Chapter 1

Introduction

1.1 History of phosphor

Inorganic luminescent materials have been known since approximately the tenth century in China and Japan as well as since the end of the Middle Ages in Europe. [1,2] Around 1600, the Stone of Bologna attracted Galilei's interest. (Table 1.1) This barite mineral emits yellow to orange lights with long persistence when subjected to sunlight. In 1671, by heating the mineral with carbon black, Kirchner was able to intensify the luminescence, indicating that impurity-type luminescence of BaS is the origin of light emission. [3] Luminescent materials these times were only used for decorative purposes. At the end of the nineteenth century, a first major milestone concerning luminescent materials and devices was the realization of gas discharges and electron beams in evacuated glass tubes by Geissler and Braun, as well as the discovery of X-rays by Rontgen. Base on these fundamental results, the first luminescent devices were developed only a few years later, and included cathode-ray tubes, fluorescent lamps, and X-ray intensifying screens. [4] Thereafter, researches on cathode-ray tube and the relevant phosphors were stimulated during the Second World

War for use in radar screen. In addition, the rapid and successful applications of fluorescent lamps for illumination purposes, as well as the use of X-rays for medical imaging, intensified researches on novel luminescent materials in the first half of the twentieth century.

Base on neon, argon, or mercury discharges in combination with different phosphors and color glasses, different colored lamps were realized. These lamps were presented by Claude at the World Exhibition in 1937 in Paris and used for advertising. [5] Using a single phosphor, generation of white light is possible if emission is more or less continuous over the whole visible spectral range. However, technical application did not start until 1938. [6] Such single-phosphors lamps containing halophosphates such as $Ca_5(PO_4)_3(Cl,F):Sb^{3+},Mn^{2+}$ are still in used today. (Fig. 1.1) As suggested in 1971 by Koedam and Opstelten, the use of rare-earth element-based luminescent materials marked a second major milestone. [7] Base on narrow f-f transition, phosphor emission can be narrowed to the visible, resulting in both high efficiency and high lumen equivalent. However, due to line-type emission bands, the opportunities to render color across a wide spectrum are low. Consequently, at last three phosphors with emission in the blue, green, and red spectral range have to be combined. (Fig. 1.1(b))

Today, luminescent materials are applied for a wide variety of applications. This

includes displays such as television tubes, computer monitor tubes, oscilloscopes, radar screens, and displays in electron microscopes. There are also many lighting applications, such as standard fluorescent lamps and energy-saving lamps. As a third important field, there is X-ray-intensifying and scintillation. (Table 1.2.) [1,8] Factors such as efficiency, emission color, decay time, quenching effects, chemical and physical stabilities, reproducibility of materials preparation and properties, environmental aspects, and cost price have to be considered.

In fact, activities aimed at producing novel phosphors for classical applications have almost come to an end. Nevertheless, materials research and development is still going on. This includes investigation and optimization of topology of phosphor layers, morphology of phosphor particles, light generation and propagation, and quantum effects, as well as many other topics.

1.2 Principles of luminescence

Luminescent materials are generally characterized by the emission of light with energy beyond thermal equilibrium. Luminescence can occur as a result of many different kinds of excitation, which is reflected in expressions such as photo-, electro-, chemi-, thermo-, sono- or triboluminescence. In practice, most often the excitation is via X-rays, cathode rays, or UV emission of a gas discharge. The role of the phosphor

is to convert the incoming radiation into visible light. And two other terms are used quite often to classify luminescent materials. Both can be related to the decay time (τ): fluorescence ($\tau < 10$ ms) and phosphorescence ($\tau > 10$ ms). [9]

$$\tau = \frac{cm_e}{8\pi e^2} \cdot \frac{\lambda^2}{fn}(\frac{3}{n^2+2})^2 \tag{1.1}$$

Where f is the oscillator strengh of the transition, λ is wavelength of the transition and n is the refractive index of the material.

The luminescence of inorganic solids can be traced to two mechanisms: luminescence of localized centers and luminescence of semiconductors (Fig. 1.2). [8,9] In the case of luminescent centers is represent is represented by transitions between energy levels of single ions (e.g., $f\text{-}f$ transition of Eu^{3+} in $Y_2O_3\text{:}Eu^{3+}$) or complex ions (e.g., charge-transfer transition on $[WO_4]^{2-}$ in $CaWO_4$). The transition rate is correlated to the relevant quantum-mechanical section rules, and reflected in the intensity as well as the decay time of the transition. Excitation and emission can be (as shown in Fig. 1.2(a)) both localized to one center (e.g., $[WO_4]^{2-}$ in $CaWO_4$)or separated from each other (e.g., Ce^{3+} as sensitizer and Tb^{3+} as activator in $LaPO_4\text{:}Ce^{3+}$, Tb^{3+}). Luminescence of semiconductors (as shown in Fig. 1.2(b)) normally occurs, after band-to-band excitation, between impurity states within the band gap (e.g., donor-acceptor pair luminescence in $ZnS\text{:}Ag^+$, Cl^-).

Fig. 1.3 reviews the possibilities mentioned for radioactive recombination in a

4

semiconductor. Semiconductors are characterized by a valence band (VB) and a conduction band (CB) by an energy gap E_g of a few eV. Excitation of the luminescence occurs by exciting electrons to the empty conduction band leaving holes in the completely filled valence band. Emission occurs by electron-hole recombination. However, emission due to recombination of free electrons and holes is exceptional. Usually recombination occurs close to or at defects in the crystal lattice. It has been the practice to distinguish edge emission (i.e. emission close to the energy E_g) and deep-center emission (i.e. emission at an energy considerably lower than E_g).

Edge emission is due to excite recombination. Usually this emission is due to bound excitation, i.e. an excitation of which either the electron or the hole is trapped at an imperfection in the lattice. Another type of recombination in semiconductors is donor-acceptor pair emission. In this type of emission an electron trapped at a donor and a hole trapped at an acceptor recombine. Other possibilities for radioactive recombination are a few holes that recombines with a trapped electron (Lambe-Klick model) or a free electron that recombines with a trapped hole (Schon-Klasens model). The trapped charge carriers may occupy deep traps, so that the emitted energy is considerably less than E_g.

The nanoparticle effective band gap can be written as

$$E_{g \cdot eff}(R) = E_g(\infty) + \frac{\hbar \pi^2}{2R^2}(\frac{1}{m_e} + \frac{1}{m_h}) - \frac{1.8e^2}{\varepsilon R} \qquad (1.2)$$

where $E_g(\infty)$ is bulk band gap, R is the ionized donor and acceptor with interimpurity distance, m_e, m_h are effective masses of the electron and hole, and ε is the bulk optical dielectric constant.

And Bohr excitation radius α_B is defined as

$$\alpha_B = \varepsilon_0\varepsilon_r h^2 / \pi m_{eh} e^2 \qquad (1.3)$$

Where ε_0 and ε_r were the permittivity of vacuum and relative permittivity semiconductor, m_{eh} is reduced of the electron and hole ($\frac{m_e m_h}{m_e + m_h}$) and e is electron charge. When

(i) $R < \alpha_B$, the quantum confinement effect becomes significant especially.

(ii) $R > 3\alpha_B$, the confinement is week and electron-hole coulomb interaction energy overcomes the confinement energy, and the whole excitation may be confine.

(iii) $\alpha_B < R < 3\alpha_B$, the quantum confinement mechanism becomes more complex and the blue shifts in the optical spectra are difficult to explain in terms of size effect alone.

The effect of quantum confinement is reflected in charges in excitation energy, absorption cross section and oscillator strength.

The puzzle of rare-earth spectra in solids was solved 40 years ago by Judd and Ofelt. [10] The rich variety of sharp optical absorption and emission lines characteristic of $4f^N \rightarrow 4f^N$ lanthanide transitions are parity forbidden in the free ions.

However, in the quantitative Judd-Ofelt theory, observation of these transitions is explained through simple configuration mixing caused by a noncentrosymmetric crystal field, allowing opposite-parity excited configurations to become slightly mixed into $4f^N$. Significant additions to this theory have been required in order to account for anomalous transitions that acquire a major fraction of their intensity from other mechanisms. The Judd-Ofelt theory, however, remains the standard method for analyzing observed rare-earth transition intensities, and successfully accounts for the intensities of up to 20 or 30 transitions per rare-earth ion with an agreement usually better than 15 % of observed oscillator strengths.

In recent years, light emitting devices have made a great advance. In particular, active research and development efforts are made on the following two subjects. The first relates to light emitting diodes (LED) and laser diodes (LD) relying as the basic principle on the injection and radiative recombination of electrons and holes across a semiconductor p-n junction. The second relates to organic electroluminescent cells relying on the basic principle that an organic thin film serving as a light emitting layer is stacked along with electron transporting and hole transporting organic substances to accomplish injection and radiative recombination of electrons and holes similar to the semiconductor p-n junction.

However, LED and LD are difficult to apply as surface-emitting devices. Even if

surface-emitting devices can be constructed, they become very expensive, suffering

from a disadvantage from the price viewpoint. So that inorganic luminescent materials

still have existence value.

1.3 Synthesis of nanosize phosphors

Several nanophosphors have been synthesised mostly as powders with few

exceptions in a matrix and as films using different techniques. Synthesis techniques

for nanomaterials, in general, can be divided into two broad categories as chemical

methods and physical methods. Under chemical methods different routes, viz.,

colloidal, capping, cluster formation, sol–gel, electrochemical, etc., are being

followed. Physical methods mostly used are molecular beam epitaxy, ionised cluster

beam, liquid metal ion source, consolidation, sputtering and gas aggregation of

monomers. Sputtering is again achieved by either using high-energy ions or laser

ablation. Again aggregation can be brought about by one of the ways, from oven

sources, laser vaporization or laser pyrolysis.

Since the mid 1970s, and accelerating significantly in the 1990s, techniques for

depositing oxide thin films from aqueous solutions at low temperatures (< 100 $^{\circ}$C)

have been reported in the literature. Such approaches offer a variety of technological

and environmental advantages over alternative routes to depositing films, as described

in recent reviews. [11,12]

One-dimensional nanometer-sized semiconductor materials, i.e., nanowires and nanorods, have attracted considerable attention due to their great potential for fundamental studies of the roles of dimensionality and size in their physical properties as well as for their application in optoelectronic nanodevices. Zinc oxide (ZnO), a semiconductor with a direct wide band gap (3.26 eV at room temperature) and large exciton binding energy (60 meV), is one of the most promising materials for the fabrication of optoelectronic devices operating in the blue and ultraviolet (UV) region and for gas sensing applications. The synthesis, characterization and application of various 1D ZnO nanostructures including the rods/wires, belts/ ribbons, rings, tetrapods, combs, sheets and complex structures are presently the subject of intense research. However, most of the synthetic procedures involve high temperature, long reaction time and toxic template.

Recently, a new solvent system, room-temperature ionic liquids (RTILs), has developed to a focal point of interest in both academia and industry. [13] RTILs are salts that are liquid at low temperatures (<100 ^{o}C) with low melting points, negligible vapor pressure, wide range of liquidus temperatures (up to 400 ^{o}C), low toxicity, nonflammability, large electrochemical window, good solvents for many organic and inorganic materials and high ionic conductively and thermal stability, making them

attractive novel environmentally friendly solvents for organic chemical reactions, separations and electrochemistry. In contrast to their successful applications in organic and materials chemistry, the use of RTILs in inorganic synthesis is still in its infancy.

Dijken *et al*. [14] in 2001 prepared colloidal solutions of nanocrystalline ZnO particles and studied quantum efficiency with particle size. NaOH solution is added slowly to zinc acetate solution. Both the solutions are in 2-propanol and pre-cooled to 0 ^{o}C. Colloidal suspension of ZnO particle of 0.7 nm radius is generated. Particle size grows with time due to aging. Growth up to 3 nm was recorded and analyzed. Quantum efficiency of the colloidal suspension of the sample is determined by comparing the emission spectrum of the sample with a reference solution of coumarone 153 in 2-propanol. Quantum efficiency of the visible emission has been found to decrease as particle size increases.

Yang's group or Kim *et al.* had reported that ZnO or GaN nanorods arrays could be grown on the sapphire substrate via the hydride vapor-phase epitaxy technique [15-16]. But, sapphire is not conductive and also relatively expensive. And the substrate temperature was over 400 ^{o}C. They used Au-coated Si wafer to serve as catalyst and form nanorods. Vayssieres is arrays of ZnO nanorods grown by the aqueous chemical method on to a ZnO nanostructured thin film and the temperature is

95 ^{o}C [17]. And Choy *et al*. also found that ZnO nanorods were successfully grown on a Si wafer by a wet-chemical process at 95 ^{o}C for 6h, where the Si wafer was dip-coated with 4 nm ZnO nanoparticles as a buffer and seed layer prior to crystal growth.[18]

Zinc aluminate ($ZnAl_2O_4$) spinels are widely used as catalytic, ceramic and electronic materials. Recently, nanostructured or nanocrystalline zinc aluminates are of interest due to their improved properties such as thermal stability and increased hardness, etc. Attia used $Al_2SO_4 \bullet 9H_2O$ and $ZnSO_4$ to form hydroxide and then calcined at 500°C for 4 hours to form $ZnAl_2O_4$. [19] In 1997, a wet mixing of zinc oxide and boehmite was also employed to obtain the $ZnAl_2O_4$ after calcined at 1000 ^{o}C for 8 h. [20] Adak prepared the $ZnAl_2O_4$ by using the polyvinylalcohol evaporation route with aluminum nitrate non-hydrate and zinc nitrate hexahydrate at 550 ^{o}C. [21] Mathur used heterometal Zn-Al alkoxides [$Zn(Al(OR)_4)_2$] and sintered at 400 ^{o}C to form $ZnAl_2O_4$. [22] Wrzyszcz developed a two-stage hydrothermal process at 160 ^{o}C / 4 h to obtain $ZnAl_2O_4$. [23] During the synthesis, the processing parameters, including reaction temperature and time, precursor concentration and pH value have to be controlled because of the complex dissolution-precipitation and transformation behavior. Although the synthesis of $ZnAl_2O_4$ spinel nanocrystalline powder has been investigated, it is important to develop a simple route on hydrothermal synthesis of

spinels, especially the study of core-shell nanoparticles. So far, most of the researches

in this area have been focused on noble-metal nanocores and molecular shells, few

studies have paid attention on nanomaterials with rare-earth metal shells. [24]

In addition, the Alkaline-earth phosphate exhibits the blue emission band

appropriate for fluorescent lamp as well as high luminescent efficiency and stability

under ultraviolet irradiation, it has been used in trichromatic fluorescent lamp.

However, a very high temperature in a complete reducing atmosphere is needed for

the synthesis of this material by conventional solid-state synthesis, which not only

takes up too much expense but also results in the large hexagonal plate-like particles

with a high aspect ratio. Considering the short penetration depth of VUV radiation

due to a large absorption coefficient in fundamental absorption, small-sized phosphor

particles with large surface area would be more effective for PDP application.

Furthermore, the formation of the apatites involves the formation of various

intermediates and the preparation of luminescent-grade raw materials is critically

dependent on various parameters such as pH values and precipitation temperature. [25]

Recently, some techniques have been reported for the preparation of

europium-activated alkaline-earth-metal chlorophosphate luminophores through

solution processing. However, the effect of the pH value in the precursor solution on

the crystalline phase and luminescence characteristics of halophosphate phosphor

nano-particles has not been systematically investigated, especially the role of annealing atmosphere in phosphor emission.

In the present literatures, Notzold had synthesized $(Sr,Eu)_5(PO_4)_3(Cl,F)$ at 700 ^{o}C and 1050 ^{o}C in reducing atmosphere. They found that the PL intensity is more usefully the host with Cl. [26] In 1998, Dafinova, used Tin as reducing agent, had synthesized white suspension of alkali-earth fluorophosphates after the powder is subjected to thermal activation at 1000°C in a reductive atmosphere. [27] Sugiyama *et al.,* using the sol–gel technique reported for the preparation of CaHAp were developed for the preparation of MgHPO$_4$ and SrHAp. The solution was dried at 100 ^{o}C for 3 h under vacuum to the dried gel and the dried gel was calcined at 900 ^{o}C for 1 h. [28]
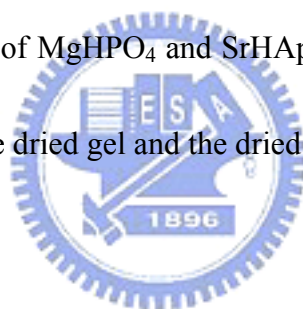
1.4 Nanosize phosphors characterization

Nanoparticles, in general, are supposed to have nearly half of their atoms contained in top two monolayers, which make optical properties highly sensitive to surface morphology. Control over movement of electrons and holes and structure of surface has been of special importance for technology development related to very low dimension optonics and electronics. Optical properties of semiconductor nanoparticles are directly dependent on the size. Blue shift of band gap and strong

non-linear response of nanoparticles of CdS and CdSe in glass samples were first reported [29] in the early 1980s. Enhanced quantum properties were further confirmed with study of other semiconductor nanoparticles of ZnS, PbS, ZnSe and CdSe. Metal nanoparticles were also synthesised with a view to prepare better catalysts.

To understand the physics and develop applications based on nanophosphors that come under the category of doped nanocrystals (DNC) and also in field of quantum dots, huge amount of research effort is being expanded during the recent years. The development of applications and physics of quantum confined 2D-electron gas structures has given a boost to the effort. To utilize the phenomena of quantum confinement further, device fabrication with nano dimensions is being done world over with urgency. The challenge is great but will be equally rewarding.

Luminescence properties are measured by usual techniques and instruments used for studying phosphors. The measuring set-up has to be at least one generation higher than existing ones as regards excitation and emission range, spectral resolution, nano to picosecond time resolution and with high intensity, higher energy excitation sources. X-ray diffraction (XRD), small angle X-ray scattering (SAXS), small angle neutron scattering (SANS), high resolution electron microscopy (HRTEM), low frequency Raman scattering and longitudinal-optic (LO) phonon Raman scattering, atomic force microscope (AFM), time of flight secondary ion mass spectrometry

(ToF-SIMS) and X-ray photoelectron spectroscopy (XPS) are the other characterisation techniques used for development and understanding of nanophosphors.

1.5 Outline of this dissertation

The dissertation is divided into eight chapters listed below:

Chapter 3 discusses the structural crystallinity and photoluminescence properties of nitrogen- implantd ZnO thin film under different atmosphere and annealing treatment.

Chapter 4 presents the high-density good c-axis crystalline ZnO nanorods ultraviolet emission will enhance after N_2-atmosphere annealing.

Chapter 5 discusses the role of solvents in europium doped zinc oxide (Eu:ZnO) in red emission effect.

Chapter 6 introduces the formation of nano-sized $ZnAl_2O_4$ depended on pH values in the precursor solution. And using the cationic surfactant CTAB, the $ZnAl_2O_4$/Eu core-shell structure can be developed.

Chapter 7 proposes the controlling the solution pH value (crystalline phase) and changing annealing atmosphere. The Eu-doped halo-phosphate photoluminescence relative peak intensity of both red and blue emissions can be tunable.

Chapter 8 is the main conclusions in this study.

Table 1.1 Early milestones in the siscovery of luminescent materials and devices.

Year	Kind of discovery	Excitation source	Type of luminescent material	Emission color
~1600	Stone of Bologna	sunlight	$BaSO_4$ (BaS)	yellow
1858	Geißler's tube	gas-discharge (Hg)		UV
1859	Becquerel	gas-discharge (Hg)	ZnS	yellow-white
1895	X-rays (by Röntgen)		none (photographic plate)	
1896	X-ray intensifier (by Pupin)	X-ray	$CaWO_4$	blue
1896	Fluorescent lamp (by Edison)	gas-discharge (Hg)	$CaWO_4$	blue
1897	Braun's tube	cathode-ray	$CaWO_4$	blue
1916	Neon discharge lamp (by Claude)	gas-discharge (Ne)	none	red
1925	Black-and-white television	cathode-ray	$ZnS:Ag^+$; $(Zn,Cd)S:Ag^+$	blue; yellow
1937	Neon discharge lamp (by Claude)	gas-discharge (Ne)	$CaWO_4$; $Zn_2SiO_4:Mn^{2+}$	blue; green
1938	Fluorescent lamp	gas-discharge (Hg)	$MgWO_4$; $(Zn,Be)_2SiO_4:Mn^{2+}$	blue-green; green-red
1941	Radar screen	cathode-ray	$(Zn,Cd)S:Cu^+,Al^{3+}$	green
1946	Insect lamps	gas-discharge (Hg)	$CaWO_4$	blue
1960	Color television	cathode-ray	$ZnS:Ag^+$; $(Zn,Cd)S:Cu^+,Al^{3+}$; $(Zn,Cd)S:Ag^+$	blue; green; red
1960	Laser (by Maiman)	gas-discharge (Hg)	$Al_2O_3:Cr^{3+}$	red
1972	Computed tomography (by Houndsfield)	X-ray	$NaI:Tl^+$	green
1972	Rare-earth phosphors	gas-discharge (Hg)	$Sr_3(PO_4)_5Cl:Eu^{3+}$; $LaPO_4:Ce^{3+},Tb^{3+}$; $Y_2O_3:Eu^{3+}$	blue; green; red

Table 1.2 Most important phosphors for practical use.

Emission colour	Application			
	Cathode Ray Tube	Plasma Display Panel	Fluorescent Lamp	X-ray-Intensifying / Scintillation
blue	$ZnS:Ag^+,Cl^-$	$BaMgAl_{10}O_{17}:Eu^{2+}$	$BaMgAl_{10}O_{17}:Eu^{2+}$ $Sr_4Al_{14}O_{25}:Eu^{2+}$ $Sr_3(PO_4)_5Cl:Eu^{2+}$	$NaI:Tl^+$ $Ba(F,Br):Eu^{2+}$ (storage phosphor) $LaBr_3:Ce^{3+}$ $Bi_4Ge_3O_{12}$ $Gd_2SiO_5:Ce^{3+}$ / $Lu_2SiO_5:Ce^{3+}$ $LuAlO_3:Ce^{3+}$ $YTaO_4:Nb^{5+}$
green	$ZnS:Cu^+,Au^+,Al^{3+}$ $ZnS:Cu^+,Al^{3+}$	$BaAl_{12}O_{19}:Mn^{2+}$ $Zn_2SiO_4:Mn^{2+}$ $BaMgAl_{10}O_{17}:Eu^{2+},Mn^{2+}$	$GdMgB_5O_{10}:Ce^{3+},Tb^{3+}$ $LaPO_4:Ce^{3+},Tb^{3+}$ $CeMgAl_{11}O_{19}:Tb^{3+}$	$CsI:Tl^+$ $Gd_2O_2S:Tb^{3+}$
yellow			$Y_3Al_5O_{12}:Ce^{3+}$	
red	$Y_2O_2S:Eu^{3+}$	$Y_2O_3:Eu^{3+}$	$Y_2O_3:Eu^{3+}$ $(Y,Gd)(P,V)O_4:Eu^{3+}$	
white			$Ca_5(PO_4)_3(F,Cl):Sb^{3+},Mn^{2+}$	

17

Fig. 1.1 (a) Emission spectrum of $Ca_5(PO_4)_3(Cl,F):Sb^{3+},Mn^{2+}$ (solid line) as used in single-phosphor lamps compared to the eye sensitivity curve. (b) Emission spectrum of $BaMgAl_{10}O_{17}:Eu^{2+}$ (solid line), $LaPO_4:Ce^{3+},Tb^{3+}$ (dotted line), $Y_2O_3:Eu^{3+}$ (dashed line) as used in tri-color lamps compared to the eye sensitivity curve.
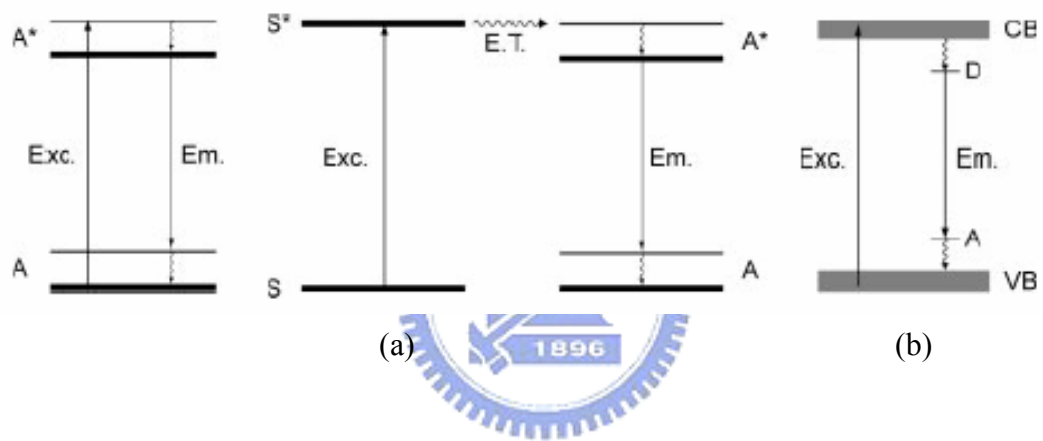
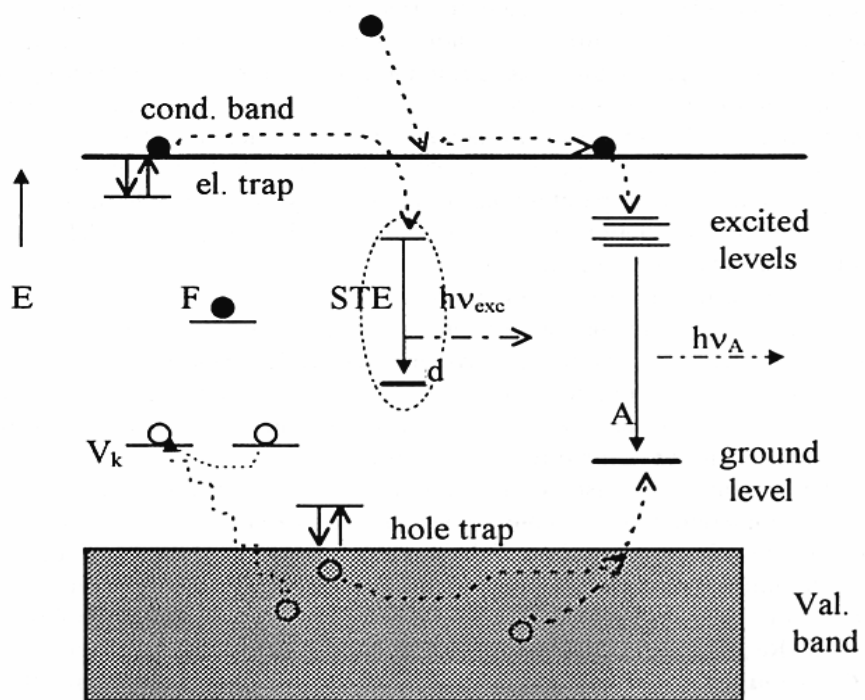Fig. 1.2 Schemes illustrating the underlying physical processes of luminescence on (a) isolated center and (b) in semiconductors.

Fig 1.3 Emission transitions in semiconductor (schematically representation). The band gap E_g separates the valence band (VB) and the conduction band (CB).

Chapter 2

Experimental

2.1 Experimental process

2.1.1 ZnO film

The ZnO thin films (~150 nm thick) were deposited on 4 inch diameter Si substrates by RF magnetron sputtering, using 99.99% ZnO as the target. The growth chamber was evacuated by a turbo pump and mechanical pump. Before the deposition, a target was pre-sputtering by Ar ions for 10 min to remove contamination on the target. Argon and oxygen mixtures with oxygen molar ratio (OMR) of 5 % were used as sputtering gases. Silicon substrates were cleaned by usual semiconductor technology methods before loading into the chamber. Sputtering conditions for ZnO films were performed at a substrate temperature of 50 ^{o}C, RF power of 50W, sputtering pressure of 10m Torr and sputtering time of 40 minutes.

(1) Nitrogen- implanted

The as-grown ZnO film was subsequently subjected to N implantation at room temperature. The nitrogen ions with energy of 80 keV were injected into the as-grown ZnO films.

(2) ZnO nanorods

The flow chart of preparing ZnO nanorods was shown in Fig. 2.1. Both precursors of methenamine ($C_6H_{12}N_4$) and zinc nitrate hexahydrate ($Zn(NO_3)_2 \cdot 6H_2O$) were used for preparing the solution to grow ZnO nanorods (ZNs). The ZnO_f/Si substrates were then placed inside the aqueous solution at 75 ^{o}C for 10 h. After that, the substrates were removed from the aqueous solutions, rinsed with distilled water, and dried at room temperature overnight.

2.1.2 Preparation of $ZnAl_2O_4$ and $Ca_{10-y}Sr_y(PO_4)_6Cl_2$ nano phosphors

(1) Precursor
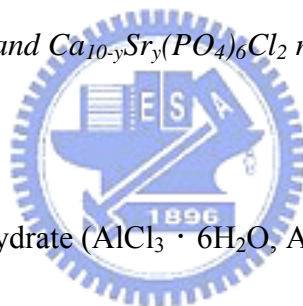
Aluminum chloride hexahydrate ($AlCl_3 \cdot 6H_2O$, Aldrich, 99%)

Zinc chloride ($ZnCl_2$, Aldrich, 99%)

Europium nitrate hexahydrate ($Eu(NO_3)_3 \cdot 6H_2O$, Merck, 99%)

Calcium nitrate hexahydrate ($Ca(NO_3)_2 \cdot 6H_2O$, Merck, 99%)

Strontium chloride hexahydrate ($SrCl_2 \cdot 6H_2O$, Aldrich, 99%)

Urea (H_2NCONH_2, Merck, 99%)

Ammonium nitrate (NH_4NO_3, Riedel, 99%)

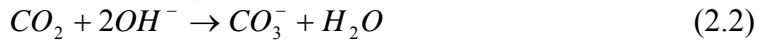Diammonium hydrogen phosphate (DAP, $(NH_4)_2HPO_4$, Aldrich, 98%)
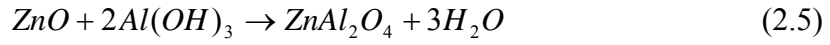
(2) Chemical reaction
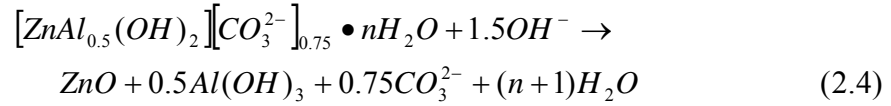
(i) Synthesis of $ZnAl_2O_4$ (ZA):

As the pH value was 7 at T = 25 °C, it was found that the $Al(OH)_3$ was formed following the reaction of Eq. 2.1 but the Zn^{2+} ions still remain in amorphous state.

$$Al^{3+} + H_2O \rightarrow Al(OH)_3^0 + 3H^+ \tag{2.1}$$
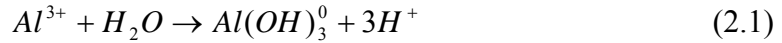
With an increase of the reaction temperature, at 120 °C, the $Al(OH)_3$ would further react with Zn^{2+} to form ZnAl layered double hydroxide (ZnAl-LDHs). The layered double hydroxides (LDHs) are a family of natural and synthetic materials of general type $[M_{1-x}^{2+}M_x^{3+}(OH)_2]^{x+} X_{x/m}^{m-} \bullet nH_2O$, X= Cl or CO_3, sometimes known as anionic clays. The structure is shown in Fig 2.2. [30] These materials are structurally similar to the mineral brucite and the formation of ZnAl-LDHs was described as follows.
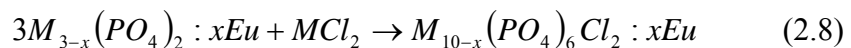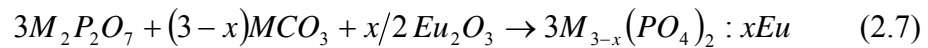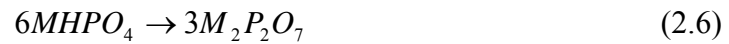
$$CO_2 + 2OH^- \rightarrow CO_3^- + H_2O \tag{2.2}$$

$$Zn^{2+} + 2Al^{3+} + 6.5OH^- + 0.75CO_3^{2-} + nH_2O \rightarrow$$
$$[ZnAl_{0.5}(OH)_2][CO_3^{2-}]_{0.75} \bullet nH_2O + 1.5Al(OH)_3 \tag{2.3}$$
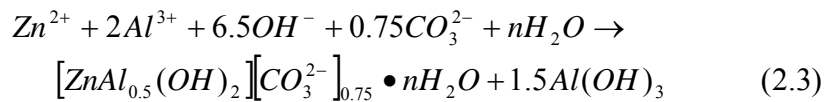
The CO_3^{2-} ions are from CO_2 in the air and the formation of $[ZnAl_{0.5}(OH)_2][CO_3^{2-}]_{0.75} \bullet nH_2O$ leads to amorphous $Al(OH)_3$. At a higher reaction temperature (T >120°C), more energy was provided to snap ZnAl-LDHs into two layers and promote the formation of ZnO and $Al(OH)_3$ (Eq. 2.4). Then, both ZnO and $Al(OH)_3$ phases will further react together to form ZA (Eq. 2.5).

$$[ZnAl_{0.5}(OH)_2][CO_3^{2-}]_{0.75} \bullet nH_2O + 1.5OH^- \rightarrow$$
$$ZnO + 0.5Al(OH)_3 + 0.75CO_3^{2-} + (n+1)H_2O \qquad (2.4)$$

$$ZnO + 2Al(OH)_3 \rightarrow ZnAl_2O_4 + 3H_2O \qquad (2.5)$$

(ii) Synthesis of $Ca_{10-y}Sr_y(PO_4)_6Cl_2$:

Alkaline-earth-metal halophosphates, also known as apatites, have the generic molecular formula $M_5(PO_4)_3X$ (M = Ca, Sr, Ba; X = F, Cl, Br, OH) and are well known for their applications as phosphor materials[31,32], laser hosts [33] and biocompatible materials. [34]

Various routes have been reported for the preparation of $M_5(PO_4)_3X$ employing different phosphate sources. [31,35,7] The commercial method is based on the conventional ceramic route, involving high temperatures, employing $MHPO_4$ as the phosphate source, along with MCO_3, Eu_2O_3 and MCl_2 in suitable proportions. The formation of $M_5(PO_4)_3X : Eu^{2+}$ can be given as follows:

$$6MHPO_4 \rightarrow 3M_2P_2O_7 \qquad (2.6)$$

$$3M_2P_2O_7 + (3-x)MCO_3 + x/2\,Eu_2O_3 \rightarrow 3M_{3-x}(PO_4)_2 : xEu \qquad (2.7)$$

$$3M_{3-x}(PO_4)_2 : xEu + MCl_2 \rightarrow M_{10-x}(PO_4)_6Cl_2 : xEu \qquad (2.8)$$

As can be seen from Eq. 2.6-2.8, the formation of apatites involves the formation of various intermediates. Further, the preparation of luminescent-grade materials critically dependent on various parameters such as pH, concentration of the metal and

phosphate ions, precipitation temperature, rate of digestion.

Eu^{2+}-doped $Ca_{10-y}Sr_y(PO_4)_6Cl_2$ is obtained by rapidity an aqueous concentrated

solution containing stoichiometric amounts of metal nitrates, chlorides, urea and DAP

as given in the following equation.

$$\begin{aligned} (10 - x)Ca(NO_3)_3 &+ xEu(NO_3)_3 + 15NH_2CONH_2 \\ &+ 18NH_4NO_3 + 6(NH_4)_2HPO_4 + ySrCl_2 \\ \rightarrow Ca_{10-x-y}Sr_y&(PO_4)_6Cl_2 + 49N_2 + 93H_2O + 15CO_2 \qquad (2.9) \end{aligned}$$
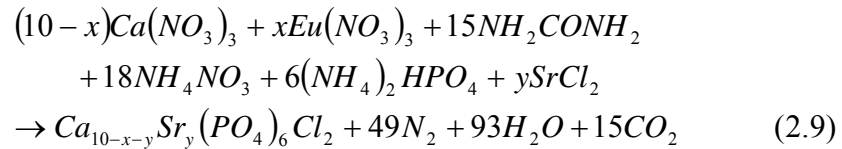
The flow chart of preparing $Ca_{10-y}Sr_y(PO_4)_6Cl_2 : xEu^{2+}$ was shown in Fig. 2.3.

2.2 Characterization analysis

(1) X-ray diffraction analysis (XRD)

The phase or structure of thin film and phosphor were characterized by a MAC

science, M18X diffractometer (at 50kV and 200 mA) with Cu Kα radiation.

(2) Scanning electron Microscopy (SEM)

The surface morphology of the nanoparticles and film thickness were also

observe by Scanning electron Microscopy (SEM) using JEOL-6500F

(3) Transmission electron microscope (TEM)

The morphology and microstructures of the nanoparticles were examined by

transmission electron microscope (TEM) with Philips TECNAI 20.

(4) Photoluminescence (PL)

The luminescent properties are characterized by the excitation from 325 nm He-Cd laser and Hitachi FL F4500 at room temperature.

(5) Fourier transform infrared (FTIR)

The chemical bands were obtained by FT-IR spectrometer (Bomem, DA8.3) spectra using KBr disks containing ~ 1 % sample.

(6) Electron paramagnetic resonance spectrometry (EPR)

The g factor measurements were performed using an *X*-band (9.776 GHz) Bruker spectrometer at room temperature.

(7) Secondary ion mass spectroscopy (SIMS)

The depth profile of the implanted ions was measured by secondary ion mass spectrometry (CAMECA IMS-SF). A 10 keV Cs^+ primary beam was used to determine the atomic distruibution of the implanted N.

(8) Extended X-ray absorption fine structure (EXAFS)

Zinc K-edge X-ray absorption spectra were recorded at the wiggler beamline BL17C at NSRRC. The electron storage ring was operated at energy of 1.5 GeV and a current of 120-200 mA.

```
                    ┌─────────────────┐
                    │ R. F. sputtering │
                    └─────────────────┘
                             │
                             ▼
┌───────────────┐  ┌─────────────────┐  ┌──────────────────────┐
│   C₆H₁₂N₄     │  │     ZnO/Si      │  │  Zn(NO₃)₂ · 6H₂O     │
└───────────────┘  └─────────────────┘  └──────────────────────┘
        │                    │                      │
        └──────────────►┌─────────────────┐◄────────┘
                        │ Aqueous solution │
                        └─────────────────┘
                                 │ 75ºC
                                 ▼
                        ┌─────────────────┐
                        │   ZnO nanorod   │
                        └─────────────────┘
                                 │ Annealing
                                 ▼
                        ┌─────────────────┐
                        │   Measurement   │
                        └─────────────────┘
```
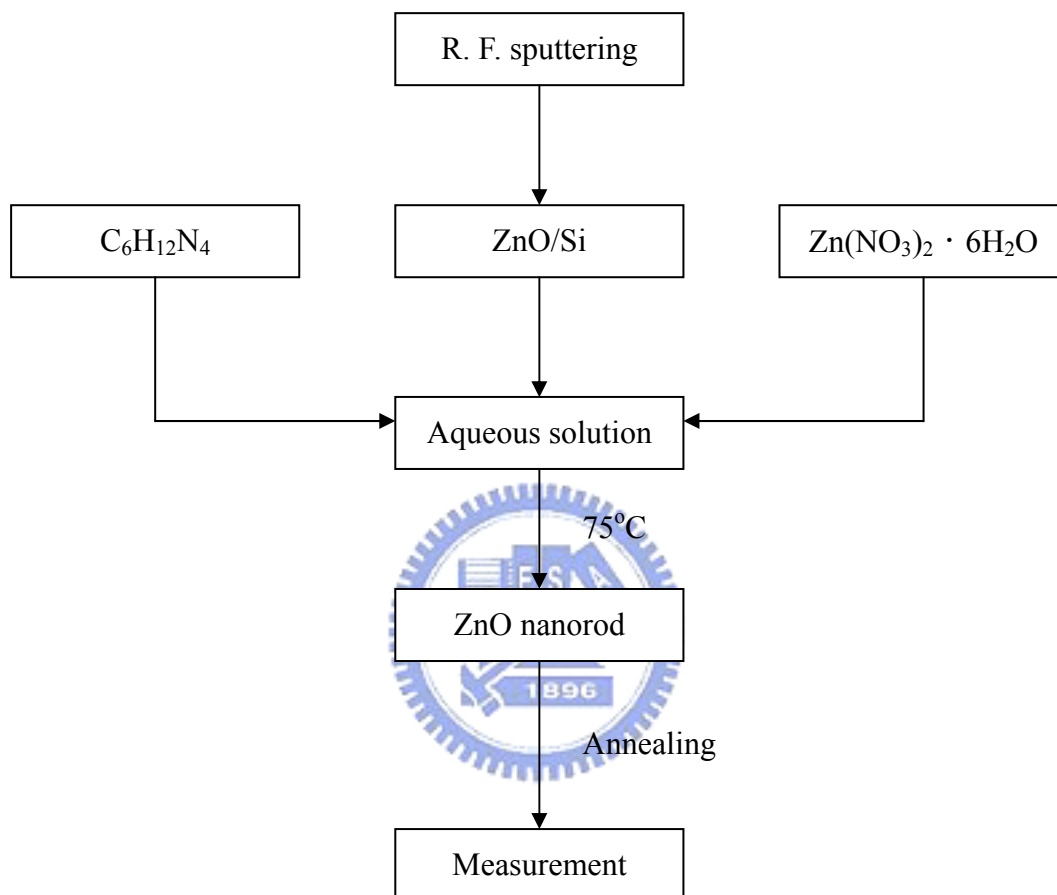
Fig. 2.1 Flow chart for preparing ZnO nanorods
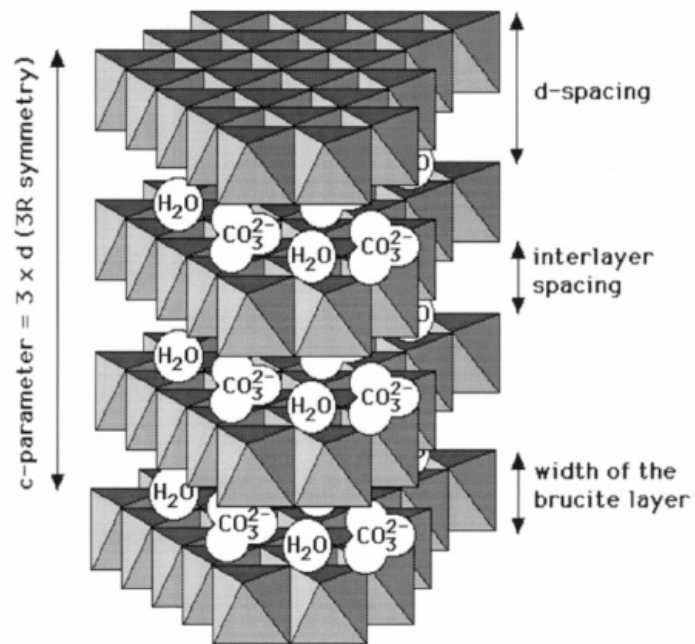
Fig. 2.2 Idealized structure of a layered double hydroxide, with interlayer carbonate anions. Several parameters are defined.
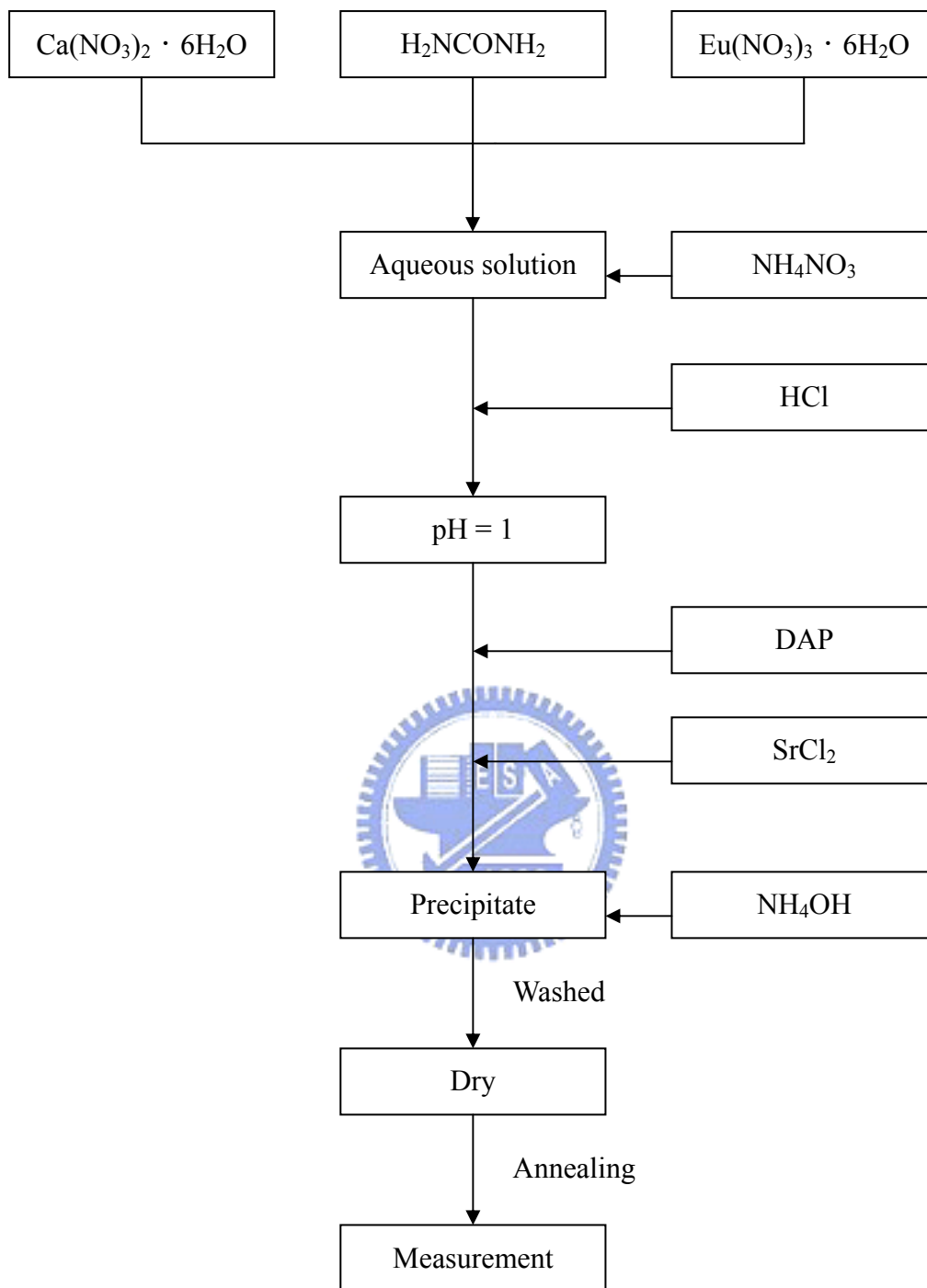
Fig. 2.3 Flow chart for preparing $Ca_{10-y}Sr_y(PO_4)_6Cl_2{:}xEu^{2+}$ nanosize phosphors

Chapter 3

Physical characteristics and photoluminescence properties of nitrogen- implantd ZnO thin film

3.1. Introduction

In wide-band gap optoelectronics, zinc oxide (ZnO) is attracting more attention because of its potential applications in various fields, such as ultraviolet (UV) resistive coating, gas sensors, solar cells and optical devices. [37, 38] One of these unique properties is that ZnO thin films present strong spontaneous and simulated emissions by excitons even at room temperatures. [39, 40] It has been recognized that to grow high-quality *p* and *n* type ZnO thin films is necessary for the development of ZnO-based optoelectronic devices. The *n*-type ZnO is available even without any doping because ZnO is a natural n-type semiconductor, while it has been recognized that *p*-type ZnO is very difficult to develop although high-densities of holes could be achieved with nitrogen as the dopant. The presence of intrinsic defects such as interstitial zinc and oxygen vacancies has been considered to cause a deviation from stoichiometry. [41] Ogata *et al.* reported that those intrinsic defects can be reduced by thermal annealing of ZnO layer in O_2 atmosphere but the electron carrier density was

also decreased. [42]

So far, there have been several reports on fabrication of *p*-type ZnO films using N or As. [43, 44] Nitrogen (N) doping has been considered as an effective method to realize *p*-type ZnO films because N has the smallest ionization energy in group V-dopants. [45] Recently, several investigations have been focused on nitrogen and donor co-implanted ZnO to study the solubility and diffusion behavior of nitrogen in ZnO crystal. [46, 47] Georgobiani *et al.* studied the electrical properties of ZnO films with ion implantation of nitrogen from 3×10^{14} to 3×10^{15} ions/cm^2 in oxygen atmosphere. It was shown that the nitrogen implantation could result in the formation of the hole type of conductivity but new peaks had appeared in the ultraviolet and visible ranges of photoluminescence spectra. [48]

Even though it was reported that p-type ZnO may be developed by some novel technologies, no detailed studies were made to investigate the effect of implanted-nitrogen concentration on the structural change and optical properties of sputtered ZnO films. Furthermore, it is well known that both physical characterization and optoelectronic properties are strongly influenced by the defect concentration in ZnO films and this can be modified and controlled via nitrogen treatment under different atmosphere and annealing conditions. Therefore, in this work, ZnO films were pre-treated with nitrogen implantation in the range from 5×10^{12} - 5×10^{15} ions/cm^2. The photoluminescence behavior of the N-implanted ZnO films annealed in different atmospheres as a function of nitrogen concentration will be focused.

3.2. Experimental procedure

The ZnO thin films (~150 nm thick) were deposited on 4 inch diameter Si substrates by RF magnetron sputtering, using 99.99% ZnO as the target. The growth chamber was evacuated by a turbo pump and mechanical pump. Before the deposition, a target was pre-sputtering by Ar ions for 10 min to remove contamination on the target. Argon and oxygen mixtures with oxygen molar ratio (OMR) of 5% were used as sputtering gases. Silicon substrates were cleaned by usual semiconductor technology methods before loading into the chamber. Sputtering conditions for ZnO films were performed at a substrate temperature of 50 ^{o}C, RF power of 50W, sputtering pressure of 10m Torr and sputtering time of 40 minutes. The as-grown ZnO film was subsequently subjected to N implantation at room temperature. The nitrogen ions with energy of 80 keV were injected into the as-grown ZnO films. The fluences range studied was from 5×10^{12} - 5×10^{15} ions/cm^2. Based on Rutherford back scattering measurement followed by (the transport of ions in matter) TRIM simulations, the nitrogen ion distribution in ZnO films forms a nearly perfect Gaussian shape with the peak position at (80±10) nm below the surface. After ion implantation, the specimens were annealed at 850 ^{o}C and 1000 ^{o}C for 20 minutes under pure oxygen and nitrogen atmospheres. The thickness of ZnO films was measured using a surface profilometer (Tencor Alpha-Step 200) and the crystal

structure was determined by X-ray diffractometer using CuKα radiation. Photoluminescence measurement was performed by the excitation from 325 nm He-Cd laser at room temperature. The depth profile of the implanted ions was measured by secondary ion mass spectrometry (CAMECA IMS-SF). A 10 keV Cs^+ primary beam was used to determine the atomic distruibution of the implanted N.

3.3. Results and Discussion

3.3.1. Physical characteristics

Fig. 3.1 shows the depth profile of nitrogen-implanted ZnO films with various fluences. As can be seen, a normal shape with almost Gaussian distribution was observed for the ZnO film after annealed at 850 ^{o}C in nitrogen atmosphere. An abrupt change as marked in Fig. 3.1 appears in the slope of the concentration profile. The concentration at this point corresponds to the solubility of N in ZnO film that is determined as 9.1×10^{17}, 4.2×10^{18}, and 6.3×10^{18} ions/cm^3 with the fluence of 5×10^{12}, 1×10^{14}, and 5×10^{15} ions/cm^2, respectively. [49] The value of solubility is equal to about 4~5 atom ppm and this implies that the N is a very insoluble element in ZnO.

Fig. 3.2 shows the XRD patterns of the N-implanted (fluence of 5×10^{12}, 1×10^{14}, and 5×10^{15} ions/cm^2) and non-implanted ZnO thin films annealed at 850 ^{o}C in

nitrogen atmosphere. A strong and sharp (002) peak is observed in non-implanted

sample (Fig. 3.1), which indicates that the ZnO film exhibits a preferred (002)

orientation with c-axis perpendicular to the substrate. With an increase of nitrogen

concentration, it was found that diffraction peak was shifted towards the smaller 2θ

direction and the shift increases with an increase of fluence from 5×10^{12} to 1×10^{14}

ions/cm^2. According to the Bragg Law, the shift implies that the lattice constant

increases. This was considered due to the incorporation of the nitrogen at interstitial

sites in ZnO, leading to an increase in the lattice constant. However, as the fluence

exceeds 1×10^{14} ions/cm^2, the position of diffraction peak was almost unchanged but

a weak diffraction peak was observed at the fluence of 1×10^{14} ions/cm^2 for the

N-implanted ZnO films annealed at 850 ^{o}C in nitrogen atmosphere. It was believed

that the phenomenon is strongly dependent on the solubility limit of N ion in the ZnO

matrix. It could be postulated that part of nitrogen ions could have occupied the sites

of O atom. Therefore, the (002) peak was shifted to lower diffraction angle side and

the crystal structure was deteriorated.

On the other hand, as both N-implanted and non-implanted ZnO films were

annealed in oxygen atmosphere at 850 ^{o}C, the XRD patterns in Fig. 3.3 illustrate that

the diffraction peak (002) of N-implanted ZnO samples is also shifted with the

implanted N concentration up to 1×10^{14} ions/cm^2. Similar phenomenon is also

observed in the samples annealed at nitrogen atmosphere and this indicates that there

exists a solubility limit for N-implanted ZnO film annealed at 850 ^{o}C but seems

independent of the annealing atmosphere. However, as comparing Fig. 3.2 with 3.3, it

was found that the (002) peak is stronger for the samples annealed at O_2 than N_2

atmosphere. This may suggest that the nitrogen-implanted ZnO films present better

crystalline when annealed in oxygen atmosphere compared to that in nitrogen

atmosphere.

3.3.2. Photoluminescence properties

Our previous studies found that the predominant lattice defects in the as-grown

ZnO films is the oxygen vacancies because the as-grown ZnO films were sputtered at

the OMR 5%. As the samples were annealed below 500 ^{o}C, a very low intensity

emission with the same feature as the as-grown films was observed. However, with

the increase of annealing temperature, some lattice and surface defects could be

removed and the ZnO film would be re-structured into more perfect structure. At 850

^{o}C, a strong NBE emission with a weak deep-level emission of 528 nm was obtained.

However, when the films were annealed at a higher annealing temperature such as

1000 ^{o}C, a wide emission band appears around 560 nm and the deep-level emission

peak shifts from 2.35 eV to 2.26 eV in comparison with that at 850 ^{o}C. [50] Therefore,

850 ^{o}C was used in this work to study the influence of implanted nitrogen

concentration on the ZnO films in different atmospheres.   As shown in Fig. 3.4 (a), a

very stronger NBE peak (378 nm) and a relatively low deep-level emission (528 nm)

were obtained for the non-implanted sample. However, as the ZnO films were

implanted with different fluences of nitrogen ion and annealed in this condition (N_2

atmosphere), the NBE peak becomes weaker and presents slightly red shift as

compared to the non-implanted one. The decrease in the NBE emission must be

related to the variation of the intrinsic defects such as zinc vacancy V_{Zn}, oxygen

vacancy V_o and interstitial zinc Zn_i.   As the samples were annealed at 850 ^{o}C in

nitrogen atmosphere, either V_o or Zn_i should be apparently increased and this could

promote the possibility of N_i to occupy the oxygen vacancies to form N_o defects.

Therefore, both Zn_i and N_o will be increased with increasing implanted nitrogen

concentration. Furthermore, it was found that with an increase of implanted nitrogen

concentration, the NBE emission of ZnO film becomes weak. This PL result along

with the XRD analysis implies that there exists a critical implanted nitrogen

concentration corresponding to the defect transition that in turn influences the related

PL properties. Generally, the defect reaction for non-implanted films can be expressed

as follows:

$$Zn_{Zn} + O_o \Rightarrow Zn_i + V_o + \frac{1}{2}O_2 \qquad\qquad (3.1)$$
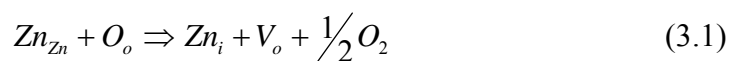
When the ZnO film was annealed at a higher temperature, both zinc interstitials

and oxygen vacancies would be induced from the ZnO films as illustrated in Eq. 3.1.

However, as the ZnO was implanted with nitrogen and then annealed at high

temperatures, the induced defect concentration and defect type would be changed with

different fluences for the nitrogen-implanted ZnO films. In order to clarify the role of

N-implanted concentration in the ZnO films, it can be further elucidated as follows.

First, if the fluence was below 1×10^{14} ions/cm^2, the nitrogen ions may possibly

substitute for the oxygen atoms in ZnO films depending on annealing conditions

especially on atmosphere. Because the ZnO films in our experiment grew in lower

oxygen partial pressure (OMR = 5%), V_o and Zn_i can be easily formed especially as

the ZnO films were further annealed in nitrogen atmosphere at high temperatures.

Therefore, the oxygen could be evaporated from the as-grown ZnO films and more

oxygen vacancies will be produced in nitrogen atmosphere. Furthermore, it is possible

for a certain amount of nitrogen ions to occupy oxygen sites in the N-implanted ZnO

films after nitrogen annealing at high temperatures. The defect chemistry (reaction)

could be depicted as follows:

$$N_i + ZnO \xrightarrow{\ N_2\ } Zn_{Zn} + N_O + \frac{1}{2}O_2$$
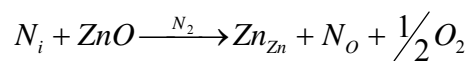
(3.2)

Therefore, the peak intensity of NBE emission decreases with the increase of

implanted nitrogen concentration as illustrated in Fig. 3.4 (a). Therefore, it is likely

that high nitrogen concentration is responsible for the producing high amount of

structure defects (N_o) in ZnO films, which are the centers of non-radiative

recombination. Using the full potential linear muffin-tin orbital method, Lin *et al*. [51]

calculated the levels formed by some defects in ZnO films shown in Fig. 3.5. It is

seen from Fig. 3.5 that the energy transferred probable process during NBE emission

and deep-level emission (green).

In addition, according to XPS analysis for oxygen (O1s) peak in the ZnO films,

the intensity of the peak (531 eV) shown in Fig. 3.6 (a) for the non-implanted sample

annealed at 850 ^{o}C in nitrogen atmosphere represents the measured amount of oxygen

atoms in a fully oxidized stoichiometric surrounding. The binding energy side of the

O1s spectrum at 531.25 ± 0.20 eV is associated with O^{2-} ions in the oxygen deficient

regions within the matrix of ZnO [52]. Therefore, the change in this peak intensity

(O1s at 531.25 ± 0.20 eV) may be partly correlated with the variation in the

concentration of oxygen vacancies. Dependence of the relative intensity ratio of this

component on O1s at 531.25 ± 0.20 eV can be further depicted in Fig. 3.6 (b). It was

found that the concentration of oxygen vacancies decreases with an increase of the

N-implanted fluence in ZnO film but this phenomenon is more obvious for the

samples annealed in oxygen atmosphere. This indicates that part of nitrogen ions have

occupied at the oxygen vacancies (sites).   Based on above-mentioned results, it can

be inferred that the amount of both zinc interstitials and concentration of antisite N_o

would increase in proportion to the fluence of nitrogen ions for the N-implanted ZnO

films annealed at 850 ^{o}C. The amount of both zinc interstitials and concentration of

antisite N_o would increase in proportion to the fluence of nitrogen ions.

However, if the annealing atmosphere was exchanged and the oxygen

atmosphere was used for annealing the N-implanted ZnO, the number of oxygen

vacancies (V_o) existing in the as-deposited ZnO film will be further decreases

probably because the effective incorporation of O atom diminishes those donor levels.

Therefore, the (002) peak intensity and better crystalline were obtained for the ZnO

films annealed in oxygen atmosphere compared to those annealed in nitrogen

atmosphere (comparing Figs. 3.2 with 3.3). In this condition, part of the implanted

nitrogen ions are probably located as the interstitial defects (N_i) in the ZnO films

because of limited available oxygen vacancies. Therefore, when the N-implanted ZnO

films were implanted with a lower dose of 5×10^{12} ions/cm^2 nitrogen ions which is

below the solubility limit, some of nitrogen ions could be incorporated into the

oxygen sites to reduce the intrinsic defect and restore the radiation damage. Therefore,

the peak intensity of NBE emission was slightly enhanced by the implantation of

nitrogen ions. Furthermore, as compared with Figs. 3.4 (a) with (b), it reveals that for

the same lower N-implanted concentration, i.e. 5×10^{12} fluence, a stronger NBE peak

intensity was detected in the N-implanted ZnO film annealed in oxygen atmosphere

compared to that annealed in nitrogen atmosphere. However, with an increase of

implanted nitrogen concentration, more implanted nitrogen ions were incorporated

into the ZnO matrix and the structure defects were further increased. As the implanted

fluence exceeds 1×10^{14} ions/cm^2 i.e., 5×10^{15} ions/cm^2, a broader deep level peak

around 532 nm due to high levels of nitrogen incorporation was observed in the

sample annealed in oxygen atmosphere compared to that annealed in nitrogen

atmosphere because a large amount of nitrogen ions could be dissolved in the ZnO

films as the interstitial defects and the produced unstable defects would deteriorate the

crystalline and become some nonradiative center to absorb the light emission during

photoluminescence process.
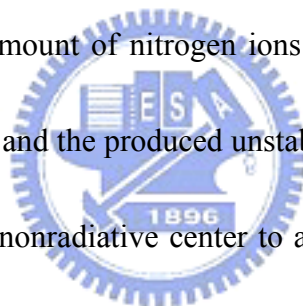
3.4. Conclusions

The ZnO films implanted with nitrogen ions from 5×10^{12} to 5×10^{15} ions/cm^2

show high preferred-orientation (c-axis) films with strong NBE emission property. It

was found that there exists a solubility issue of nitrogen in ZnO films. Furthermore,

the annealing atmosphere plays an important role in crystalline and

photoluminescence of nitrogen-implanted ZnO films. When annealed in nitrogen

atmosphere, the peak intensity of near band-edge (NBE) emission remarkably decreases with the increase of concentration of implanted nitrogen. However, when the ZnO films were implanted with 5×10^{12} ions/cm^2 and annealed in oxygen atmosphere, the optical properties are improved probably because the effective incorporation of O atom diminishes those donor levels (oxygen vacancies) and the crystalline is also improved due to implanted nitrogen. However, excess nitrogen would reduce the crystalline and promote the formation of the deep-level emission due to high amount of intrinsic and structure defects. This study reveals that it is possible to control the crystalline and the NBE emission of the ZnO films by using different annealing atmospheres and changing the nitrogen-implanted fluence.
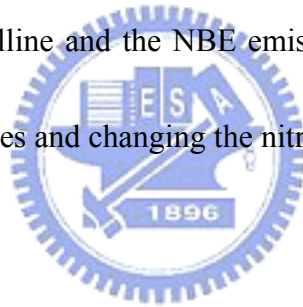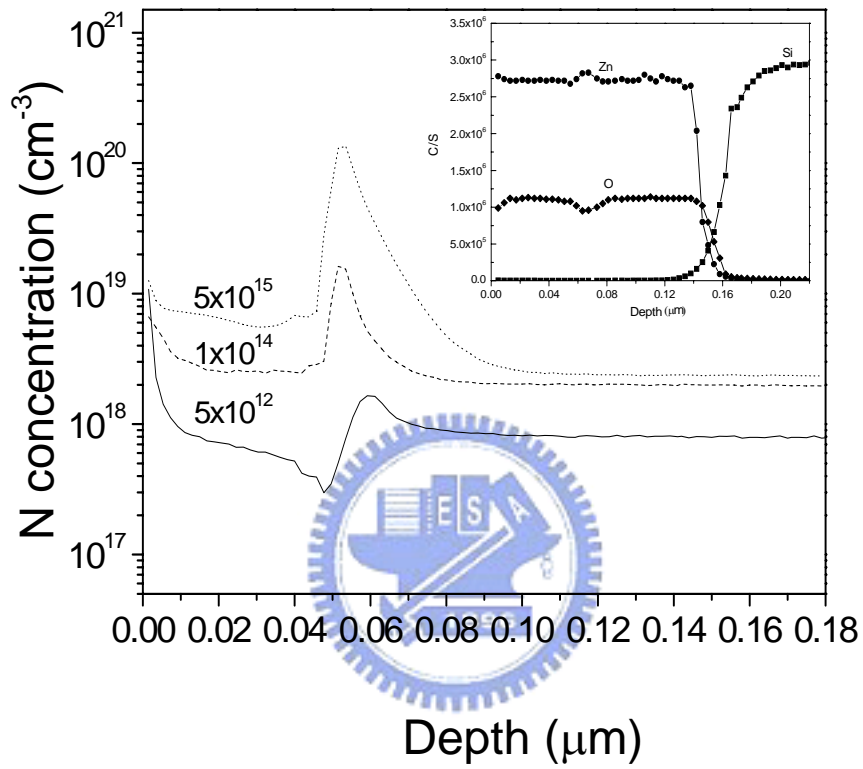
Fig. 3.1 SIMS depth profile of various fluences of nitrogen implanted into ZnO films
after annealing at 850 ^{o}C in nitrogen atmospheres.
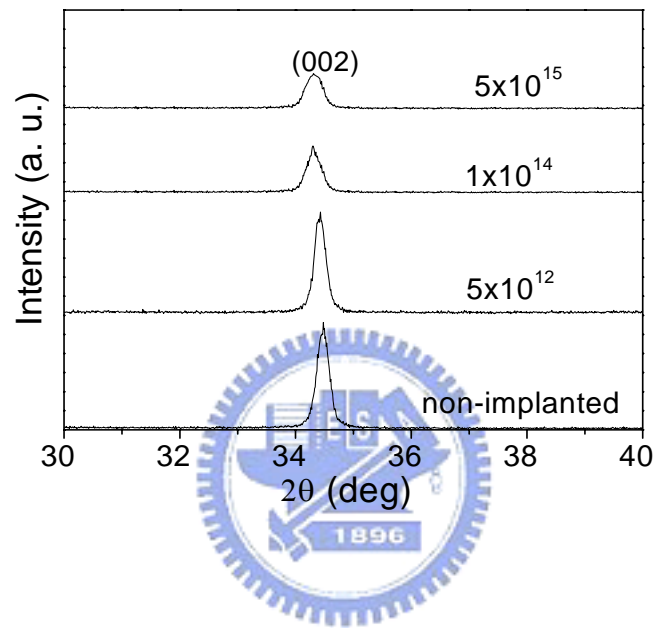
Fig. 3.2. XRD patterns of ZnO films with different fluences annealed in nitrogen

atmospheres at 850 $^{\circ}$C.
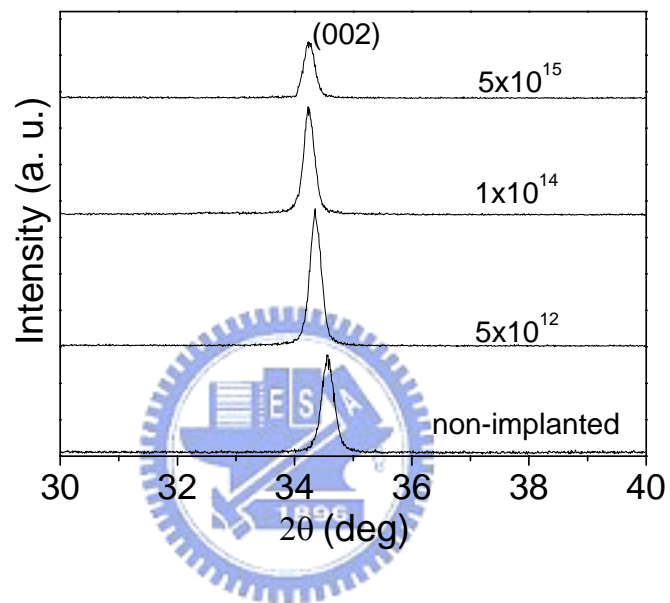
Fig. 3.3. XRD patterns of ZnO films with different fluences annealed in oxygen
atmospheres at 850 ^{o}C.
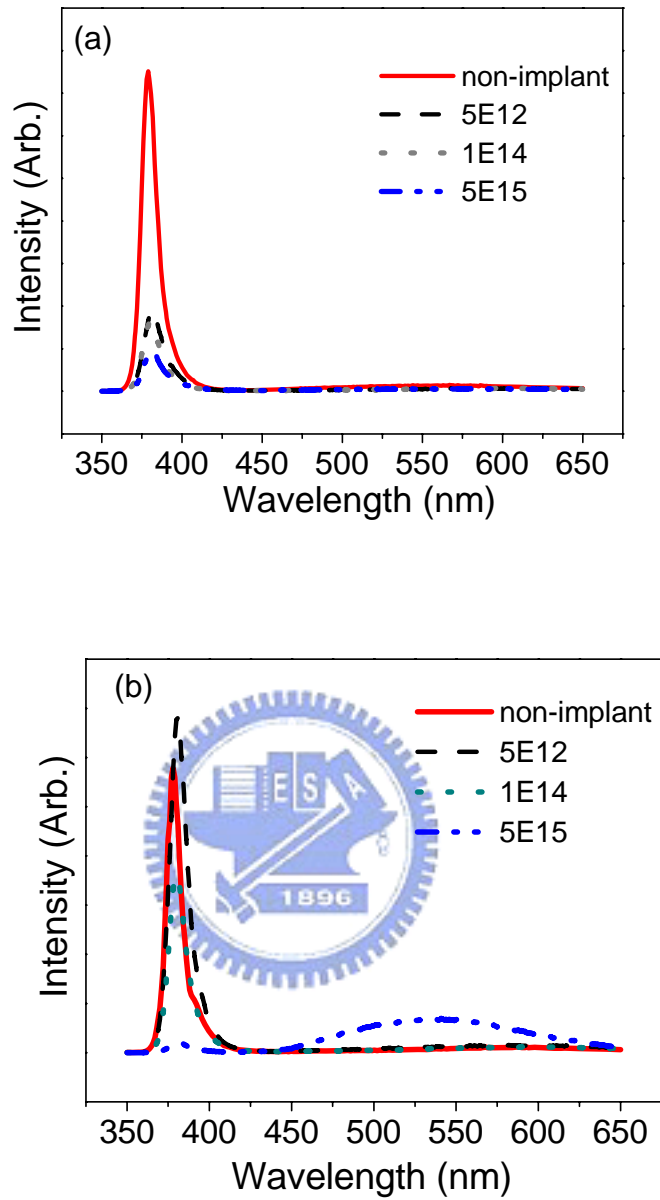
Fig. 3.4. Dependence of fluences conditions on the room temperature PL spectra of the annealed ZnO films treated at 850 $^{\circ}$C in (a) N_2 and (b) O_2 atmospheres.
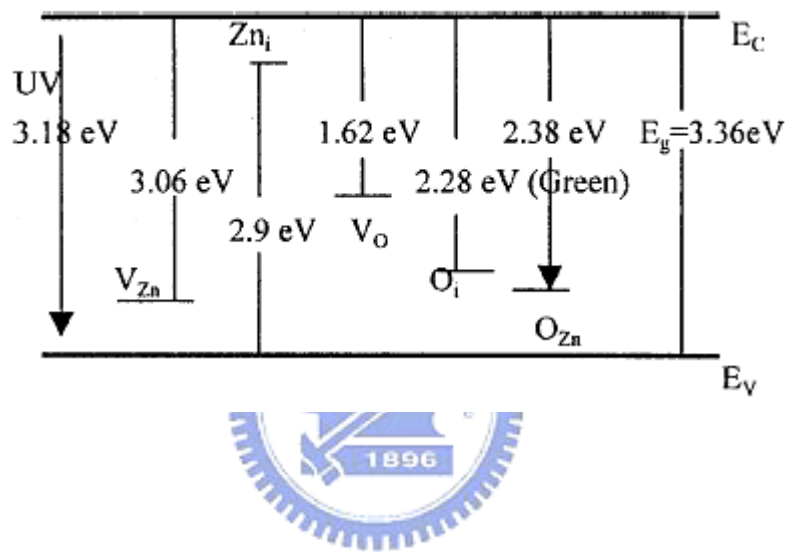
Fig. 3.5. Defects' levels in ZnO film.
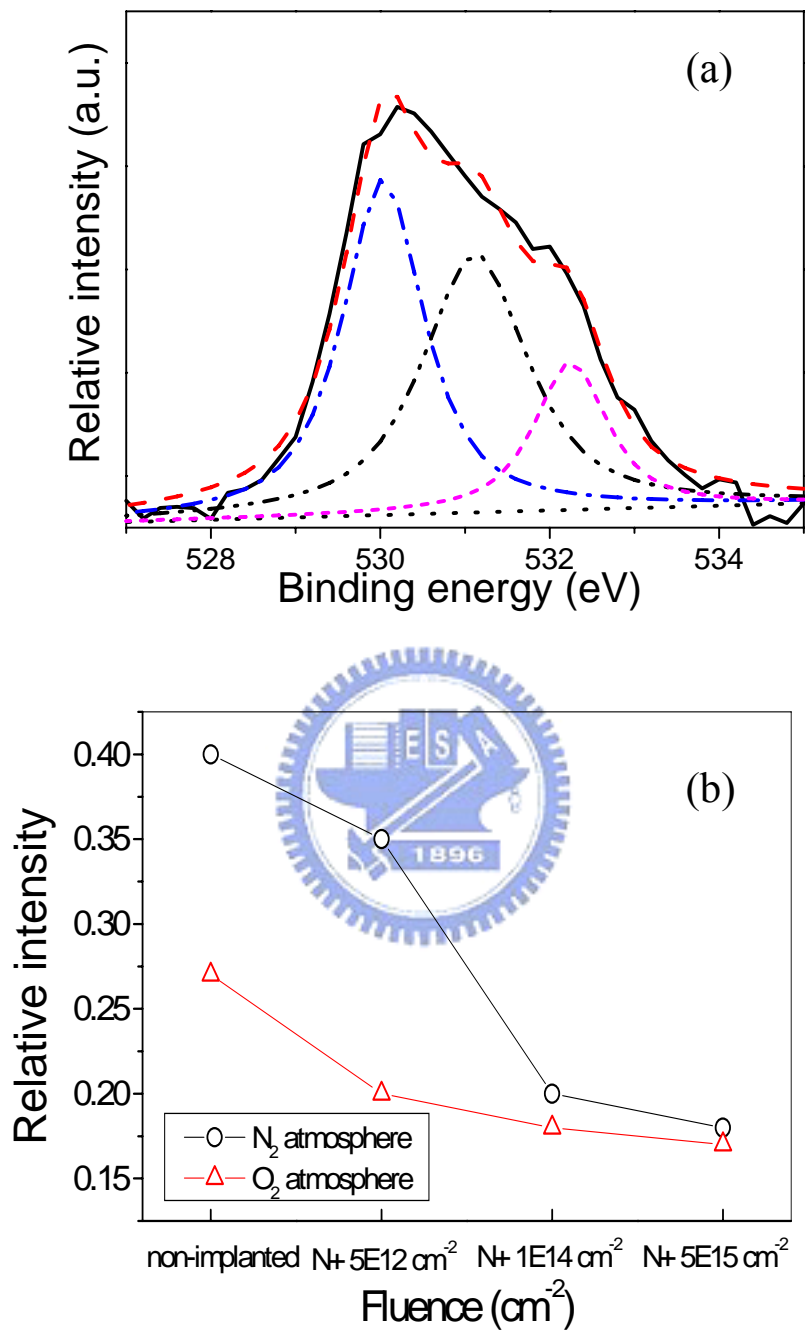
Fig. 3.6. (a) Displays the O1s fitted spectra of non-implanted sample. (b) Dependence of relative intensity of the fitted components centered at O1s 531.25 ± 0.2 eV, on N-implanted fluence in different atmospheres. (a) Displays the O1s fitted spectra of non-implanted sample.

Chapter 4

Physical characteristic of low-temperature grown ZnO nanorods on Si from aqueous solution and annealed at various atmospheres

4.1. Introduction

Wide band gap semiconductors such as ZnO have attracted much attention because of their potential for optoelectronic devices in the blue and ultraviolet spectral regions due to its wide direct band gap of 3.37 eV and a relatively large exciton binding energy of 60 meV.　In the recent years, one-dimensional (1D) nanostructures (nanowires or nanorods) are expected to further lower the lasing threshold because of quantum effects that result in the enhancement of density of states near the band edges and radiative recombination due to carrier confinement. [53] Different approaches have been used to synthesize 1D solid nanostructures including metal-organic-chemical vapor deposition method, [54] vapor-liquid-solid growth, [55] solution-liquid-solid method, [56] template-mediated growth method, [57] electron-beam lithography. [58] However, so far, no systematical studies were performed to investigate the effect of annealing atmospheres on the relationship between the structure and optoelectronic properties of the ZnO nanorods grown in

liquid solution. Therefore, in this study, Raman spectroscopy, X-ray diffraction (XRD), electron paramagnetic resonance spectrometry (EPR), and extended X-ray absorption fine structure (EXAFS) technique will be used to characterize ZnO nanorods and investigate the effect of annealing atmosphere on the PL properties of ZnO nanorods.

4.2. Experiment procedure

Both precursors of methenamine ($C_6H_{12}N_4$) and zinc nitrate hexahydrate [$Zn(NO_3)_2 \cdot 6H_2O$] were used for preparing the solution to grow ZnO nanorods (ZNs). The ZnO thin films were deposited on Si substrates by rf magnetron sputtering following our previous report. [59] The ZnO_f/Si substrates were then placed inside the aqueous solution at 75 ^{o}C for 10 h. After that, the substrates were removed from the aqueous solutions, rinsed with distilled water, and dried at room temperature overnight. After annealed at 850 ^{o}C in various atmospheres, the structural characteristics of the ZnO nanorods were analyzed by scanning electron microscopy (SEM/EDX, JEOL-6500F), and transmission electron microscopy (Philips Tecnai 20). The crystal structure was determined using X-ray diffraction (XRD) with CuKα radiation. Photoluminescence (PL) of the ZnO nanorods were performed by the excitation from 325 nm He–Cd laser at room temperature. Zinc K-edge X-ray absorption spectra were recorded at the wiggler beamline BL17C at National

Synchrotron Radiation Research Center (NSRRC). The electron storage ring was

operated at energy of 1.5 GeV and a current of 120–200 mA. The EXAFS function,

so-called $\chi(k)$ data, was obtained by subtracting the post-edge background from the

overall absorption data followed by normalization with respect to the edge step. A

polycrystalline ZnO powder (Cerac, 99.9%) was used as a reference standard. The

EPR measurements were performed using an *X*-band (9.776 GHz) Bruker

spectrometer at room temperature. Raman spectroscopy was also conducted as a

supplementary tool to identify structural information.

4.3. Results and discussion

4.3.1. Microstructure and phase evolution
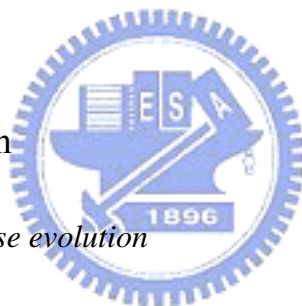
Fig. 4.1 shows the top-view field-emission scanning electron microscope image

of the ZnO nanorods annealed at 850 ^{o}C for 1 h in different atmospheres. It can be

observed that some ZnO nanorods tend to be aggregated and lose the hexagonal shape

especially for the sample annealed in O_2 and air atmospheres. The space group of the

hexagonal wurzite ZnO belongs to C_{6V}^{4} (*P*6$_3$/ *mc*) with two formula units per

primitive cell, all atoms occupying 2*b* sites of symmetry C_{3V}. Therefore, there are

Raman-active phonon modes E$_2$ (low), E$_2$ (high), A$_1$ longitudinal optical (LO), A$_1$

transverse optical (TO), E$_1$ (LO), E$_1$ (TO). According to group theory,

single-crystalline ZnO has three optical phonon modes at point of the Brillouin zone, classified as Raman active modes (A_1+ E_1+2 E_2), Raman silent modes (2B_1), and infrared active modes (A_1+ E_1). E_2 mode is only Raman active and the B1 mode is inactive. Fig. 4.2 shows the room-temperature Raman spectrum of the ZnO nanorods annealed at different atmospheres of (a) N_2, (b) O_2, and (c) air. The observed photon frequencies are E_2 (high) = 437 cm^{-1} and A_1 (LO) = 351 cm^{-1}. The spectrum was recorded with the incident light exactly perpendicular to the top surface of the ZnO nanorods arrays, that is to say, the incident light is parallel to the c-axial direction of the ZnO nanorods. [60] In this case, only both E_2 and A_1 (LO) modes are allowed, while the A_1 (TO) and E_1 (TO) modes are forbidden according to the Raman selection rules. Thus, the absence of the TO mode in the measurements further confirms that the ZnO nanorods are highly *c*-axis oriented.

The peak at 437 cm^{-1} is attributed to ZnO nonpolar optical phonons E_2 vibration mode, which is typical of the one of Raman active branches. The E_2 peak in Fig. 2 is more sharpened when the ZnO nanorods annealed in air compared to that in other conditions. According to the report of Tzolov *et al.*, [61] a significant increase in the defect number of Zn-rich and oxygen vacancies enhances the Raman activity of this phonon mode. It means that the defect density of the ZnO nanorods annealed in air is more than that annealed in both O_2 and N_2 atmospheres.

Generally, at higher temperatures, Schottky disorder may occur as follows:

$$Nill \quad \rightarrow \quad V_{Zn}'' + V_O^{\bullet\bullet} \tag{4.1}$$

When the ZnO was annealed at a higher temperature, a large number of zinc element

could be vaporized from the ZnO and induce the formation of defects as illustrated in

Eq. 4.1. Therefore, it is possible for the formation of a certain amount of Zn

interstitials and oxygen vacancies on the surface of the ZnO nanorods after air

annealing.

When annealed in nitrogen atmosphere at a high temperature, the as-grown ZnO

nanorods can be considered as annealed in reductionlike atmosphere (a much lower

oxygen pressure). Although the oxygen could be evaporated from the ZnO and many

oxygen vacancies were produced, in this condition, it is possible for a certain amount

of nitrogen ions to occupy oxygen sites especially on the surface of the ZnO nanorods.

Therefore, the defect density could be reduced for the ZnO nanorods after nitrogen

annealing.

$$ZnO \xrightarrow{\ N_2\ } Zn_{Zn} + N_O + \frac{1}{2}O_2 \tag{4.2}$$
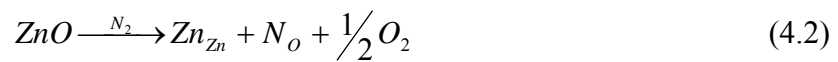
Similar phenomenon was reported by Wang *et al*., that with the incorporation of

nitrogen into ZnO film, the intensity of E_2 peak decreased. [62]

However, if the annealing atmosphere was exchanged using the oxygen

atmosphere for annealing the ZnO nanorods, the oxygen vacancies will be reduced

according to Eq. 4.1. Therefore, the defect density can be also decreased, leading to a

decreased E_2 peak intensity.

4.3.2. Spectroscopic characterization

Fig. 4.3 shows the photoluminescence spectra of the ZnO nanorods annealed at

different atmospheres (N_2, O_2, and air). The UV emission corresponds to the near

band-edge emission, and the green emission peak is commonly referred to as a

deep-level or trap-state emission. The green transition has been attributed to the singly

ionized oxygen vacancy in ZnO and the emission results from the radiative

recombination of a photogenerated hole with an electron occupying the oxygen

vacancy. [63] The spectrum is usually characterized by a sharp UV band and small

green light emission. It was found that the ZnO nanorods annealed in N_2 atmosphere

display a maximum UV peak because the near band-edge may represent transition

from singly ionized nitrogen acceptors to shallow donor. The nitrogen ions probably

have the opportunity to be in the nonparamagnetic singly ionized state (N^-) for the

N_2-annealed sample in the high temperatures. [64] Furthermore, because the nitrogen

has a smaller ionic radius than oxygen, it can be easily trapped in the ZnO nanorods to

reduce intrinsic defects. Therefore, the surface defects can be reduced and thus the

UV peak intensity can be further enhanced compared to the sample annealed in air.

The electron paramagnetic resonance spectrometry (EPR) is an effective method for investigating the electron spin state and the structure of the surface of nanosized crystallines. The ZnO is generally antimagnetic, as can be proved from theory or experiments; that is, the undoped ZnO does not have the EPR signal. However, the ZnO nanorods show a strong EPR signal with a g factor of 1.96. The $g \approx 1.96$ signal is attributed to singly ionized oxygen vacancy defects (V_O^+) in the ZnO matrix. [65] Qualitative observation of the 850 ^{o}C-annealed ZnO nanorods reveals that the EPR spectra are not significantly different for those samples annealed under different atmospheres as shown in Fig. 4.4. This may be attributed to the fact that the ZnO nanorods structures are not apparently changed compared to the as-grown sample at room temperature. However, from the oxygen vacancy defects (V_O^+), the intensity of the g factor (≈ 1.96) is $N_2 < O_2 <$ air, because the nitrogen ion in the annealed sample could be in the nonparamagnetic singly ionized state (N^-) which can easily occupy the oxygen vacancies. [12] This can further support the PL spectra of ZnO nanorods shown in Fig. 4.3. The ZnO nanorods annealed in N_2 atmosphere exhibit a weaker green emission peak than that in air atmosphere. In other words, a stronger UV peak was detected for the ZnO nanorods annealed in N_2 atmosphere.

Fig. 4.5 shows pseudoradial distribution functions obtained from k^3-weighted Fourier transforms of the as-grown ZnO nanorods annealed at 850 ^{o}C for 1 h in

various atmospheres. The local structural parameters, such as the interatomic distance, coordination number, and Debye-Weller factor are measurements of disorder of neighboring atoms around an absorbing atom that can be extracted from the EXAFS function. From the Fourier transform of the EXAFS function shown in Fig. 5.5, the first shell bond distance around Zn^{2+} is ~1.47 Å which is close to the Zn–O bond length (~1.47 Å) of a standard ZnO sample. A second intense peak, labeled Zn–Zn, is observed for ZnO. It was found that those peaks are not significantly different. This indicates that the local structure around Zn^{2+} ions in those samples is similar. In other words, the annealing atmosphere shows no apparent influence on the deep-level defects of ZnO nanorods except that some ions or are possibly trapped adsorbed on the surface of the ZnO nanorods.
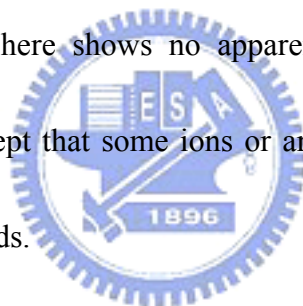
4.4. Conclusions

High-density ZnO nanorods can be vertically grown on Si substrate from aqueous solution via a simple low-temperature process. After annealed in various atmospheres, the ZnO nanorods exhibit different PL spectra. A maximum UV emission was observed for the ZnO nanorods annealed in N_2 atmosphere which may be correlated with the decrease in defect density as evidenced in Raman and EPR. However, the EXAFS analysis demonstrates that the effect of annealing atmosphere on the deep-level defects of ZnO nanorods is confined in local surface area.
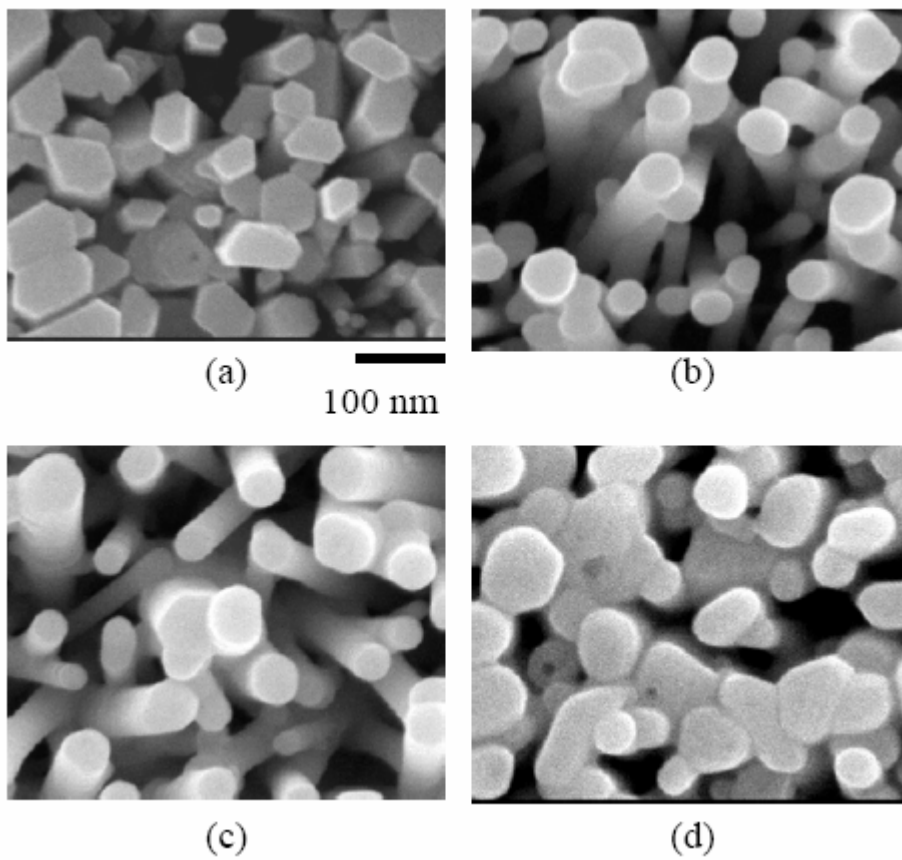
Fig. 4.1. The morphology of annealed ZnO nanorods. (a) Not annealed ZnO nanorods, and annealed in (b) N_2, (c) O_2, and (d) air at 850 $^{\circ}$C/1h.
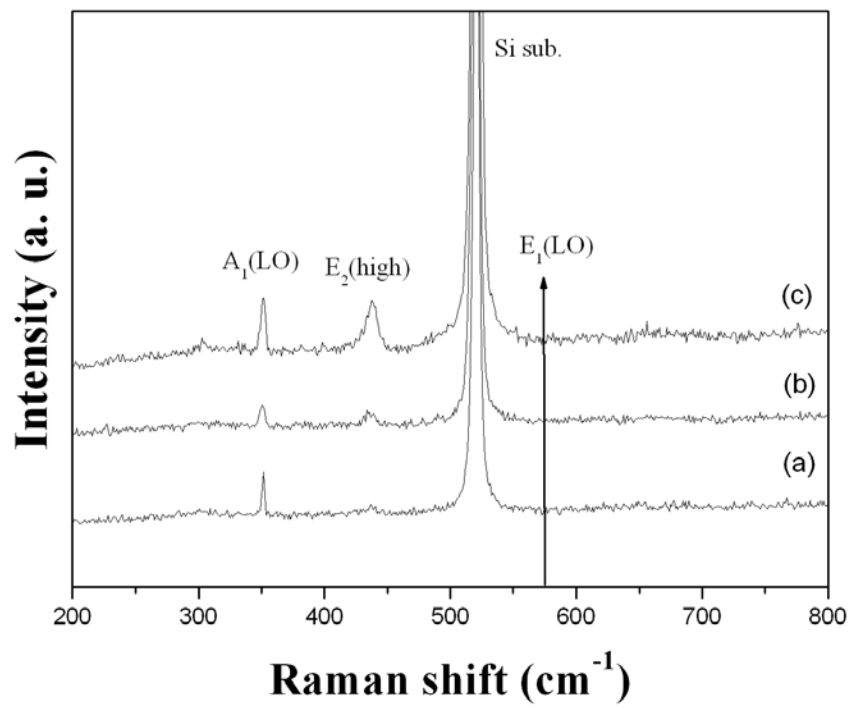
Fig. 4.2. Room-temperature Raman spectrum of the ZnO nanorods annealed in (a) N_2,

(b) O_2, and (c) air atmospheres.
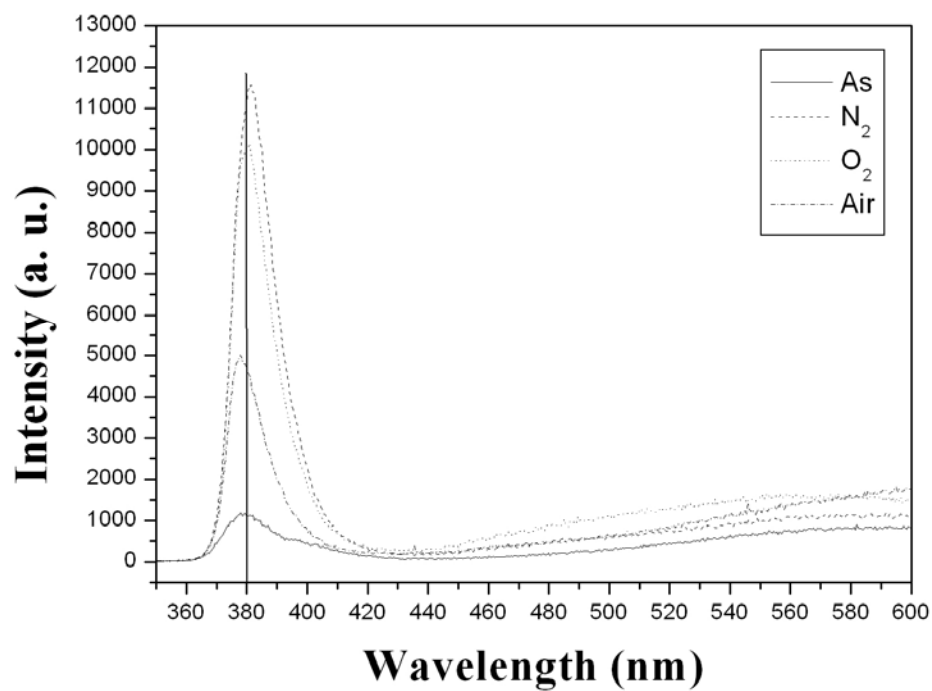
Fig. 4.3. PL spectra of as-grown ZnO nanorods annealed in various atmospheres at 850 $^{\circ}$C for 1 h.
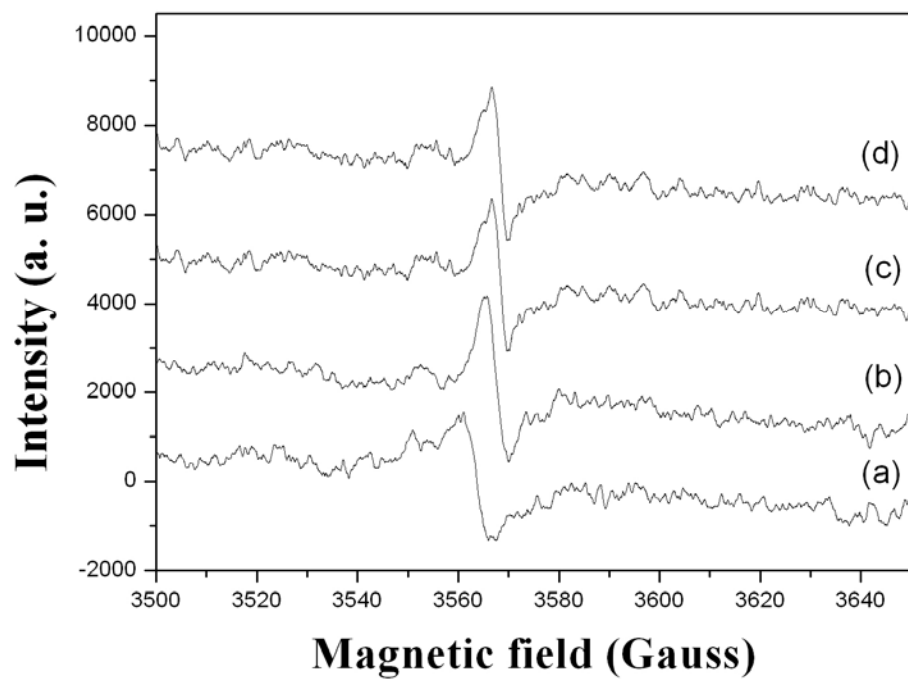
Fig. 4.4. EPR spectra of (a) as-grown and annealed ZnO nanorods in (b) N_2, (c) O_2, and (d) air at 850 ^{o}C/1 h.
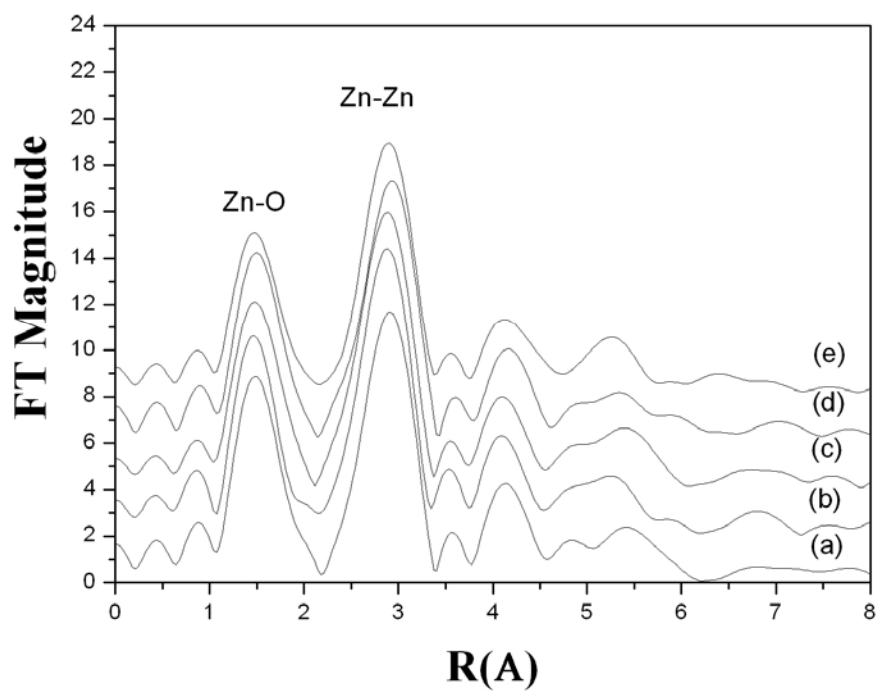
Fig. 4.5. Fourier transform of the EXAFS function at the Zn K edge for (a) as-grown

and annealed ZnO nanorods annealed at 850 ^{o}C for 1 h in (b) N_2, (c) O_2, and

(d) air atmosphere ; (e) ZnO powder standard.

Chapter 5

Effect of phase transformation on photoluminescence behavior of ZnO:Eu prepared in different solvents

5.1. Introduction

Wide band-gap materials always present good potential for full color phosphors. [66] Zinc oxide is one of the wide band-gap materials and shows versatile applications. [67-69] However, a pure red emission could not be obtained since the sharp red emission was also accompanied by a broad green emission due to self-activated centers. It is well known that zinc oxide easily produces intrinsic defects such as interstitial zinc ($Zn_i^{\bullet\bullet}$) and oxygen vacancy ($V_O^{\bullet\bullet}$). These defects will influence the photoluminescence behavior of ZnO in different ways. [70] The emission characteristics of ZnO doped with various impurities have been extensively studied. [71-73] Depending on the relative energy of the 4f emitting level, the excitation of RE[3+] is either a direct 4f-4f process or an indirect process. However, it has been reported that the 4f-4f electron emission of trivalent RE[3+] in the ZnO lattice is extremely difficult under UV excitation. Recently, Narahara *et al.* [74] and Park *et al.* [75] have observed a red emission of Eu^{3+} ions from complete quenching of the

EuCl$_3$-doped ZnO phosphors sintered in vacuum. It was claimed that the red emission

is due to an energy-transfer process occurring from the self-activated defect centers in

ZnO host to the Eu^{3+} ion which exists in the form of EuOCl. The addition of a

co-activator such as Li$^+$ is also used to promote the photo-excited RE^{3+} luminescence,

while no apparent enhancement in the luminescence intensity of the Eu^{3+} was

obtained. In addition, it was reported that the existence of OH$^-$ from the solvent will

retards the emission of RE^{3+}. [76] Therefore, more information is required for

successfully developing ZnO:Eu for application in field emission displays (FED).

Several attempts were undertaken to obtain a strong red luminescence from

ZnO:Eu, especially the role of solvent and processing temperature in the

luminescence behavior of ZnO/RE^{3+}. In this work, two solvents, deionized water and

acetone, were used to study the phase transformation of Eu-doped ZnO powder in

terms of ball-milling and sintering temperature. The effect of phase transformation on

the luminescence behavior of ZnO/RE^{3+} was also elucidated.

5.2. Experimental procedures

Europium doped zinc oxide (Eu:ZnO) powder was prepared by mixing 99.99

purity ZnO and Eu$_2$O$_3$. The powder mixture was ball-milled in a polyethylene ball

with Y$_2$O$_3$-stabilized ZrO$_2$ grinding media in both deionized water (with OH$^-$) and

acetone (without OH⁻) solvents. After dried, the powder was then sintered at different

temperature (600~1000 $^{\circ}$C) for 1 h in air and subsequently cooled to room

temperature. The crystal phases have been detected by X-ray diffraction (XRD)

(MAC Science, M18X) (Tokyo, Japan) with Cu Kα radiation. Luminescent properties

at room temperature have been characterized by photoluminescence (PL)

measurements under 325 nm and 532 nm excitation wavelength (λ) (FL F4500,

Hitachi). The surface microstructure and chemistry were studied by scanning electron

microscopy (SEM) and energy dispersive X-ray analysis (EDX).

5.3. Results and discussion
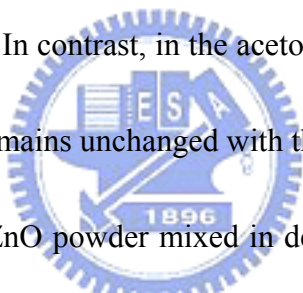
5.3.1. OH⁻ effect

Prior to ball-milling in deionized water, pure Eu_2O_3 powder is a cubic structure

according to XRD patterns in Fig. 5.1 (a). However, after ball-milling, it was found

that cubic Eu_2O_3 powder was transformed into hexagonal $Eu(OH)_3$ as shown in Fig.

5.1 (b). In order to check OH⁻ effect, acetone instead of deionized water was used in

the ball-milling but no apparent difference was detected. Therefore, it can be

assumed that the existence of OH⁻ ion promotes the formation of the $Eu(OH)_3$ phase.

Park et al. studied the photoluminescence characteristics of ZnO: $EuCl_3$ phosphors

and found that Eu can exist in the ZnO host lattice as EuOCl, [75] implying the

possibility of incorporation of Eu^{3+} into the ZnO lattice.

Fig. 5.2 shows the XRD patterns of 0.5 wt% Eu-doped ZnO powder mixed in deionized water and acetone, respectively. It was observed that both of them present a different phase evolution as function of the sintering temperature. In deionized water, the peak intensity at $2\theta = 28.4$ (corresponding to the Eu_2O_3 phase) becomes stronger with the sintering temperature (Fig. 5.2 (a)). This phenomenon was tentatively related to the formation of $Eu(OH)_3$ as evidenced from Fig. 5.1 (b). An increase in the sintering temperature will lead to the decomposition of $Eu(OH)_3$ and promotes the formation of the Eu_2O_3 phase. In contrast, in the acetone solvent, the peak intensity of Eu_2O_3 shown in Fig. 5.2 (b) remains unchanged with the sintering temperature.

The 0.5 wt% Eu-doped ZnO powder mixed in deionized water and acetone was measured by PL (excitation wavelength 532 nm). Fig. 5.3 shows that all PL spectra are characteristic of the main Eu^{3+} red emission and this is due to Eu^{3+} transmission from $^5D_0$ to ^7F_j (j = 0~4) energy level. The sensitively red PL transmission for Eu^{3+} is $^5D_0 \rightarrow {}^7F_2$. As illustrated in Fig. 5.3 (a), at low temperatures, the $^5D_0 \rightarrow {}^7F_2$ of Eu^{3+} emission is still influenced by the OH^- quench effect and the PL intensity is very weak for the samples mixed in deionized water, in contrast to the sample mixed in acetone. Apparently, the OH^- plays an important role in the PL intensity which is consistent with the observation of XRD in Fig. 5.2. This demonstrates OH^- to quench the

emission of RE^{3+} of the ZnO-Eu_2O_3 powder mixed in deionized water.

The emission intensity of $^5D_0 \rightarrow {^7F_{1-4}}$ is also dependent on the sintering conditions. The η_{21} and η_{41} represent the relative intensity ratios of $^5D_0 \rightarrow {^7F_2}$ to $^5D_0 \rightarrow {^7F_1}$ and $^5D_0 \rightarrow {^7F_4}$ to $^5D_0 \rightarrow {^7F_1}$, respectively, and are listed in Table 5.1. These two values indicate the degree of short-range order and long-range order of Eu^{3+} in the crystal lattice, respectively. For the water-milled sample, the η_{21} value increases with increasing temperature. At a low sintering temperature of 600 $^{\circ}$C, the OH^- ion diffuses into Eu_2O_3 lattice and changes the short-range order and η_{21} value. However, at high temperatures, $Eu(OH)_3$ will be decomposed and the η_{21} value will be increased. The phenomenon can be used to elucidate why the $Eu:ZnO$ samples show different PL behavior at different sintering temperature in deionized water in comparison with that in acetone (Fig. 5.3).
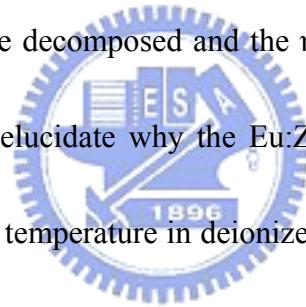
5.3.2. Eu amount

The addition of Eu_2O_3 may behave as donor through the substitution of Zn-site and promote zinc-site vacancy (V''_{Zn}) formation as shown below.

$$Eu_2O_3 \rightarrow 2\,Eu^{\bullet}_{Zn} + V''_{Zn} + 3O^x_o \tag{5.1}$$
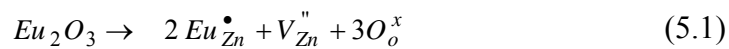
Eq. 5.1 illustrates that the doping effect forms a shadow level ($Eu^{\bullet}_{Zn}$) below the conduction band and increases the conductivity. In order to confirm the possibility

of the substitution of Eu for Zn in the ZnO host, magnified XRD patterns of ZnO (1 0

1) peak as a function of Eu amount were studied. As illustrated in Fig. 5.4, the peak

change in the XRD patterns indicates a minor substitution Eu for Zn in the ZnO lattice

($Eu_{Zn}^{\bullet}$) but above 0.2 wt%, the presence of Eu aggregates was detected from the

heavily Eu-doped samples.

Fig. 5.4 shows that the Eu could substitute for Zn, where even a smaller amount

would result in the formation of Zn interstitials. However, at higher temperatures,

Schottky disorder may occur as follows.

$$Nill \rightarrow V_{Zn}^{''} + V_O^{\bullet\bullet} \tag{5.2}$$

More $V_{Zn}^{''}$ defects benefit the reverse reaction of Eq. 5.1 and decrease $Eu_{Zn}^{\bullet}$ defect

concentration. Therefore, the probability of Eu^{3+} ion to occupy the $V_{Zn}^{''}$ sites is also

decreased, indicating that the solubility of Eu^{3+} ion into ZnO lattice will be limited.

Therefore, at a higher sintering temperature, more $Zn_i^{\bullet\bullet}$ and $V_{Zn}^{''}$ defects will be

easily created and this leads to the formation of the Eu_2O_3 phase. As evidenced from,

The Eu mapping of the 0.5 wt% Eu-doped ZnO sample (Fig. 5.5) evidences that with

increasing sintering temperature from 600 $^{\circ}$C to 1000 $^{\circ}$C, more separated Eu_2O_3

particles are widely distributed among ZnO grains. However, as the ZnO was doped

with less than 0.2 wt % Eu and sintered at 1000 $^{\circ}$C, no separated Eu_2O_3 particles were

detected among ZnO grains, this indicating that the solution limit in the Eu-doped

ZnO system is below 0.2 wt% Eu, in agreement with the result shown in Fig. 5.4.

According to the Einstein relations: $\dfrac{D_n}{\mu_n} = \dfrac{D_p}{\mu_p} = \dfrac{kT}{e}$ and conductivity

$\sigma = e\mu_n n$ (where μ_n is the n-type mobility, D_n the electron diffusion coefficient

for n-type semiconductor), the conductivity (σ) is proportional to $\dfrac{e^2}{T}$. The

temperature dependence on conductivity of Eu-doped ZnO can be plotted and shown

in Fig. 5.6. The slope (energy level of $Eu_{Zn}^{\bullet}$) can be calculated to be approximately

0.19 eV below the conduction band, and the energy level is closer to the conduction

band than these for $Zn_i^{\bullet\bullet}$ (0.22 eV). This indicates that $Eu_{Zn}^{\bullet}$ defect may exist in the

ZnO lattice and the electrons are jumped easily from the conduction band to $Eu_{Zn}^{\bullet}$

level than to $Zn_i^{\bullet\bullet}$ level.

5.3.3. Effect of excitation wavelength

It is well known that when exciting the semiconducting substrate with a beam of

wavelength lower than 385 nm, no emission from the rare-earth dopant could be

observed. Therefore, as a short wavelength beam of 325 nm was used to excite the 0.5

wt% Eu-doped ZnO samples, it was very difficult to observe the red emission of the

Eu^{3+} from the sample mixed in deionized water. In other words, only broad green (540

nm) and near UV (380 nm) region emissions are observed in Fig. 5.7 (a). The UV

emission band is due to ZnO intrinsic emission. The green emission results from zinc

interstitials and oxygen vacancy. The disappearance of the red emission excited at 325

nm wavelength is probably related to the shielding effect due to the existence of the

$Eu_{Zn}^{\bullet}$ level. In contrast, for the Eu-doped ZnO samples milled in acetone, a red

emission can be detected under excitation at 532 nm wavelength (Fig. 5.3 (b)) and

325 nm wavelength (Fig. 5.7 (b)). This may possibly suggest that the generated

excitation electron from Eu_2O_3 does not completely transfer to $Zn_i^{\bullet\bullet}$ site and that no

OH^- quenching effect occurs in the acetone-mixed sample.

5.4. Conclusions

The phase transformation of Eu-doped ZnO powders prepared in different

solvents on luminescence behavior was studied.   It was found that the solvent plays a

very important role in the ZnO-Eu_2O_3 system. When the powder was mixed in

deionized water, it leads to the existence of Eu^{3+} ion in the ZnO matrix. The intrinsic

red photoluminescence ($^5D_0 \rightarrow ^7F_2$) of Eu^{3+} is easily shielded by the ZnO intrinsic

defect when the samples were excited with a short wavelength of 325 nm, because the

energy level of $Eu_{Zn}^{\bullet}$ (0.19 eV) is closer to the conduction band than for $Zn_i^{\bullet\bullet}$ (0.22

eV). Therefore, no red emission can be detected. However, this work demonstrates

that a sharp red emission can be promoted by treating the Eu-doped ZnO sample in

acetone solvent.

Table 5.1. Relative intensity ratio of $^5D_0 \rightarrow {^7F_2}$ to $^5D_0 \rightarrow {^7F_1}$ and $^5D_0 \rightarrow {^7F_4}$ to $^5D_0 \rightarrow {^7F_1}$

as a function of sintering temperature for ZnO:Eu powders

Sample	Temperature	Solvent	η_{21}	η_{41}
	600 ^{o}C	water	0.54	0.43
ZnO:Eu 0.5wt%	800 ^{o}C	water	1.11	0.55
	1000 ^{o}C	water	1.35	0.48
	600 ^{o}C	acetone	1.34	0.45
ZnO:Eu 0.5wt%	800 ^{o}C	acetone	1.38	0.478
	1000 ^{o}C	acetone	1.25	0.32
ZnO:Eu 0.2wt%	1000 ^{o}C	water	0.65	0.39
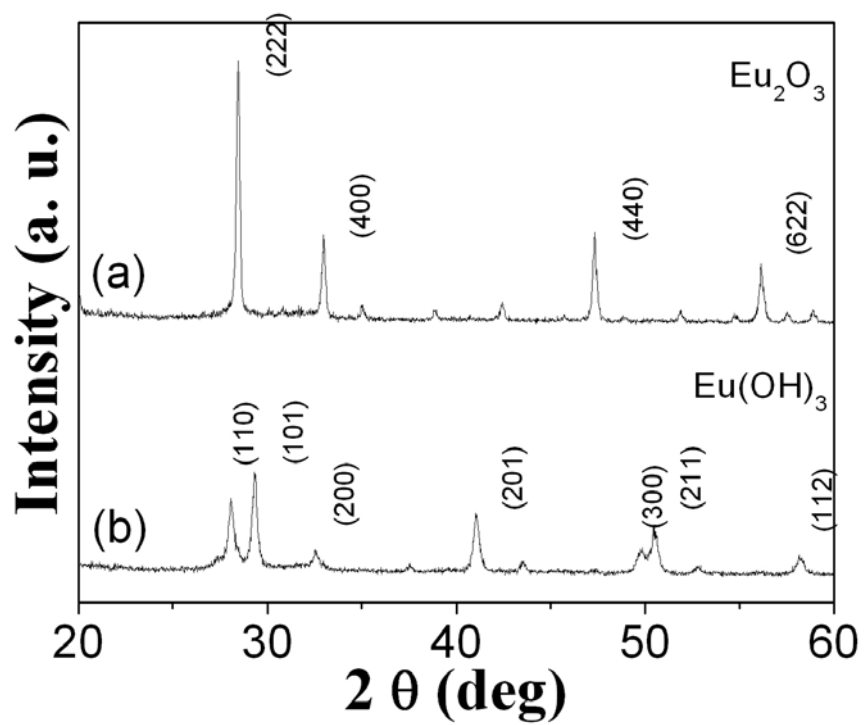
Fig. 5.1. XRD patterns of the Eu_2O_3 powder (a) without and (b) with ball-milling in

deionized water.
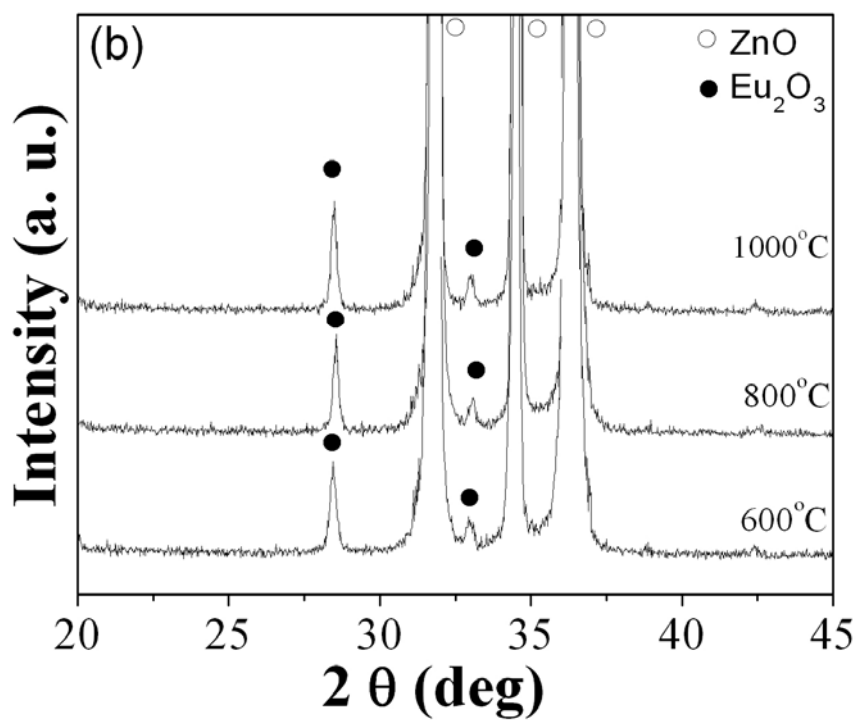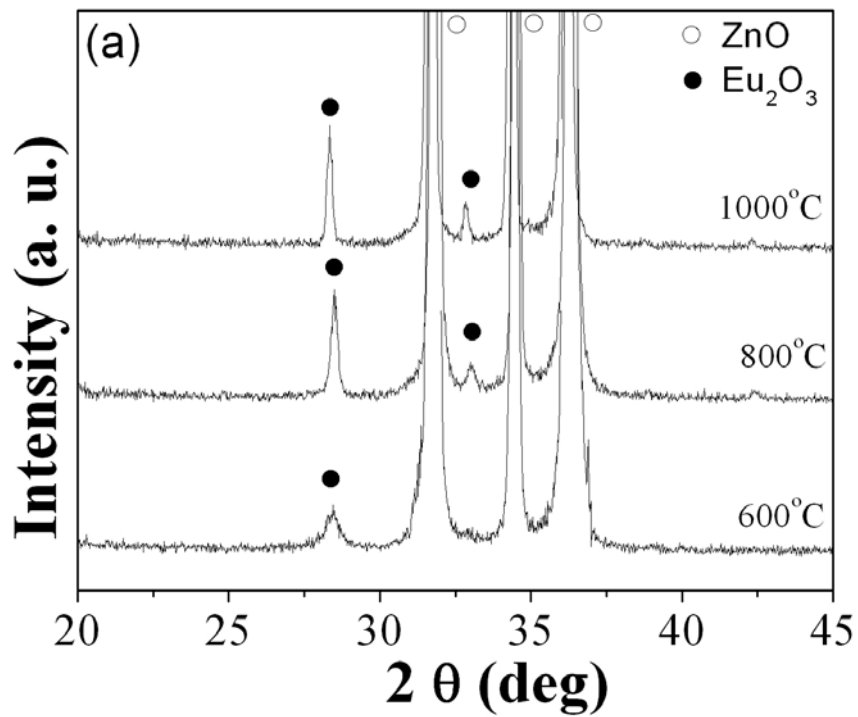
Fig. 5.2. XRD patterns of 0.5 wt% Eu-doped ZnO powder mixed in (a) deionized

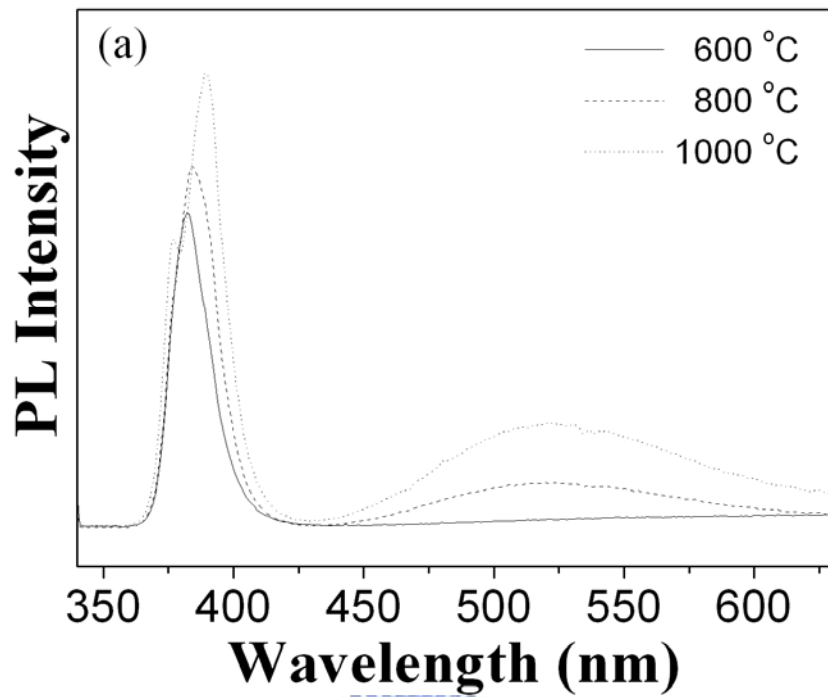water and (b) acetone and then sintered at 600-1000 ^{o}C/1 h.
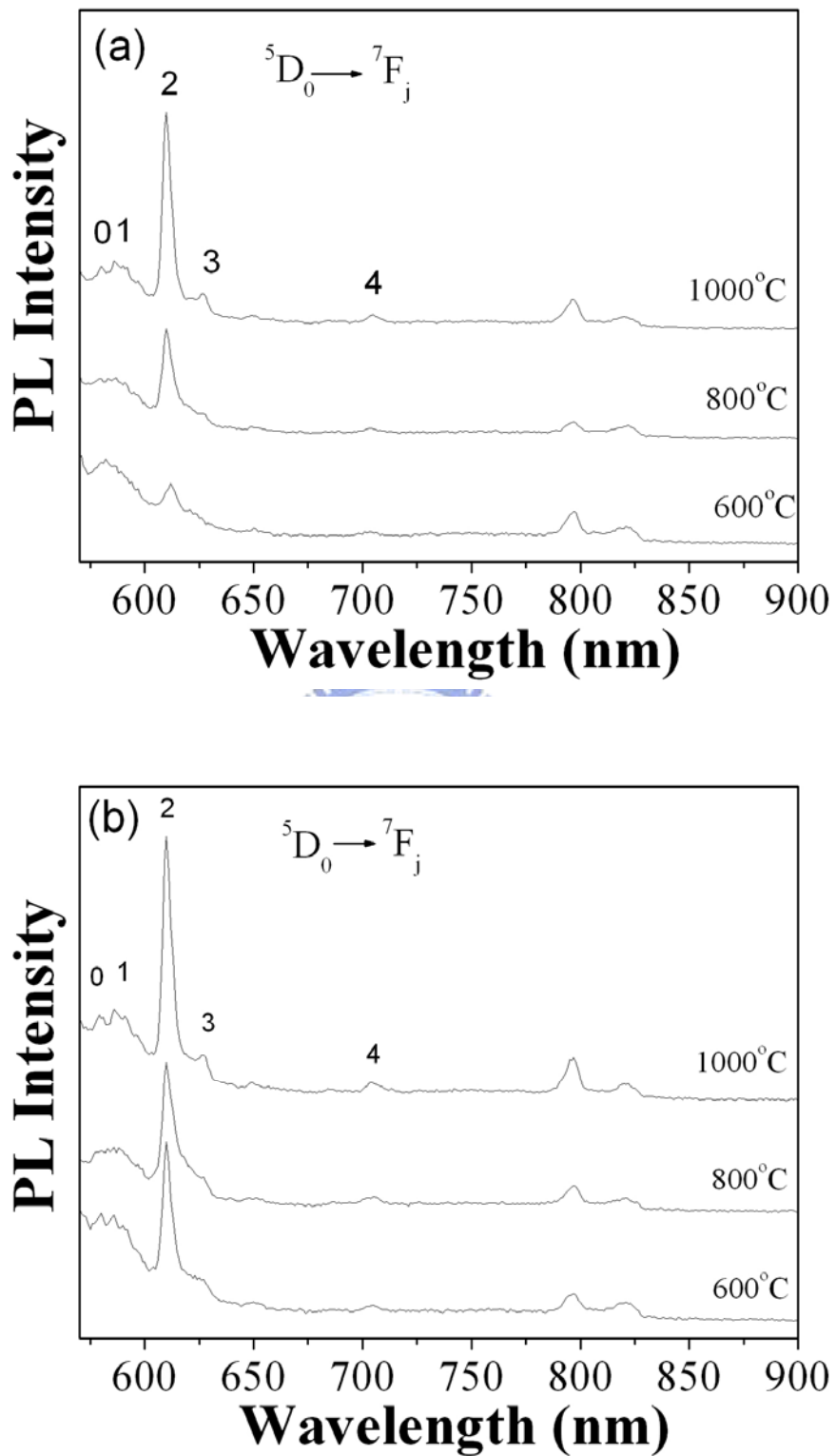
Fig. 5.3. PL spectra of 0.5 wt% Eu-doped ZnO powder mixed in (a) deionized water

and (b) acetone and sintered in air (excitation wavelength 532 nm).
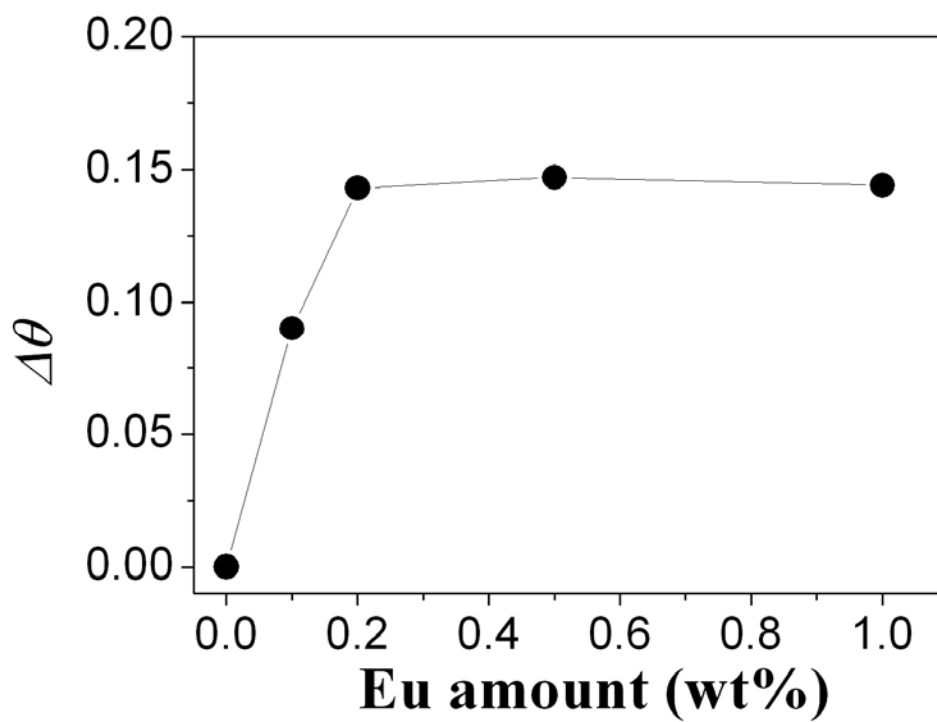
Fig. 5.4. Peak shift in ZnO (1 0 1) peak as a function of Eu amount.
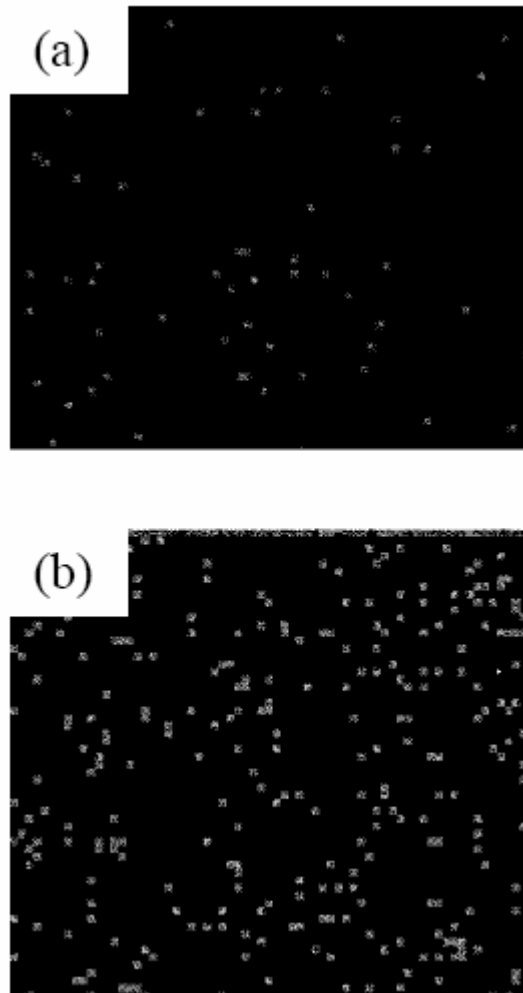
Fig. 5.5. Eu mapping of the 0.5 wt% Eu-doped ZnO sample sintered at (a) 600 ^{o}C and

(b) 1000 ^{o}C in air.
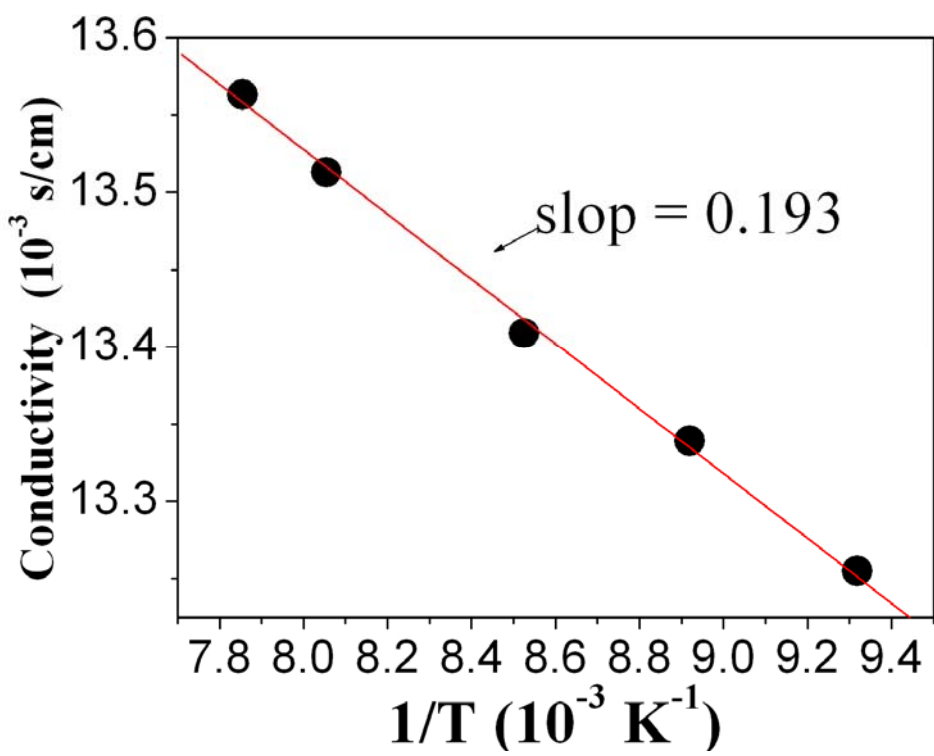
Fig. 5.6. Temperature dependence on conductivity of Eu-doped ZnO.
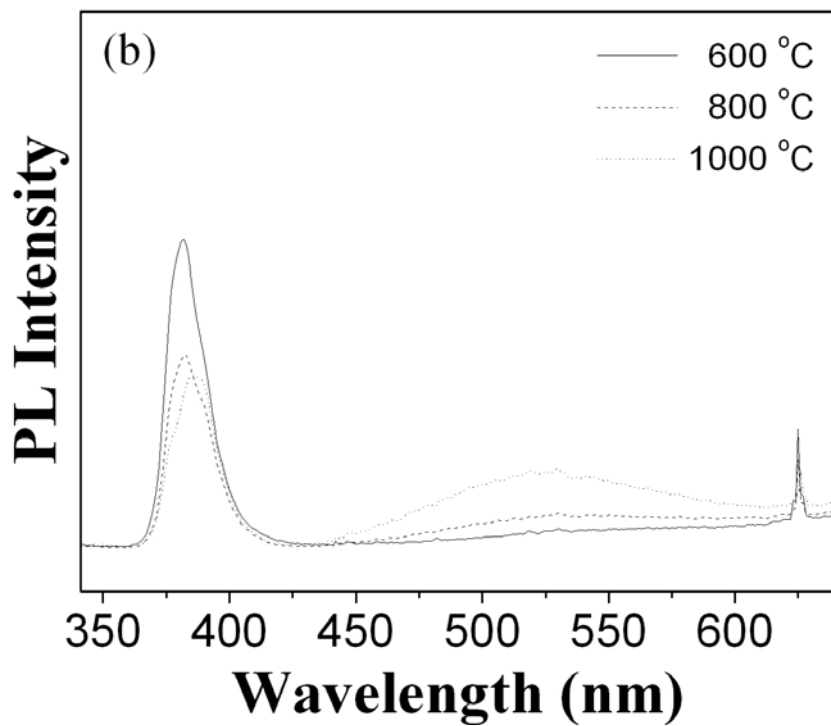
Fig. 5.7. PL spectra of 0.5 wt% Eu-doped ZnO powder mixed in (a) deionized water

and (b) acetone in air (excitation wavelength 325 nm).

Chapter 6

In-situ synthesis and physical characteristics of $ZnAl_2O_4$ nanocrystalline and $ZnAl_2O_4$/Eu core-shell structure via hydrothermal route

6.1. Introduction

Zinc aluminate ($ZnAl_2O_4$) spinels are widely used as catalytic and electronic materials. [77-79] Recently, nanostructured or nanocrystalline zinc aluminates are of interest due to their improved properties such as thermal stability and hardness, etc. So far, many methods have been developed to prepare nanocrystalline $ZnAl_2O_4$ powders [80-81] such as solid-state reaction, sol-gel and hydrothermal. Wrzyszcz developed a two-stage hydrothermal process at $160\ ^oC$ /4 h to obtain $ZnAl_2O_4$. [82] During the synthesis, the processing parameters, including reaction temperature and time, precursor concentration and pH value have to be controlled because of the complex dissolution-precipitation and transformation behavior. Although the synthesis of $ZnAl_2O_4$ spinel nanocrystalline powder has been investigated, it is important to develop a simple route on the synthesis of spinels.

On the other hand, so far, most of the researches in this area have been focused on noble-metal nanocores and molecular shells. Few studies have paid attention to nanomaterials with rear-earth metal shells. [83] Therefore, in this paper, a simple route to develop $ZnAl_2O_4$ nanopowder will be proposed through hydrothermal processing. In addition, after surface treatment with R-OH, the development and

photoluminescence properties of $ZnAl_2O_4$/Eu core-shell structure will be discussed.

6.2. Experimental

Both precursors of aluminum chloride hexahydrate (Aldrich) and zinc chloride (Aldrich) were used in this work to study the formation of nanocrystalline $ZnAl_2O_4$ (ZA) through hydrothermal process. The molar ratio of Zn/Al is fixed at 1:2 and the pH value was controlled by the addition of 3M NaOH (Aldrich). After the solution was transferred into Teflon-lined stainless steel autoclaves and kept at reaction temperature (120-180 ^{o}C) for 5-20 h under autogenous pressure (heating/cooling rate of 1 ^{o}C min^{-1}). Thereafter, the solid material was filtered off, washed with deionized water and then air-dried overnight at 80 ^{o}C. Subsequently, the obtained ZA nanopowders were mixed in methyl alcohol with the addition of surfactant CTAB. The europium nitrate hexahydrate (Merck) solution was then added into the solution with different molar ratio of ZA/Eu to form the micells. After the solution was reacted 200 ^{o}C for 20h. ZA/Eu core-shell powders were obtained.

All the samples were characterized by X-ray diffraction (XRD) with CuKα radiation (λ = 1.5418 Å). The morphology and microstructures of the nanoparticles were examined by transmission electron microscope (TEM) with Philips TECNAI 20. Photoluminescence were performed by the excitation from 325nm He-Cd laser at room temperatures. The FT-IR spectrometer (Bomem, DA8.3) spectra were obtained using KBr disks containing ~1 % sample.

6.3. Results and discussion

6.3.1. Phase development and characterization of $ZnAl_2O_4$

When the precursors were hydrothermally treated under T = 180 ^{o}C for 5 h at

different pH values, different crystalline phases were detected. As illustrated in Fig. 6.1, pure $ZnAl_2O_4$ (ZA) spinel only can be obtained at pH=7, indicating that the formation of ZA phase is very sensitive to the solution pH. For a lower solution pH, i.e. 3.5, Panias *et al*. studied the formation reactions of the hydroxoaluminate complex ions and reported that some of Al^{3+} ions would be transformed into smaller $Al(OH)^{2+}$ (Eq. 6.1) for the precursor solution of pH = 3.5 at 25 ^{o}C [84].

$$Al^{3+} + H_2O \rightarrow Al(OH)^{2+} + H^+ \qquad (6.1)$$
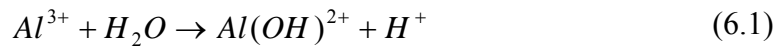
As increasing reaction temperature up to 180 ^{o}C, $Al(OH)^{2+}$ would be further transformed into boehmite AlOOH because the zinc ions (Zn^{2+}) always keep in stable state at a lower pH solution. [85]

$$Al(OH)^{2+} + H_2O \rightarrow AlO(OH) + 2H^+ \qquad (6.2)$$
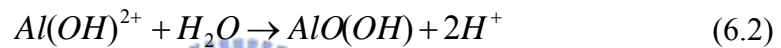
As the solution was controlled at pH = 7/ 180 ^{o}C, $ZnAl_2O_4$ (ZA) spinel was developed. The phase evolution of ZA with reaction temperature at pH = 7 would be further investigated. As shown in Fig. 6.2, it was found that at 25 ^{o}C, only $Al(OH)_3$ was formed following the reaction of Eq. 6.3, meaning that the Zn^{2+} ions still remain in ion state.
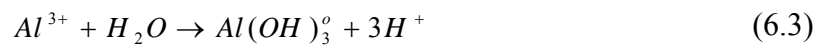
$$Al^{3+} + H_2O \rightarrow Al(OH)_3^o + 3H^+ \qquad (6.3)$$

With an increase of the reaction temperature, at 120 ^{o}C, the $Al(OH)_3$ would further react with Zn^{2+} to form ZnAl layered double hydroxide (ZnAl-LDHs) as demonstrated by XRD in Fig. 6.2, indicating that Zn^{2+} ions can replace Al^{3+} in the $Al(OH)_3$. [86] At a higher reaction temperature (T >120 ^{o}C), more energy was provided to snap ZnAl-LDHs into two layers and promote the formation of ZnO and $Al(OH)_3$. The Zn-Al LDHs will promote the formation of ZnO and $Al(OH)_3$. Then,

both ZnO and Al(OH)$_3$ phases will further react together to form ZA.

At pH = 10.5, the Al^{3+} ions are easily transformed into Al(OH)$_4^-$ at 25 ^{o}C. In addition, in such a high-pH solution, the Zn^{2+} ions tend to form Zn(OH)$_2$ which then can be further transformed into Zn(OH)$_3^-$ and dissolved into the water based on the report by Smith. [87]

$$Zn(OH)_2 \downarrow + OH^- \Leftrightarrow Zn(OH)_3^- \qquad (6.4)$$
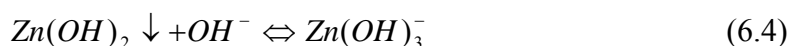
At T < 75 ^{o}C, it was found that ZnO crystalline was formed via hydrothermal route and Al(OH)$_4^-$ was transformed to Al(OH)$_3$. However, with increasing treatment temperature up to 120°C, it was found that Al(OH)$_4^-$ was transformed to Al(OH)$_3$ which will further react with ZnO to form ZnAl$_2$O$_4$. Therefore, the amount of the ZnO crystalline would be decreased and at T =180 ^{o}C, only both ZnO and ZA phases were formed
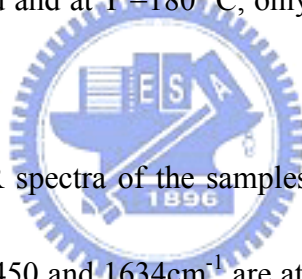
.   Fig. 6.3 shows the FTIR spectra of the samples prepared at various pH values for 180 ^{o}C/5h. The bands at 3450 and 1634cm^{-1} are attributed to OH stretching due to absorbed water molecule. For the sample prepared at pH = 3.5, 180 ^{o}C/5h, Fig. 6.3 (a) shows the typical FTIR spectra of boehmite phase. The bands at 3360, 3094 cm^{-1} are assigned to AlOOH vibration. The other two bands at 1158 and 1067 cm^{-1} correspond to asymmetric and symmetric δ(OH) vibration of AlOOH. Another two bands at 747 and 635 cm^{-1} are assigned to the γ(OH) of AlOOH. In contrast, when the samples were treated at pH = 7 and 10.5, Figs. 6.3 (b) and (c) do not show characteristic bands of boehmite phase. The bands at 569 and 663 cm^{-1} can be attributed to the Al-OH, indicating that some Al(OH)$_3$ still exist in the samples but can't be detected by XRD.

*6.3.2. Particles sized comparison of synthesized ZnAl$_2$O$_4$*

Fig. 6.4 shows the TEM image of ZnAl$_2$O$_4$ particles prepared from the mixed solutions of AlCl$_3$ and ZnCl$_2$ at 150 ^{o}C for 5 h. Table 6.1 summarizes the average particle size of the as-synthesized ZnAl$_2$O$_4$ nanopowders. The crystallite size from XRD method is calculated based on X-ray line broadening of the (311) diffraction peak using Scherrer equation. The lattice parameter is also measured from the (311) diffraction peak using Si as an internal standard. For comparison, BET method is also used to calculate the average particle size from $d = 6/\rho S_w$, where d is the diameter of particles with spherical shape, ρ is powder density of ZnAl$_2$O$_4$ (4.68 g/cm^3), and S_w specific surface area. The specific surface area of ZnAl$_2$O$_4$ powders is dependent on the reaction temperatures and time. As shown in Table 6.1, raising the reaction temperatures or time promotes the increase of the average particle size of ZnAl$_2$O$_4$ crystallite. The average particle size of 5.21 nm, calculated from BET, is smaller than that calculated by the XRD method (6.54 nm) for 150 ^{o}C-treated ZnAl$_2$O$_4$ sample. The particle size difference is due to the different solubility of AlOOH and Al(OH)$_3$ and is explained based on the nucleation theory .

6.3.3. Microstructure and photoluminescence properties of ZnAl$_2$O$_4$/Eu core-shell particles

Nanoparticles have unique property for industry application. However, the shell material may behave as function stabilizer or modifier of core material. First, methyl alcohol was used to modify ZnAl$_2$O$_4$ surface to connect the OH group. Subsequently, surfactant CTAB was coated on the surface of particles to connect Eu, By controlling molar ratio of methyl alcohol/D.I. water, ZA/Eu core-shell particles can be

synthesized. Fig. 6.5 shows the high resolution TEM image of Eu-coated ZA nanoparticle. The thickness of the shell is about 7.8 nm which is almost 1/4 of core diameter.

Fig. 6.6 shows the photoluminescence of ZA/Eu core-shell particles excited by wavelength 390 nm. It was found that different molar ratio of methyl alcohol/D.I. water can lead to different structure morphology of the ZA/Eu and Eu^{3+} emission intensity. As shown in Fig. 6.6 for the sample is excited with $\lambda = 390$ nm, the sample treated with the molar ratio of 2 (R = 2) shows a stronger Eu^{3+} emission from ZA/Eu structure as compared to that treated with 4.375. The peaks at 464 nm and 524 nm are attributed to Eu^{3+} transmission from $^{5}D_{2}$ to $^{7}F_{0}$ and $^{5}D_{1}$ to $^{7}F_{0}$, respectively. The ZA/Eu core-shell structure not only shows Eu^{3+} emission from $^{5}D_{0} \rightarrow {}^{7}F_{2}$ but also the Eu^{3+} emission from depth transition of $^{5}D_{2}$ to $^{7}F_{0}$ is also detected.
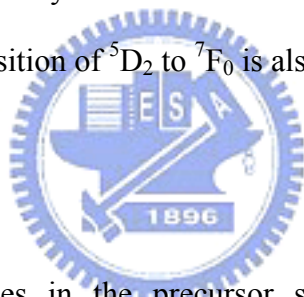
6.4. Conclusions

Depending on pH values in the precursor solution, ZnAl layered double hydroxide (ZnAl-LDH), ZnO, boehmite or gibbsite could be formed. Nanocrystalline $ZnAl_{2}O_{4}$ with average particle size of ~5 nm are hydrothermal synthesized by controlling the precursor solution at pH = 7 at T > 120 ^{o}C for 5h through ZnAl layered double hydroxide (ZnAl-LDH). In addition, the $ZnAl_{2}O_{4}$/Eu core-shell structure can be developed by using the cationic surfactant CTAB. Both $^{5}D_{0}$ to $^{7}F_{2}$ sensitivity energy level and $^{5}D_{2}$ to $^{7}F_{0}$ depth energy level can be detected from the $ZnAl_{2}O_{4}$/Eu core-shell structure.

Table 6.1   Average practical size of synthesized $ZnAl_2O_4$ nanopowders.

Reaction temperature/Time (^{o}C/hour)	Specific surface area (m^2/g)	Average particle size (nm) from		
		XRD	BET	TEM
150/5 h	246	6.54	5.21	5.20
180/5 h	240	7.76	5.34	5.33
200/5 h	230	9.37	5.57	5.55
150/20 h	241	7.7	5.31	5.32
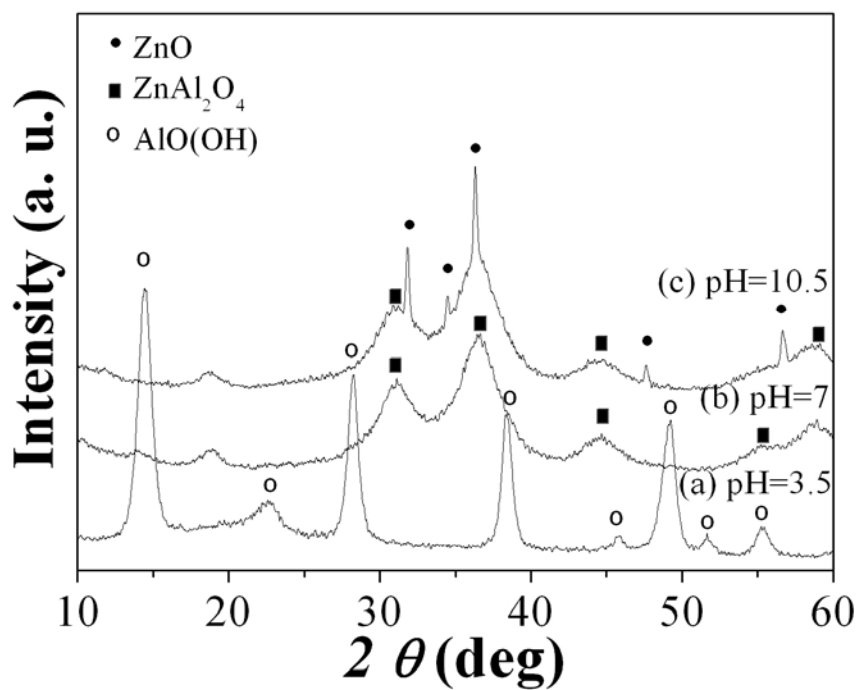
Fig. 6.1. XRD patterns of various phases by hydrothermally treating the precursors (aluminum chloride hexahydrate and zinc chloride) at 180 $^{\circ}$C for 5 h at different pH values.
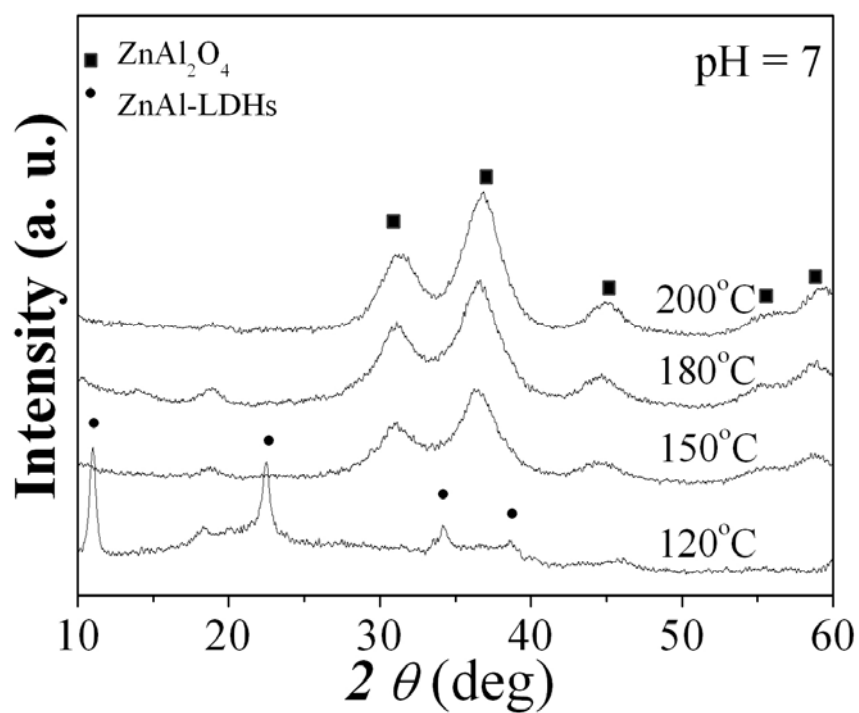
Fig. 6.2. XRD patterns of the solution with pH = 7 prepared by hydrothermal treatment at various temperatures for 5h.
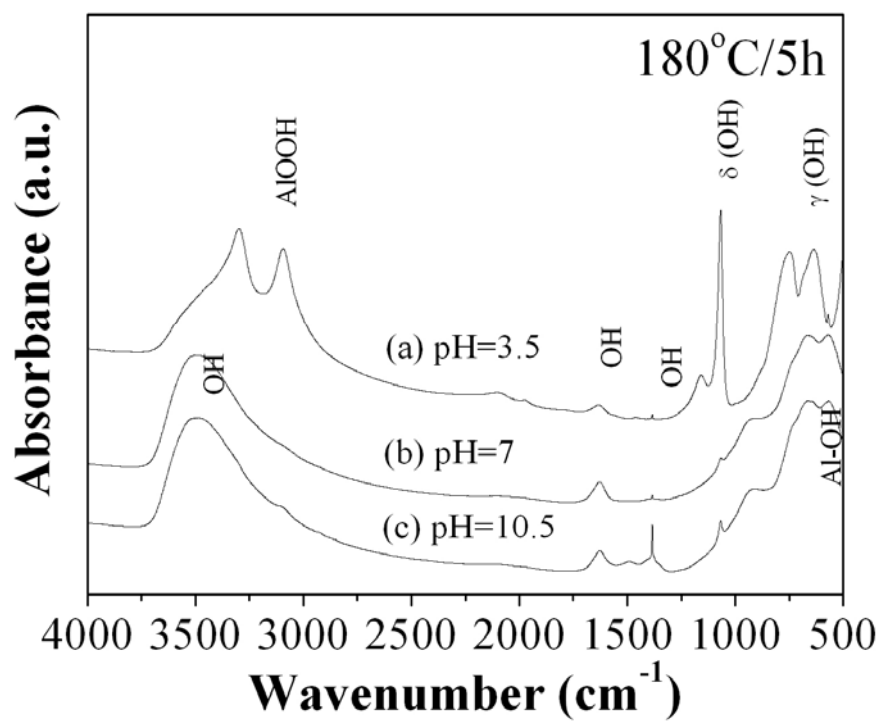
Fig. 6.3. FTIR spectra of various phases by hydrothermally treating the precursors at various pH values.
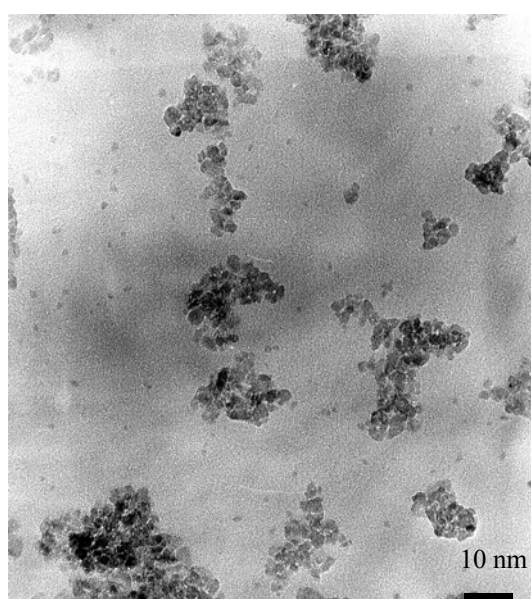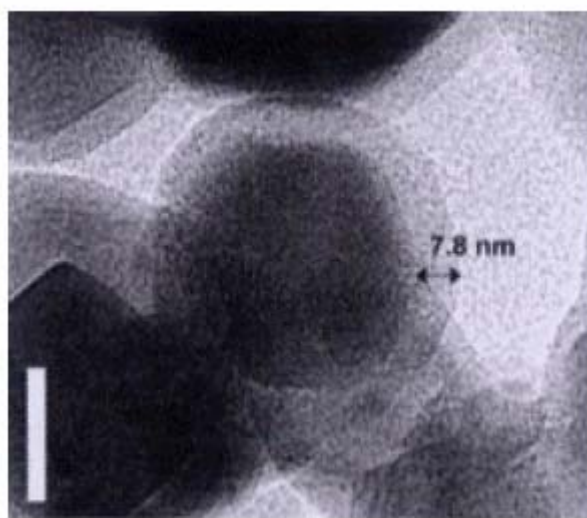
Fig. 6.4. TEM image of synthesized ZnAl$_2$O$_4$ nanoparticles.

Fig. 6.5. TEM image of Eu-coated $ZnAl_2O_4$ nanoparticles, mark = 20 nm.
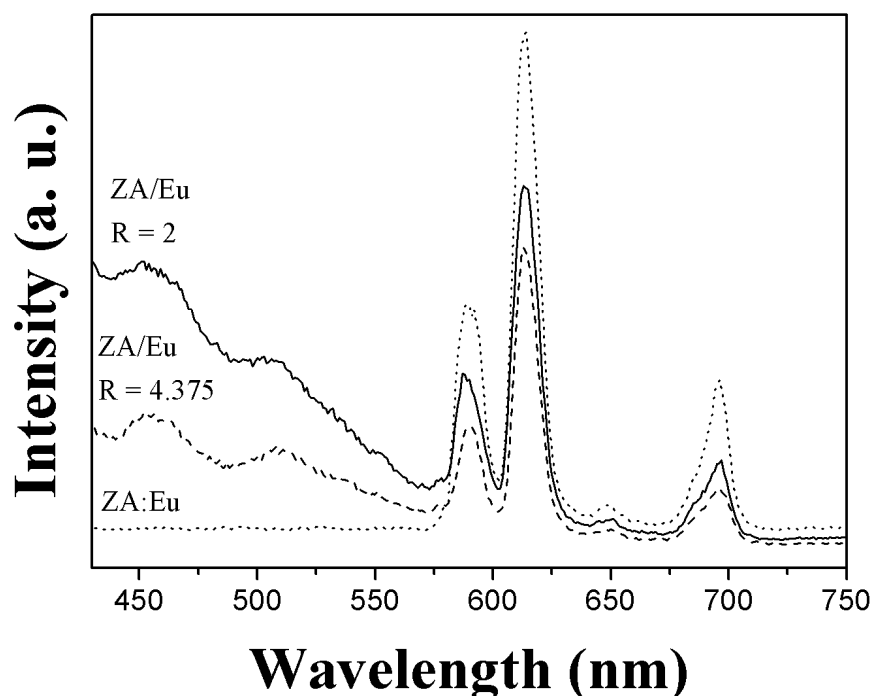
Fig. 6.6. PL spectra for ZnAl$_2$O$_4$/Eu core-shell particles excited by 390 nm.

Chapter 7

Physical characterization and tunable photoluminescence of Eu-doped strontium-substituted nano-halophosphate

7.1. Introduction

Calcium hydroxyapatite $(Ca_{10}(PO_4)_6(OH)_2$; HAP), a naturally-occurring biomaterial, has been a mineralized hard tissue found in bones and teeth of human and vertebrates, which attracted extensively studied for more than 30 years.[88] However, HAP has been employed as catalysts for the oxidation of lower alkanes, [89] and used for illuminating purpose which has long been known as halophosphate phosphor. 90, 91] Alkaline-earth haloposphates were efficient ultraviolet-stimulable luminescent materials. These materials have found wide applications as a blue component in three-band fluorescent lamps and field-emission displays as well as display devices.

Haloposphates luminophores, characterized by the general formula $Ca_5X(PO_4)_3A,B$, where X denotes F^-, Cl^-, Br^- or OH^- ions, and A and B represent activators and sensitizer, respectively. Recently this material was studied due to the developing of plasma display, in which the phosphor is demanded to be efficient and stable under the VUV excitation. In tradition, these halophosphates were prepared by

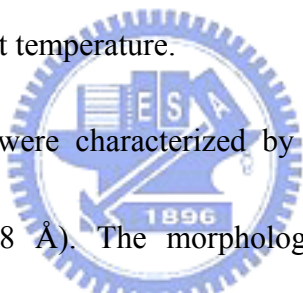a solid-state reaction method and the effect of the reaction conditions on the photostimulated luminescence of polycrystalline $Sr_9Ca(PO_4)_6Cl_2$:Eu was studied. [92] Furthermore, the formation of the apatites involves the formation of various intermediates and the preparation of luminescent-grade raw materials is critically dependent on various parameters such as pH values and precipitation temperature. [93]

Recently, some techniques have been reported for the preparation of europium-activated alkaline-earth-metal chlorophosphate luminophores through solution processing. However, the effect of the pH value in the precursor solution on the crystalline phase and luminescence characteristics of halophosphate phosphor nano-particles has not been systematically investigated, especially the role of annealing atmosphere in phosphor emission. Therefore, in this work, nanohalophosphate phosphor particles synthesized from different pH-value solutions will be studied by XRD and SEM at ambient temperature. For comparison, the influence of the pH value and annealing atmosphere on the crystalline phase, morphology and luminescence characteristics of halophosphate phosphor nano-particles will be dicussed.

7.2. Experimental procedure

In a typical experiment, regent-grade $Ca(NO_3)_2$, $SrCl_2$, urea, NH_4NO_3, and europium nitrate were dissolved in 100 ml of HCl solution at pH = 1–2 and then diammonium hydrogen phosphate (DAP) was added. The molar ratio of (Ca+Sr+Eu)/P is fixed at 1.67 and the pH value of the resulting sol solution was controlled by the addition of ammonia. Thereafter, the solid precipitate was filtered, washed with deionized water and then air-dried overnight at 60 ^{o}C. The resulting white polycrystalline powder is subjected to anneal at 850 ^{o}C in a reduced atmosphere and then fast cooled to ambient temperature.

The powdered samples were characterized by X-ray diffraction (XRD) with CuKα radiation (λ = 1.5418 Å). The morphology and microstructures of the nanoparticles were examined by scanning electron microscopy (SEM, JEOL-6500F). Luminescent properties are characterized by PL measurement under 254 nm excitation (FL F4500, Hitachi) at room temperature.

7.3. Results and discussion

7.3.1. Phase and microstructure development

Figs. 7.1 (a), (b), and (c) show the XRD of the halophosphate particles synthesized from the chemical solution with different pH values of 2, 8 and 10,

respectively. It can be observed that both $Ca_{8.3}Sr_{1.7}(PO_4)_6Cl_2$ and HAP phases appear

at the solution of pH = 2. According to the report of Yasukawa, [94] the Cl^- ions in

the starting solution have been considered to be barely incorporated into the HAP

particles because the Cl^- ions can be detected in the powders prepared from the

solution with the pH=1.6–2. Therefore, both $Ca_{8.3}Sr_{1.7}(PO_4)_6Cl_2$ and

$Ca_{8.3}Sr_{1.7}(PO_4)_6(OH)_2$ phases can be formed in the pH = 2 solution. At pH = 8, all the

peaks are characteristic of HAP phase. With increasing the pH value, at pH = 10, it is

difficult to form $Ca_{8.3}Sr_{1.7}(PO_4)_6Cl_2$ phase. Furthermore, the crystallization of the

HAP phase was enhanced and became stronger compared to that at pH = 8. Fig. 7.2

(a), (b), and (c) show the SEM microstructure of the halophosphate particles

synthesized from the chemical solutions with different pH values (pH = 2, 8, and 10)

at room temperature. At pH = 2, the rod particles were observed in Fig. 7.2 (a).

However, as the pH values of the chemical solution increased, the synthesized particle

sizes are small than 100 nm and the particle morphology becomes the plate as shown

in Fig. 7.2 (c). The plate-like crystals can be attributed to the formation of HAP

structure, as evidenced from XRD patterns, this indicating that the

nano-halophosphate particles can be synthesized via wet chemical process at room

temperature. From the TEM image (Fig. 7.3 (a)), the halophosphate particles

synthesized with pH = 2, we can find it covered the two kinds of the particle

morphology. This result is the same as the XRD patterns, as showed in Fig. 7.1. As the as-precipitated white powder was further annealed at 850 ^{o}C in a reduced atmosphere for 2 h, Fig. 7.4 shows the XRD diffraction patterns of the halophosphate powders synthesized at different pH solutions. As compared with Fig. 7.1, it was found that the crystallinity of both $Ca_{8.3}Sr_{1.7}(PO_4)_6Cl_2$ and HAP phases was apparently enhanced through thermal annealing but those phases do not change with annealing temperature (i.e., HAP does not transform into β-TCP). Furthermore, the crystallized phases remained unchanged even those powders were annealed at 850 ^{o}C in different atmospheres of N_2, H_2/N_2, and air for two hours. (not shown here) The above results indicate those nanohalophosphate powders were thermally stable.
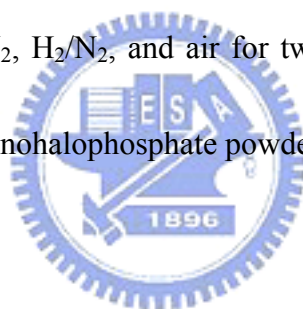
7.3.2. Eu effect

Luminescent properties are characterized by PL measurement under 254 nm excitation. The effect of the doped-Eu^{3+} content on the relative PL intensity at red emission (612 nm) and blue emission (450 nm) is shown in Fig. 7.5 for the halophosphate powders synthesized at pH=10 and then annealed at 850 ^{o}C for 2 h in H_2/N_2. It can be found that a maximum red emission (612 nm) PL intensity occurs at the sample with 7 mol% Eu added. Above that, the PL intensity was decreased because of concentration quenching effect. Furthermore, at such a high temperature

of 850 $^{\circ}$C, more Eu^{3+} ions were probably incorporated into the host lattice to substitute for Ca^{2+} ions in apatite where it is usually considered that rare-earth ions occupy mainly Ca (II) sites with Cs symmetry (6h site). [95] The substitution on Ca (II) sites needs a charge compensation mechanism which can be described as:

$$OH^- + Ca^{2+} \rightarrow Eu^{3+} + O^{2-} \tag{7.1}$$

According to charge neutrality, one can assume that the Eu^{3+} ions will remain in the neighborhood of the substituted oxygen ion. This indicates that the majority of Eu^{3+} ions occupy the sites in the neighborhood of OH$^-$ ions which are located in the channels. [96]
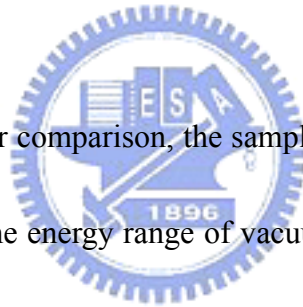
In order to make a further comparison, the samples were also measured by using the synchrotron radiation in the energy range of vacuum ultraviolet (VUV) range. As compared to that measured at 254 nm, similar trend was observed but it shows a stronger blue emission at 450 nm, corresponding to the radiative transition from the excited state of Eu^{2+}, 4f^{6}5d, to its ground state 4f^7. The luminescent properties of Eu^{2+} ions in various matrix compounds, and the reduction processes of Eu$^{3+} \rightarrow$ Eu^{2+} in phosphor preparations have been well known. [97] On the other hand, when the trivalent Eu^{3+} ions were doped into Ca$_{8.3}$Sr$_{1.7}$(PO$_4$)$_6$(OH)$_2$, they would replace the Ca^{2+} ions of Ca$_{8.3}$Sr$_{1.7}$(PO$_4$)$_6$(OH)$_2$. In order to keep the charge balance, two Eu^{3+} ions should be needed to substitute for three Ca^{2+} ions. Hence, one vacancy defect

represented as $V_{Ca}^{''}$ along with two negative charges and two positive defects of

$Eu_{Ca}^{.}$ would be created by each substitution of every two Eu^{3+} ions in the compound of

$Ca_{8.3}Sr_{1.7}(PO_4)_6(OH)_2$:Eu. The vacancy of $V_{Ca}^{''}$ then acted as a donor of electrons,

while the two $Eu_{Ca}^{.}$ defects became acceptors of the electrons. Consequently, the

electrons in the vacancy defects of $V_{Ca}^{''}$ would be transferred to $Eu_{Ca}^{.}$ sites and thus

Eu^{3+} could be possibly reduced to Eu^{2+}.

7.3.3. Photoluminescence characterization

Fig. 7.6 shows the room-temperature emission (excited at 254 nm) spectra of the

halophosphate powder synthesized at different pH solutions.   In Fig. 7.6 (a), it was

found that the all as-precipitated powders only showed one Eu^{3+} red emission

independent of the solution pH value. Among those samples, the pH = 8 powder

exhibits a maximum $^5D_0 \rightarrow ^7F_2$ (612 nm) red emission. This result may be attributed to

the fact that the Eu ions possibly easily tend to form $Eu(OH)^{2+}$ and $Eu(OH)^+_2$ [98] in

the solution with pH = 8 compared to that with pH = 2 and 10.

On the other hand, for the synthesized powders sintered at 850 ^{o}C in a reduction

atmosphere, it was found that the PL spectra of the nano-powders were strongly

influenced by the pH value in the chemical solution. As shown in Fig. 7.6 (b), not

only the peaks (450 nm) corresponding to Eu^{2+} emission but also the other two peaks

(590 and 612 nm) corresponding to Eu^{3+} emission were detected. It can be seen that the pH = 2 powder shows the strongest Eu^{2+} emission peak (450 nm) and Eu^{3+} emission peak (612 nm). This is probably related to the reduction of Eu^{3+} to Eu^{2+} and the crystalline effect of the $Ca_{8.3}Sr_{1.7}(PO_4)_6Cl_2$. This may indicate that part of the Eu^{3+} ions was more easily reduced to Eu^{2+} in $Ca_{8.3}Sr_{1.7}(PO_4)_6Cl_2$ matrix when the sample was subjected to thermal activation at 850 ^{o}C in this study. As one can see in Fig. 7.4, both $Ca_{8.3}Sr_{1.7}(PO_4)_6Cl_2$ and $Ca_{8.3}Sr_{1.7}(PO_4)_6(OH)_2$ phases can be formed in the pH = 2 solution, which makes contributions to strong blue and red emissions, respectively. On the other hand, for the samples prepared in the pH = 10 solution, although it is very difficult to form $Ca_{8.3}Sr_{1.7}(PO_4)_6Cl_2$. it was found that a weak blue–emission is still observed. This may reveal that the appearance of blue-emission in those samples prepared at pH = 8 and 10 is also related to the reduction of Eu^{3+} to Eu^{2+}.

Fig. 7.7 shows the PL spectra of the samples annealed at 850 ^{o}C in H_2/N_2 and air atmospheres for two hours as a function of solution pH value. As described above, for the samples synthesized from pH = 2 solution and annealed at H_2/N_2 reduction atmosphere, both stronger blue and red emissions were observed as shown in Fig. 7.7 (a).   However, as the samples prepared at pH = 2 was annealed in air, although both phases were detected, the blue emission becomes weak. Although the sample was sintered in air atmosphere, the reduction of $Eu^{3+} \rightarrow Eu^{2+}$ was also possible.   Similar

observation was also reported by Z. Pei [99] and J. Qiu [100] *et al*. that the reduction

of $Eu^{3+} \rightarrow Eu^{2+}$ also occurred in the Eu-doped matrixes annealed in air atmosphere.

On the other hand, as the samples were prepared in the pH = 10 solution, and

annealed in H_2/N_2 reduction atmosphere, a stronger blue emission was identified but

the observation is reversed for the sample annealed in air atmosphere shown in Fig.

7.7 (b). However, both emissions (blue and red) in Fig. 7.7 (b) show a weaker PL

intensity compared to that synthesized in the pH = 2 solution (Fig. 7.7 (a)). Above

results indicate that the atmosphere plays more important role in PL properties than

the crystalline phase formed in the sample. Therefore, all the results suggest that the

emission from one red to blue-red can be obtained by varying the pH value of the

precursor solution and controlling the annealing atmosphere. Furthermore, as

combining one green emission with the two strong emissions, a strong white emission

may be obtained from such a simple process, which will be further under

investigation.

.
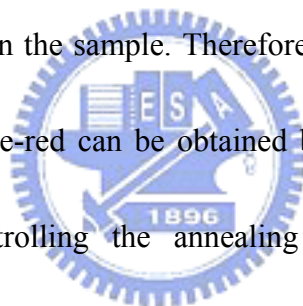
7.4. Conclusions

Nanocrystalline Eu-doped halo-phosphate particles with size smaller than 100

nm were obtained at room temperature. The crystalline phase was dependent on the

pH value in the solution. At pH=2, both $Ca_{8.3}Sr_{1.7}(PO_4)_6Cl_2$ and $Ca_{8.3}Sr_{1.7}(PO_4)_6(OH)_2$

phases were detected, but with an increase of pH value over 7, only one

$Ca_{8.3}Sr_{1.7}(PO_4)_6(OH)_2$ phase was identified. After prepared at pH = 2 and then

annealed at 850 ^oC in reduction atmosphere, the PL properties of the samples doped

with 7 mol% Eu exhibit strong blue and red emissions. In contrast, for the samples

prepared at pH = 10 and annealed in reduction atmosphere, the blue emission

becomes weaker. These results indicate that the relative peak intensity of red to blue

emissions can be tunable by controlling the solution pH value (crystalline phase) and

changing annealing atmosphere. In the future, it may provide an opportunity to

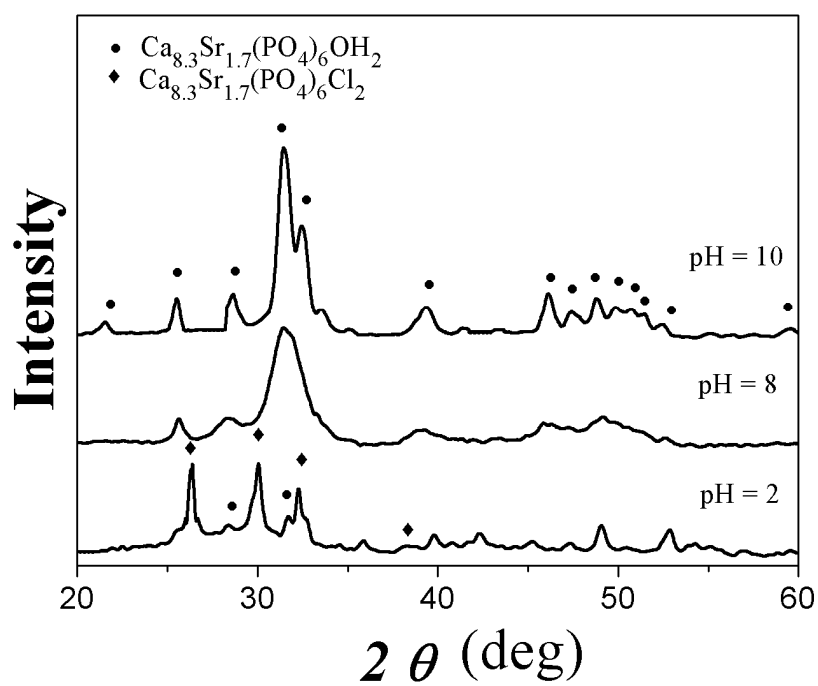develop white emission by co-doping another green emission element.

Fig. 7.1. XRD patterns of nano-halophosphate synthesized from the chemical solution

with different pH values as room temperature.

(a)

100 nm
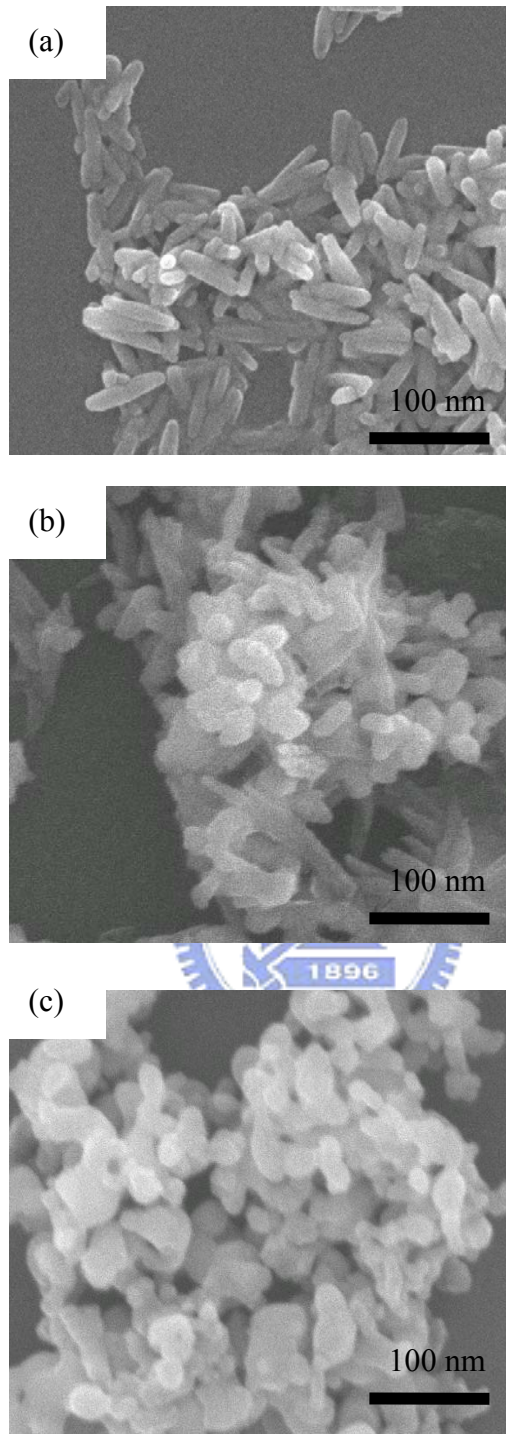
(b)

100 nm

(c)

100 nm

Fig. 7.2. SEM microstructure of the halophosphate particles synthesized from the chemical solution with different pH values (a) pH=2, (b) pH=8, and (c) pH=10
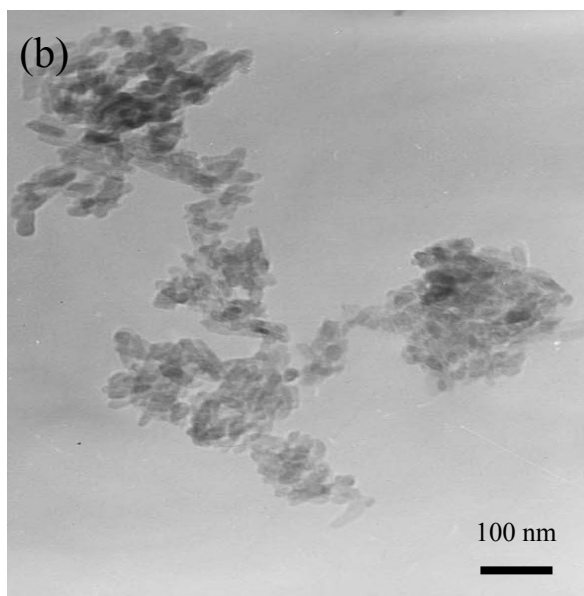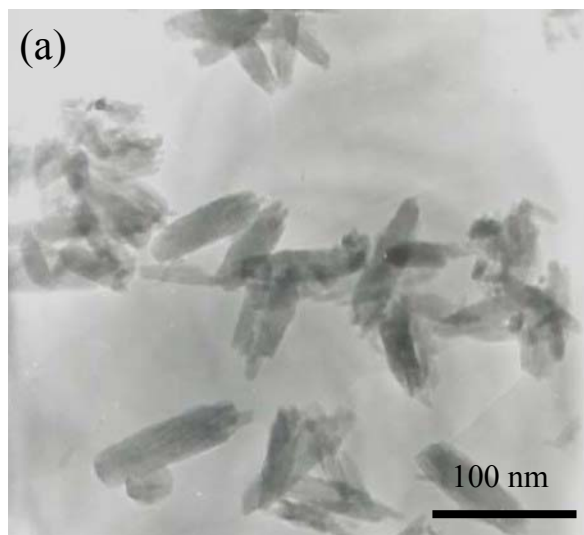
Fig. 7.3. TEM image of the halophosphate particles synthesized from the chemical solution with different pH values (a) pH = 2 and (b) pH = 10 at room temperature.
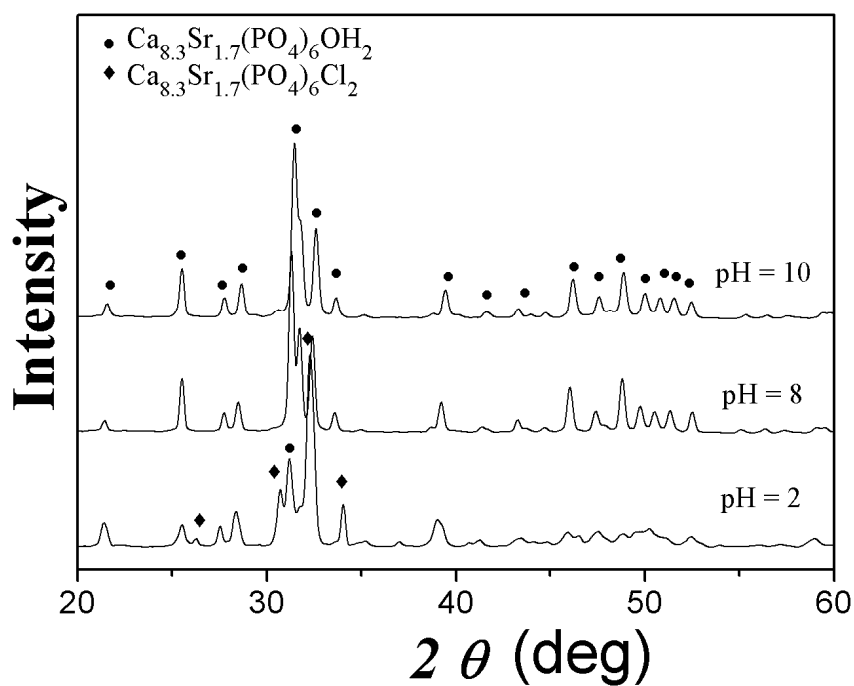
Fig. 7.4. XRD diffraction patterns of the halophosphate powders synthesized from the

chemical solution with different pH values and then annealed at 850 $^{\circ}$C for 2

h in H_2/N_2 atmosphere.
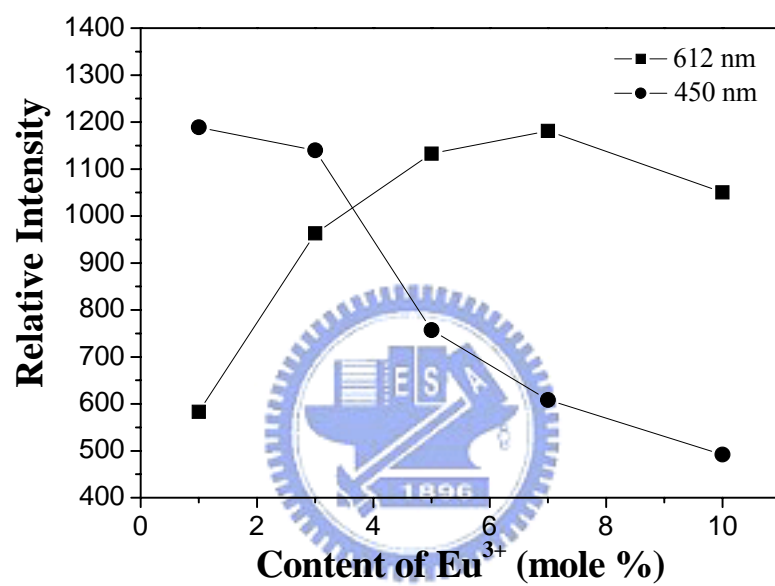
Fig. 7.5. Effect of the doped-Eu^{3+} content on the relative PL intensity of the halophosphate powders doped Eu.

Fig. 7.6. PL spectra of the (a) as-precipitated and (b) annealed halophosphate powders

at 850 ^{o}C in a reduced atmosphere for 2 h dependent on different pH solutions.

Fig. 7.7 PL spectra of the halophosphate powders prepared from the solution with different (a) pH=2 and (b) pH=10 values and then annealed at 850 $^{\circ}$C in air and H$_2$/N$_2$ atmospheres for 2 h.
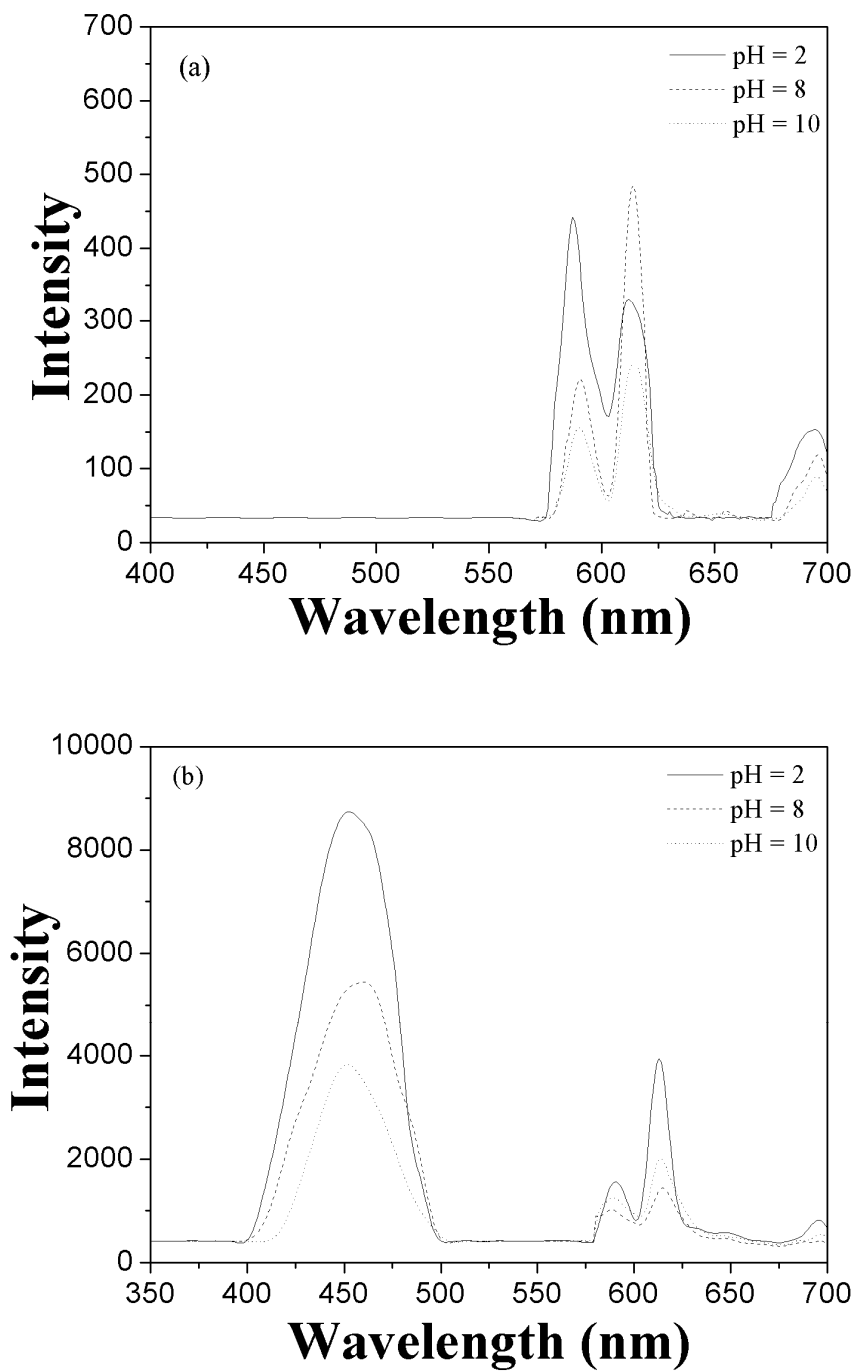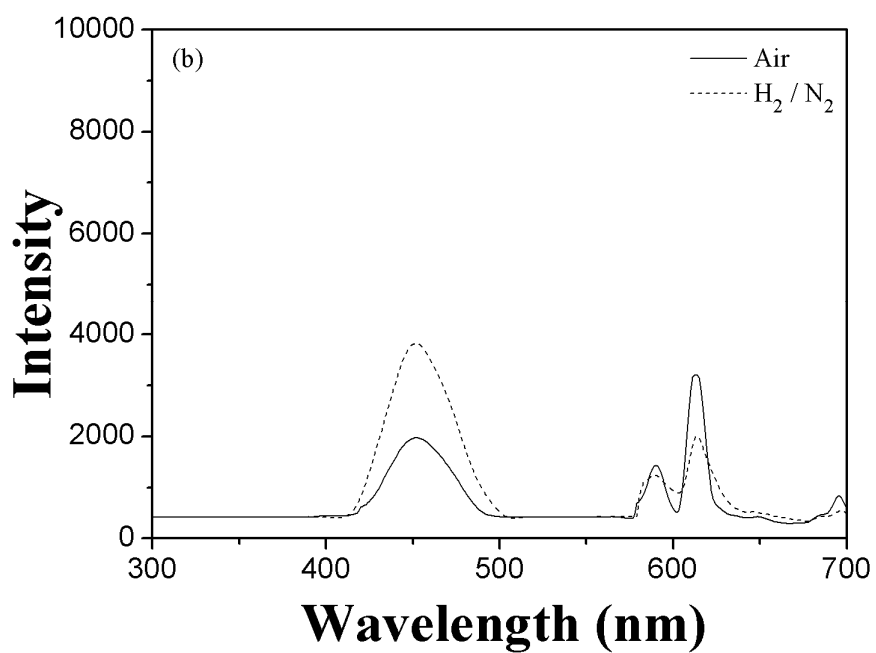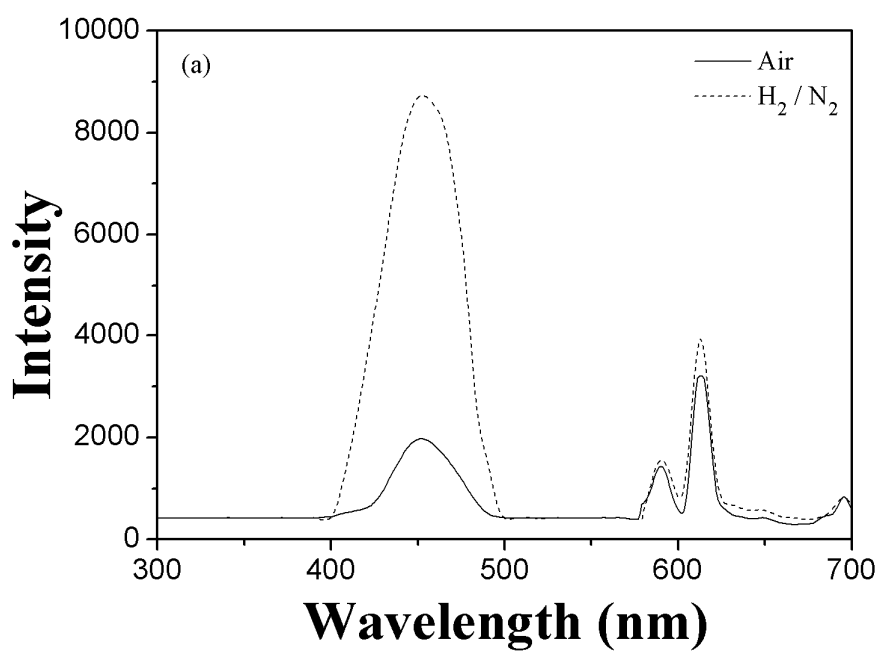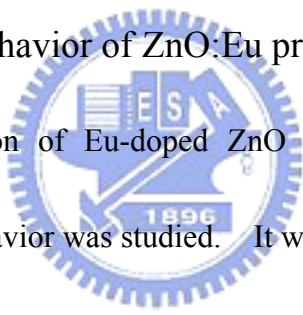
Chapter 8

Conclusions

8.1 Photoluminescence properties of ZnO film and nanorods under different atmosphere and annealing treatment

The ZnO films implanted with nitrogen ions from 5×10^{12} to 5×10^{15} cm^{-2} show high preferred-orientation (c-axis) films with strong NBE emission property. Furthermore, the annealing atmosphere plays an important role in crystalline and photoluminescence of nitrogen-implanted ZnO films. When annealed in nitrogen atmosphere, the peak intensity of near band-edge (NBE) emission remarkably decreases with the increase of concentration of implanted nitrogen. However, when the ZnO films were implanted with 5×10^{12} cm^{-2} and annealed in oxygen atmosphere, the optical properties are improved probably because the effective incorporation of O atom diminishes those donor levels (oxygen vacancies) and the crystalline is also improved due to implanted nitrogen. However, excess nitrogen would reduce the crystalline and promote the formation of the deep-level emission due to high amount of intrinsic and structure defects. This study reveals that it is possible to control the crystalline and the NBE emission of the ZnO films by using different annealing atmospheres and changing the nitrogen-implanted fluence.

High-density ZnO nanorods can be vertically grown on Si substrate from aqueous solution via a simple low-temperature process. After annealed in various atmospheres, the ZnO nanorods exhibit different PL spectra. A maximum UV emission was observed for the ZnO nanorods annealed in N_2 atmosphere which may be correlated with the decrease in defect density as evidenced in Raman and EPR. However, the EXAFS analysis demonstrates that the effect of annealing atmosphere on the deep-level defects of ZnO nanorods is confined in local surface area.

8.2 Photoluminescence behavior of ZnO:Eu prepared in different solvents

The phase transformation of Eu-doped ZnO powders prepared in different solvents on luminescence behavior was studied. It was found that the solvent plays a very important role in the ZnO-Eu_2O_3 system. When the powder was mixed in deionized water, it leads to the existence of Eu^{3+} ion in the ZnO matrix. The intrinsic red photoluminescence ($^5D_0 \rightarrow ^7F_2$) of Eu^{3+} is easily shielded by the ZnO intrinsic defect when the samples were excited with a short wavelength of 325 nm, because the energy level of $Eu^{\bullet}_{Zn}$ (0.19 eV) is closer to the conduction band than for $Zn^{\bullet\bullet}_i$ (0.22 eV). Therefore, no red emission can be detected. However, this work demonstrates that a sharp red emission can be promoted by treating the Eu-doped ZnO sample in acetone solvent.

8.3 Synthesis and optical characteristics of nanosize phosphors

Depending on pH values in the precursor solution, ZnAl layered double hydroxide (ZnAl-LDH), ZnO, boehmite or gibbsite could be formed. Nanocrystalline $ZnAl_2O_4$ with average particle size of ~5 nm are hydrothermal synthesized by controlling the precursor solution at pH = 7 at T > 120 ^oC for 5h through ZnAl layered double hydroxide (ZnAl-LDH). In addition, the $ZnAl_2O_4$/Eu core-shell structure can be developed by using the cationic surfactant CTAB. Both $^5D_0$ to $^7F_2$ sensitivity energy level and $^5D_2$ to $^7F_0$ depth energy level can be detected from the $ZnAl_2O_4$/Eu core-shell structure.

Nanocrystalline Eu-doped halo-phosphate particles with size smaller than 100 nm were obtained at room temperature. The crystalline phase was dependent on the pH value in the solution. At pH =2, both $Ca_{8.3}Sr_{1.7}(PO_4)_6Cl_2$ and $Ca_{8.3}Sr_{1.7}(PO_4)_6(OH)_2$ phases were detected, but with an increase of pH value over 7, only one $Ca_{8.3}Sr_{1.7}(PO_4)_6(OH)_2$ phase was identified. After prepared at pH = 2 and then annealed at 850 ^oC in reduction atmosphere, the PL properties of the samples doped with 7 mol% Eu exhibit strong blue and red emissions. In contrast, for the samples prepared at pH = 10 and annealed in reduction atmosphere, the blue emission becomes weaker. These results indicate that the relative peak intensity of red to blue emissions can be tunable by controlling the solution pH value (crystalline phase) and changing annealing atmosphere. In the future, it may provide an opportunity to develop white emission by co-doping another green emission element.

REFERENCES

[1] S. Shionoya and W. M. Yen, Phosphor Handbook, CRC Press, Boca Raton, FL (1999).

[2] E. N. Harvey, A History of Luminescence, American Philosophical Society, Philadelphia, PA (1957), p.18.

[3] H. J. Mullenmesister, Faszination Edelstein, Markt Schwaben (1990).

[4] L. H. Brixner, "New X-ray phosphors,"Mater. Chem. Phys. **16** (1987) 253.

[5] J. A. McDermott, Electrical Eng. **57** (1938) 286.

[6] R. N. Thayer and B. T. Barnes, J. Opt. Soc. Am. **29** (1939) 131.

[7] P. Maestro and D. Huguenin, "Industrial applications of rare earths: Which way for the end of the century,"J. Alloys Compd. **225** (1995) 520.

[8] G. Blasse and A. Bril, Philip Tech. Rundsch **10** (1970) 320.

[9] G. Blasse and B. C. Grabmaier, Luminescent materials, Springer, Berlin (1994).

[10] A. H. Kitai, Solid State Luminescence, London, (1993).

[11] M. Yoshimura, W. L. Suchanek and K. Byrappa, "Soft solution processing: a strategy for one-step processing of advanced inorganic materials," Mater. Res. Soc. Bull. **25** (2000) 17.

[12] T. P. Niesen and M. R. De Guire, "Review: deposition of ceramic thin films at low temperatures from aqueous solutions," J. Electroceram. **6** (2001) 169.

[13] T. Welton, "Room-temperature ionic liquids. Solvents for synthesis and catalysis," Chem. Rev. **99** (1999) 2071.

[14] A. V. Dijken, J. Makkinje and A. Meijerink, "The influence of particle size on the luminescence quantum efficiency of nanocrystalline ZnO particles," J. Lumin. **92** (2001) 323.

[15] M. H. Huang, S. Mao, H. Feick, H. Yan, Y. Wu, H. Kind, E. Weber, R. Russo and

P. Yang, "Room-temperature ultraviolet nanowire nanolasers," Science **292** (2001) 1897.

[16] H. M. Kim, T. W. Kang and K. S. Chang, "Nanoscale ultraviolet-light-emitting diodes using wide-bandgap gallium nitride nanorods," Adv. Mater. **15** (2003) 567.

[17] L. Vayssieres, "Growth of arrayed nanorods and nanowires of ZnO from aqueous solutions," Adv. Mater. **15** (2003) 464.

[18] J. H. Choy and E. S. Jang, "Soft solution route to directionally grown ZnO nanorod arrays on Si wafer; room-temperature ultraviolet laser," Adv. Mater. **15** (2003) 1911.

[19] T. Elnabarawy, A. Attia and M. Alaya, "Effect of thermal treatment on the structural, textural and catalytic properties of the $ZnO-Al_2O_3$ system," Mater. Lett. **24** (1995) 319.

[20] M. Valenzuela, P. Bosch and G. AguilarRios, "Comparison between sol-gel, coprecipitation and wet mixing synthesis of $ZnAl_2O_4$," J. Sol-gel Sci. Techn. **8** (1997) 107.

[21] A. Adak, A. Pathak and P. Pramanik, "Characterization of $ZnAl_2O_4$ nanocrystals prepared by the polyvinyl alcohol evaporation route," J. Mater. Sci. Lett. **17** (1998) 559.

[22] S. Mathur, M. Veith, M. Haas, A. Shen, "Single source sol-gel synthesis of nanocrystalline $ZnAl_2O_4$: structural and optical properties," J. Am. Ceram. Soc. **84** (2001) 1921.

[23] M. Zawadzki and J. Wrzyszcz, "Hydrothermal synthesis of nanoporous zinc aluminate with high surface area," Mater. Res. Bull. **35** (2000) 109.

[24] I. Pastoriza and L. M. Liz, "One-pot synthesis of $Ag@TiO_2$ core-shell nanoparticles and their layer-by-layer assembly," Langmuir **16** (2000) 2731.

[25] M. Kottaisamy, M. Mohan Rao and D. Jeyakumar, "Divalent europium-activated

alkaline-earth-metal chlorophosphate luminophores [$M_5(PO_4)_3Cl:Eu^{2+}$; M=Ca, Sr, Ba] by self-propagating high-temperature synthesis," J. Mater. Chem. **7** (1997) 345.

[26] D. Notzold and H. Wulff, "Structural and optical properties of the system $(Sr,Eu)_5(PO_4)_3(Cl,F)$." Phys. Stat. Sol. (b) 207 (1998) 271.

[27] R. Dafinova and A. Caralampydu, "Tin as reducing agent in Eu^{2+} doped alkali-earth fluorophosphates" J. Phys.: Condens. Matter 10 (1998) 6181.

[28] S. Sugiyama, M. Fujii, K. Fukuta and K. Seyama, "Preparation of alkaline earth phosphates with sol containing sodium alginate and sodium diphosphate." J. Colloid and Interface Science (2005) in print.

[29] A. I. Ekimov, A. L. Efros and A. A. Omushchenko, "Quantum size effect in semiconductor microcrystals," Solid State Commun. **56** (1985) 921.

[30] V. Rives and M. A. Ulibarri, "Layered double hydroxides (LDH) intercalated with metal coordination compounds and oxometalates," Coordination Chemistry Reviews **181** (1999) 61.

[31] K. H. Butler, Fluorescent Lamp Phosphors, University Press (1986).

[32] T. Welker, "Recent developments on phosphors for fluorescent lamps and cathode-ray tubes," J. Luminesc. **48&49** (1991) 49.

[33] J. B. Budin, J. C. Michael and F. Auzel, "Oscillator strengths and laser effect in $Na_2Nd_2Pb_6(PO_4)_6Cl_2$ (chloroapatite), a new high-Nd-concentration laser material," J. Appl. Phys. **50** (1979) 641.

[34] K. Kaniya, M. Tanakasi, T. Suzuki and T.Tanaka, "Effects of the addition of F^- ions on the properties of fibrous hydroxyapatite grown in the gel system,"Mater. Res. Bull. **25** (1990) 63.

[35] F. C. Pallila and B. E. O'Reilly, J Electrochem. Soc. **115** (1968) 1076.

[36] A. H. Hoekstra, W. L. Wanmaker and J. G. Verriet, J. Inorg. Nucl. Chem. (1970)

32.

[37] T. Soki, Y. Hatanaka and D. C. Look, "ZnO diode fabricated by excimer-laser doping," Appl. Phys. Lett. **76** (2000) 3257.

[38] K. Hummer, Phys. Status Solidi **56** (1973) 249.

[39] P. Zu, Z. K. Tang, G. K. L. Wong, M. Kawasaki, A. Ohtomo, H. Koinuma and Y. Segawa, "Ultraviolet spontaneous and stimulated emissions from ZnO microcrystallite thin films at room temperature," Solid State Commun. **103** (1997) 459.

[40] D. M. Bagnall, Y. F. Chen, Z. Zhu and T. Yao, "Optically pumped lasing of ZnO at room temperature," Appl. Phys. Lett. **70** (1997) 2230.

[41] T. Yamamoto and H. Yoshida, "Physics and control of valence states in ZnO by codoping method," Physica B **302&303** (2001) 155.

[42] K. Ogata, K. Sakurai, Sz. Fujita, Sg. Fujita and K. Matsushige, "Effects of thermal annealing of ZnO layers grown by MBE," J. Cryst. Growth **214&215** (2000) 312.

[43] K. Minegishi, Y. Koiwai, Y. Kikuchi, K. Yano, M. Kasuga and A. Shimizu, "Growth of p-type Zinc Oxide Films by Chemical Vapor Deposition," Jpn. J. Appl. Phys. **36** (1997) L1453.

[44] Y. R. Ryu, S. Zhu, D. C. Look, J. M. Wrobel, H. M. Jeong and H. W. White, "Synthesis of p-type ZnO films," J. Cryst. Growth **216** (2000) 330.

[45] C. H. Park, S. B. Zhang and S. H. Wei, "Origin of p-type doping difficulty in ZnO : the impurity perspective." Phys. Rev. B **66** (2002) 073202.

[46] M. Komatsu, N. Ohashi, I. Sakaguchi, S. Hishita and H. Haneda, "Ga, N solubility limit in co-implanted ZnO measured by secondary ion mass spectrometry," Appl. Surf. Sci. **189** (2002) 349.

[47] D. C. Park, I. Sakaguchi, N. Ohashi, S. Hishita and H. Haneda, "SIMS depth

profiling of N and In in a ZnO single crystal," Appl. Surf. Sci. **203&204** (2003) 359.

[48] A. N. Georgobiani, A. N. Gruzintsev, V. T. Volkov, M. O. Vorobiev, V. I. Demin and V. A. Dravin, Nuclear Instruments and Methods in Physics Research A514 (2003) 117.

[49] S. M. Myers, J. Vac. Sci. Technol. **15** (1978) 1650.

[50] C. C. Lin, C. S. Hsiao, S. Y. Chen and S. Y. Cheng, "Ultraviolet Emission in ZnO Films Controlled by Point Defects**,**" J. Electrochem. Soc. **151** (2004) G285.

[51] B. Lin, Z. Fu, Y. Jia and G. Liao, "Defect photoluminescence of undoping ZnO films and its dependence on annealing conditions." J. Electrochem. Soc. **148** (2001) G110.

[52] J. C. C. Fan and J. B. Goodenough, "X-ray photoemission spectroscopy studies of Sn-doped indium-oxide films**,**" J. Appl. Phys. **48** (1977) 3524.

[53] C. H. Liu, J. A. Zapien, Y. Yao, X. M. Meng, C. S. Lee, S. S. Fan, Y. Lifshitz, and S. T. Lee, "High-Density, Ordered Ultraviolet Light-Emitting ZnO Nanowire Arrays," Adv. Mater. **15** (2003) 838.

[54] S. Liu and J. J. Wu, Mater. Res. Soc. Symp. Proc. **703** (2002) 241.

[55] A. M. Morales and C. M. Liber, "A laser ablation method for the synthesis of crystalline semiconductor nanowires," Science **279** (1998) 208.

[56] T. J. Trentler, K. M. Hickman, S. C. Geol, A. M. Viano, P. C. Gibbons, and W. E. Buhro, "Solution-liquid-solid growth of crystalline III-V semiconductors: an analogy to vapor-liquid-solid growth," Science **270** (1999) 1791.

[57] H. Dai, E. W. Wong, Y. Z. Yu, S. S. Fan, and C. M. Liber, "Synthesis and characterization of carbide nanorods," Nature **375** (1999) 769.

[58] E. Leobandung, L. Guo, Y. Wang, and S. Y. Chou, "Observation of quantum effects and Coulomb blockade in silicon quantum-dot transistors at temperatures

over 100 K," Appl. Phys. Lett. **67** (1997) 938.

[59] S. C. Liou, C. S. Hsiao and S. Y. Chen, "Growth behavior and microstructure evolution of ZnO nanorods grown on Si in aqueous solution," J. Cryst. Growth **274** (2005) 438.

[60] G. J. Exarhos, A. Rose, and C. F. W. Jr, "Spectroscopic characterization of processing-induced property changes in doped ZnO films," Thin Solid Films **308&309** (1997) 56.

[61] M. Tzolov, N. Tzenov, D. Dimova-Malinovska and M. Kalitzova, "Vibrational properties and structure of undoped and Al-doped ZnO films deposited by RF magnetron sputtering," Thin Solid Films **379** (2002) 28.

[62] Y. G. Wang, S.P. Lau, X. H. Zhang and H. W. Lee, "Observations of nitrogen-related photoluminescence bands from nitrogen-doped ZnO films," J. Cryst. Growth,**252** (2005) 265.

[63] K. Vanheusden, W. L. Warren, C. H. Seager, D. R. Tallant, J. A. Voigt, and B. E. Gnade, "Mechanisms behind green photoluminescence in ZnO phosphor powders," J. Appl. Phys.**79** (1996) 7983.

[64] N. Y. Garces, N. C. Gilles, L. E. Halliburton, G. Cantwell, and D. C. Look, "Production of nitrogen acceptors in ZnO by thermal annealing," Appl. Phys. Lett. **80** (2002) 1334.

[65] P. H. Kasai, "Electron Spin Resonance Studies of Donors and Acceptors in ZnO," Phys. Rev. **130** (1963) 989.

[66] S. A. Studenikin, N. Geolego and M. Cocivera, "Fabrication of green and orange photoluminescent, undoped ZnO films using spray pyrolysis**,**" J. Appl. Phys. **84** (1998) 2287.

[67] K. L. Chopra, S. Major and D.K. Pandya, "Transparent conductors-a status review," Thin Solid Films **102** (1983) 1.

[68] N. J. Dayan, S. R. Sainkar, R. N. Karekar and R. C. Aiyer, "Formulation and characterization of ZnO:Sb thick-film gas sensors," Thin Solid Films **325** (1998) 254.

[69] P. Mitra, A. P. Chatterjee and H. S. Maiti, "Mechanical properties of flo-deflocculated and milled powders in the $Al_2O_3/ZrO_2(CeO_2)$ system,"J. Mater. Sci. **33** (1998) 441.

[70] Y. S. Park, C. W. Litton, T. C. Collins and D. C. Reynolds, "Exciton Spectrum of ZnO," Phys. Rev. **143** (1966) 512.

[71] B. J. Pierce and R. L. Hengehold, "Depth-resolved cathodoluminescence of ion-implanted layers in zinc oxide," J. Appl. Phys. **47** (1976) 644.

[72] J. A. Garcia, A. Remon and J. Piqueras, "Influence of Bi and Mn on the green luminescence of ZnO ceramics," J. Appl. Phys. **62** (1987) 3058.

[73] E. Tomzig and R. Helbig, "Band-edge emission in ZnO," J. Lumin. **14** (1976) 403.

[74] Y. Hayashi, H. Narahara, T. Uchida, T. Noguchi and S. Ibuki, " Photoluminescence of Eu-Doped ZnO Phosphors, " Jpn. J. Appl. Phys., **34** (1995) 1878.

[75] Y. K. Park, J. I. Han, M. G. Kwak, H. Yang and S. H. Ju, "Time-resolved spectroscopic study of energy transfer in $ZnO:EuCl_3$ phosphors," J. Lumin. **78** (1998) 87.

[76] P. K. Sharma, R. Nass and H. Schmidt," Effect of solvent, host precursor, dopant concentration and crystallite size on the fluorescence properties of Eu(III) doped yttria," Opt. Mater., **10** (1998) 161.

[77] W. Strek, P. Dreen, E. Lukowiak, J. Wrzyszcz, M. Zawadzki and P. Pershukevich, "Preparation and emission spectra of Eu(III) in nanostructured γ-alumina," Spectrochim. Acta. A **54** (1998) 2121.

[78] R. Roesky, J. Weiguny, H. Bestgen and U. Dingerdissen, "An improved synthesis method for indenes and styrenes by use of a ZnO/Al_2O_3 spinel catalyst," Appl. Catal. A : Gen. **176** (1999) 213.

[79] I. Futoshi, G. Naoyuki and M. Masashi, US Patent 5561089, (1996).

[80] T. Elnabarawy, A. Attia and M. Alaya, "Effect of thermal treatment on the structural, textural and catalytic properties of the $ZnO-Al_2O_3$ system," Mater. Lett. **24** (1995) 319.

[81] A. Adak, A. Pathak and P. Pramanik, "Characterization of $ZnAl_2O_4$ nanocrystals prepared by the polyvinyl alcohol evaporation route," J. Mater. Sci. Lett. **17** (1998) 559.

[82] M. Zawadzki and J. Wrzyszcz, "Hydrothermal synthesis of nanoporous zinc aluminate with high surface area," Mater. Res. Bull. **35** (2000) 109.

[83] I. Pastoriza and L. M. Liz, "One-Pot Synthesis of $Ag@TiO_2$ Core-Shell Nanoparticles and Their Layer-by-Layer Assembly," Langmuir **16** (2000) 2731.

[84] D. Panias, P. Asimidis and I. Paspaliaris, "Solubility of boehmite in concentrated sodium hydroxide solutions: model development and assessment," Hydrometallurgy, **59** (2001) 15.

[85] Y. Zhang and M and Muhammed, "Critical evaluation of thermodynamics of complex formation of metal ions in aqueous solutions: VI. Hydrolysis and hydroxo-complexes of Zn^{2+} at 298.15 K," Hydrometallurgy, **60** (2001) 215.

[86] Z. Chen, E. Shi and W. Li, "Particle size comparison of hydrothermally synthesized cobalt and zinc aluminate spinels, " J. Am. Ceram. Soc. **85** (2002) 2949.

[87] A. Smith, "Pyrosol deposition of ZnO and SnO_2 based thin films: the interplay between solution chemistry, growth rate and film morphology," Thin Solid Films **376** (2000) 47.

[88] M. I. Kay, R. A. Youmg and A. S. Posner, "," Nature **204** (1964) 1050.

[89] S. Sugiyama, H. Matsumoto, H. Hayashi and J. B. Moffat, "Decomposition of tetrachloromethane on calcium hydroxyapatite under methane oxidation conditions," Appl. Catal. B **20** (1999) 57.

[90] Mitsubishi Corporation, Japanese patent JP 82137382, August(1982).

[91] Toshiba Corporation, Japanese patent JP 6001747, January (1985).

[92] R. Dafinova and V, Pelova, "Cerium, terbium as sensitizers of calcium fluorochlorophosphate," J. Mater. Sci. Lett. **14** (1995) 1414.

[93] M. Kottaisamy, M. Mohan Rao and D. Jeyakumar, "Divalent europium-activated alkaline-earth-metal chlorophosphate luminophores [$M_5(PO_4)_3Cl:Eu^{2+}$; M=Ca, Sr, Ba] by self-propagating high-temperature synthesis," J. Mater. Chem. **7** (1997) 345.

[94] A. Yasukawa, T. Matsuura and M. Nakajima, "Preparation of nonstoichiometric calcium hydroxyapatite using formamide," Mater. Res. Bull. **34** (1999) 589.

[95] R. Ternane, G. Panczer, M. Th. Cohen-Adad and C. Goutaudier, "Relationships between structural and luminescence properties in Eu^{3+}-doped new calcium borohydroxyapatite," Opt. Mater. **16** (2001) 291.

[96] R. Ternane, M. Trabelsi and N. Kbir, "Luminescent properties of Eu^{3+} in calcium hydroxyapatite," J. Lumin **81** (1999) 165.

[97] G. Blasse and A. Bril, Philips Res. Rep. **23** (1968) 201.

[98] W. Xiangke, "Sorption and desorption of Eu and Yb on alumina: mechanisms and effect of fulvic acid," Appl. Radia and Isotop **52** (2000) 165.

[99] M. Peng, Z. Pei, G. Hong and Q. Su, "Study on the reduction of $Eu^{3+} \rightarrow Eu^{2+}$ in $Sr_4Al_{14}O_{25}$: Eu prepared in air atmosphere," Chemical Physics Letters **371** (2003) 1.

[100] M. Peng, J. Qiu, l. Yang and C. Zhao, "Observation of $Eu^{3+} \rightarrow Eu^{2+}$ in barium hexa-aluminates with β′ or β-alumina structures prepared in air," Optical Materials **27** (2004) 591.

PUBLICATIONS

Journal papers

1. <u>Chih-Cheng Yang</u>, San-Yuan Chen and Syh-Yuh Cheng, "Synthesis and physical characteristics of ZnAl2O4 nanocrystalline and ZnAl2O4/Eu core-shell structure via hydrothermal route" Powder Technology, **148** (2004) 3.

2. <u>Chih-Cheng Yang</u>, Syh-Yuh Cheng, Hsin-Yi Lee and San-Yuan Chen, "Effects of phase transformation on photoluminescence behavior of ZnO:Eu prepared in different solvents" Ceramics International, (2005). (in print)

3. <u>Chih-Cheng Yang</u>, Chin-Ching Lin, Cheng-Hsiung Peng and San-Yuan Chen, " Effect of annealing atmosphere on physical characteristics and photoluminescence properties of nitrogen-implanted ZnO thin films" Journal of Crystal Growth, July (2005). (in print)

4. <u>Chih-Cheng Yang</u>, San-Yuan Chen and Hsin-Yi Lee, "Physical characterization of ZnO nanorods grown on Si from aqueous solution and annealed at various atmospheres" Journal of Vacuum Science and Technology B, September (2005). (was accepted)